Coherent Coupling in Light-Matter Systems

Christopher. R. Gubbin

Department of Physics

Imperial College

This dissertation is submitted for the degree of

Doctor of Philosophy

September 2016

Declaration

I hereby declare that this thesis entitled "Coherent coupling in light-matter systems" and the work presented in it are my own. I confirm that:

- This work was done wholly or mainly while in candidature for a research degree at this University.
- Where any part of this thesis has previously been submitted for a degree or any other qualification at this University or any other institution this has been clearly stated.
- Where I have consulted the published work of others, this is always clearly stated.
- Where I have quoted from the work of others, the source is always given. With the exception of such quotations this thesis is entirely my own work.
- I have acknowledged all main sources of help.
- Where the thesis is based on work done by myself jointly with others, I have made clear exactly what was done by others and what I have contributed myself.

The copyright of this thesis rests with the author and is made available under a Creative Commons Attribution Non-Commercial No Derivatives licence. Researchers are free to copy, distribute or transmit the thesis on the condition that they attribute it, that they do not use it for commercial purposes and that they do not alter, transform or build upon it. For any reuse or redistribution, researchers must make clear to others the licence terms of this work

Christopher. R. Gubbin
September 2016

Acknowledgements

I owe Professors Stefan Maier and Simone De Liberato a great debt of gratitude for their patience, support and trust in enacting this work. Without this none of the work herein would have been possible. I would also like to thank Professor Stéphane Kena-Cohen for his advice and guidance provided to me as a novice in the world of research. In addition I would like to thank Professor Alberto Politi and Francesco Martini at the University of Southampton who fabricated the samples utilised in Chapter 3.
I would also like to thank my friends and colleagues at Imperial College, especially Edmund Lovell, Oliver Baumfeld and Jack Carter-Gartside who provided a wonderful office environment and made my PhD so memorable.
Finally I would like to thank my family and partner for their love, support and tolerance during the course of this research degree.

Abstract

The strength of interaction between light and matter states is characterised by the Rabi frequency Ω which describes the rate at which they exchange energy. When Ω exceeds the system linewidth then the system is correctly described by dressed eigenstates of the coupled light-matter system. This is the strong coupling regime. Strong coupling has been demonstrated at the surface of polar dielectrics between phonon oscillations of the ionic species and light resulting in evanescent field confinement in modes termed surface phonon polaritons (SPhPs). Recent fabrication advances allow for creation of user defined SPhP resonators that support sub-diffraction SPhPs confined in three dimensions. We present a numerical study of these localised SPhP resonances in subwavelength cylindrical SiC resonators finding modes with long lifetimes and strong electric field enhancements. Additionally we investigate numerically and experimentally interactions between the localised SPhPs and the delocalised SPhP of a planar SiC interface demonstrating that this can also be coherent.

Strong light-matter coupling is also possible when a material with an resonant electronic transition such as an organic semiconductor is sandwiched in a planar optical microcavity. By employing a molecule with a broad electronic transition it is possible to reach the ultrastrong coupling (USC) regime where the coupling frequency becomes an appreciable fraction of the bare frequency and new physics is predicted. We investigate experimentally the electroluminescence properties of an optical microcavity in this regime utilising for the active layer the oligomer TDAF. We demonstrate light-matter couplings exceeding 20% of the bare resonant frequencies. Our bias resolved measurements allow for conclusions about the process of polariton formation under electrical pumping to be drawn.

Finally we present a method to describe the coupled eigenstates in arbitrary, inhomogeneous dielectric environments. By following Hopfield procedure we show that it is possible to diagonalise and correctly quantise the modes of the system. We also show how this model can be extended to include losses and illustrate an application to the specific case of the SPhP at a planar interface.

Table of contents

List of figures **xi**

List of Abbreviations **xiii**

1 Introduction **1**

2 Beating the Diffraction Limit **5**
2.1 Background 5
2.1.1 Dielectric Confinement of Light 5
2.1.2 Plasmonics 8
2.2 Surface Phonon Polaritons 10
2.2.1 A Thorough Review of Surface Phonon Polaritonics 17
2.2.2 Propagative Phonon Polaritons 21

3 Surface Phonon Polariton Resonators **23**
3.1 Finite Element Simulations of Silicon Carbide Pillars 24
3.1.1 Modelling Strategy 24
3.1.2 Pole Finding Procedure 28
3.1.3 Modes of Isolated Cylindrical Resonators 30
3.1.4 Resonator Arrays 37
3.1.5 Coherent Coupling Between Propagative and Localised Phonon Polaritons 39
3.2 Measurements of the Coherent Coupling 46
3.3 Conclusions 52

4 Electrical Pumping of Microcavity Polaritons **57**
4.1 Microcavity Polaritons 57
4.2 Ultrastrong Coupling 60
4.3 Excitation and Relaxation of Microcavity Polaritons 61

4.4 Polariton Electroluminescence from an Ultrastrongly Coupled Organic Light-Emitting Diode 62
4.5 Conclusions 67

5 Free Space Hopfield Diagonalisation of Inhomogeneous Light Matter Systems 71
5.1 Quantisation in the Absence of Dispersion 72
5.2 Field Quantisation in Dispersive, Non-Dissipative Media 73
5.3 Application: Phonon Polariton at a Planar Interface 81
5.4 Field Quantisation in Dispersive, Dissipative Media 91
5.5 Conclusions 96

Bibliography 99

List of figures

2.1 Sketch of evanescent fields at a planar interface 7
2.2 Metallic dielectric function and dispersion relation for surface mode on a metallic halfspace. 9
2.3 Ionic crystal dielectric function and dispersion relation for surface mode on a polar dielectric halfspace. 11
2.4 Phonon dispersion for a one-dimensional diatomic chain 13
2.5 Comparison of phonon dispersions in Si and 3C-SiC 16
2.6 A comparison of quality factors for a range of materials evaluated at the Fröhlich frequency 18

3.1 Comparison of numerical and analytical Purcell enhancements for a dipole placed on-axis above a cylindrical resonator 30
3.2 Numerical real resonant frequencies, quality factors, Purcell factors and mode volumes for the fundamental longitudinal mode 31
3.3 Numerical real resonant frequencies, quality factors, Purcell factors and mode volumes for the fundamental transverse mode 33
3.4 Effect of the substrate for an isolated resonator 36
3.5 Illustration of the dispersive nature of the longitudinal mode 37
3.6 Study of the effect of the substrate on the inter-resonator coupling . . . 38
3.7 Study of the band folding of the SPhP dispersion 40
3.8 Real frequency results for square arrays of SiC pillars on a planar SiC substrate 42
3.9 Hopfield coefficients for the coupled modes of square arrays of SiC pillars on a planar SiC substrate 44
3.10 Linewidths for the coupled modes of square arrays of SiC pillars on a planar SiC substrate 45
3.11 Image of the fabricated array 47
3.12 Illustration of the optical measurement 48

3.13 Experimentally recorded reflectance map 49
3.14 Hopfield model fit to experimental data 51
3.15 Experimental linewidth of the coupled modes 53

4.1 Illustration of strong coupling in a planar optical microcavity 59
4.2 Physical and electronic structure of the microcavity light emitting diode 63
4.3 Contour plots of the angle resolved electroluminescence from the LED . 65
4.4 Bias resolved power emission from the microcavity OLED 67
4.5 Illustration of the formation of coherent polaritonic states by electrical pumping 68
4.6 The external quantum efficiency of the microcavity LED under electrical pumping 69

5.1 Illustration of the modes of a planar halfspace supporting a surface mode 83

List of Abbreviations

CQED Cavity quantum electrodynamics

DBR Distributed Bragg reflector

EL Electroluminescence

EQE External quantum efficiency

FEM Finite element method

FTIR Fourier transform infrared

HOMO Highest occupied molecular orbital

IR Infrared

ISB Intersubband

LO Longitudinal optical

LSPhR Localised surface phonon resonance

LUMO Lowest unoccupied molecular orbital

MIM Metal insulator metal

mIR Mid infrared

OLED Organic light emitting diode

PL Photoluminescence

PML Perfectly matched layer

List of Abbreviations

PZW Power Zienau Wooley

QNM Quasi-normal modes

RWA Rotating wave approximation

s-SNOM Scattering scanning near-field optical microscope

SPhP Surface phonon polariton

SPP Surface plasmon polariton

TM Transverse magnetic

TO Transverse optical

USC Ultrastrong Coupling

UV Ultraviolet

Chapter 1

Introduction

How much can we confine the energy stored in an electromagnetic field? One way to analyse this is by the consideration of the Fourier transform of an arbitrary function $\mathcal{F}$ defined in three dimensions as

$$\mathcal{F}(\mathbf{k}) = \frac{1}{2\pi} \int \mathcal{F}(\mathbf{r})\, e^{i\mathbf{k}\cdot\mathbf{r}} \mathrm{d}\mathbf{r}, \tag{1.1}$$

where $\mathbf{r}$ describes the spatial coordinates and $\mathbf{k}$ is a vector of spatial frequencies. The inverse transform is given by

$$\mathcal{F}(\mathbf{r}) = \frac{1}{2\pi} \int \mathcal{F}(\mathbf{k})\, e^{-i\mathbf{k}\cdot\mathbf{r}} \mathrm{d}\mathbf{k}, \tag{1.2}$$

which implies that a function of arbitrary variation in spatial coordinates $\mathbf{r}$ may be constructed by selection of appropriate generating spatial frequencies $\mathbf{k}$. This is strictly true if we are able to use all spatial frequencies in the transform Eq. 1.2. In an electromagnetic system however the contributing spatial frequencies at a given frequency ω must satisfy the Helmholtz equation which gives

$$\mathbf{k}\cdot\mathbf{k} = \frac{\epsilon\omega^2}{\mathrm{c}^2}, \tag{1.3}$$

where c is the speed of light in a vacuum and ϵ is the dielectric constant of the medium. This imposes the inequality

$$\sqrt{\mathbf{k}\cdot\mathbf{k}} \leq \frac{\sqrt{\epsilon}\omega}{c} = \sqrt{\epsilon}\sqrt{\mathbf{k}_0\cdot\mathbf{k}_0} \tag{1.4}$$

where $\mathbf{k}_0$ is the free space wavevector on the spatial frequencies that provide an upper limit to the inverse Fourier transform Eq. 1.2. Rather than being over all spatial

frequencies the integral therefore taken over a sphere centred on the origin delimited by inequality Eq. 1.4. The result is the well known diffraction limit of optical systems, most famously described by Abbe as a limit to the resolution of two closely spaced point sources in an imaging system [1].

The diffraction limit is not a fundamental restriction on our ability to confine energy. To achieve stronger confinement we just increase the range of spatial frequencies contained in the inequality Eq. 1.4. This can either be achieved by increasing the dielectric constant of the confining material ϵ or by coupling photons to charge oscillations at material interfaces creating evanescent waves with complex wavevector whose imaginary components reduce the value of $\mathbf{k}\cdot\mathbf{k}$. Two systems in which the latter is possible are conductors such as metals or doped semiconductors, where the coupled oscillations are termed surface plasmons polaritons and polar dielectrics, where they are termed surface phonon polaritons. These systems are discussed in Chapter 2. They provide a method of miniaturising optical interconnects and devices below the diffraction limit toward the dimensions of competing electronic devices. In addition, strong localisation of light allows for a large increase of the local energy density presenting the possibility of improved sensing or non-linear photonic interactions.

By coupling to material systems in this way we are tailoring the local photonic environment and can thereby engineer the spontaneous emission rate of emitters by a reordering of the local photonic density of states. When the light-matter coupling rate, which is characterised by the vacuum Rabi frequency Ω is less than the linewidths of the light and matter modes this reshuffling results in an enhancement of spontaneous emission and the coupling manifests as an enhanced transition between decoupled light and matter states. When the Rabi frequency exceeds the linewidths of the constituent modes this is no longer true as energy is coherently exchanged between the light and matter a number of times before escaping. This is the strong or coherent coupling regime. In this regime the system is described by dressed eigenstates that are a mixture of light and matter modes. The works presented in this thesis will explore systems that operate in this regime of coherent coupling.

Coherent light-matter coupling is possible at the surface of polar dielectric materials. In these systems the coupling is between photons and coherent oscillations of the ionic species on the surface as optical phonons. This has recently been investigated in the specific case of cylindrical silicon carbide resonators on a planar silicon carbide substrate [2, 3]. Modes are supported in the SiC Reststrahlen band between $10-12.5\mu$m in the mid-infrared (mIR) spectral region with narrow linewidths and long lifetimes with applications for sub-diffraction, super-resolution imaging or enhanced molecular sensing

through surface enhanced infrared absorption. In Chapter 3 a thorough numerical study of the morphological dependance of the modes of this system is presented and figures of merit regarding field confinement are evaluated to allow for comparison with plasmonic analogues. In addition, we present both experimental and numerical results demonstrating the coherent coupling between localised SPhP (lSPhR) modes supported in the cylindrical resonators and delocalised SPhP modes supported at the SiC interface an understanding of which is vital for predictive spectral tuning of resonator modes.
Coherent coupling is also possible in planar optical microcavites containing a resonant material where polaritons result from coherent coupling between the bare modes of the optical microcavity and the (typically) electronic resonance of the interstitial material [4]. The coupled states of these systems have been shown to exhibit Bose-Einstein condensation [5] resulting in observations of exotic physics such as polariton superfluidity [6] under optical pumping. In Chapter 4 we present an experimental study of the electroluminescence from a planar optical microcavity in the regime where the coupling rate becomes an appreciable fraction of the bare frequencies termed the ultrastrong coupling (USC) regime. Our results allow for conclusions to be drawn about the mechanism of polariton formation under electrical pumping and it's efficiency.
Finally we present a general theoretical scheme for calculating and quantising the modes of arbitrary inhomogeneous dielectric environments by a real space Hopfield diagonalisation procedure. This work is presented in Chapter 5 and presents a foundation for development of a quantum theory of non-linear interactions.

Chapter 2

Beating the Diffraction Limit

2.1 Background

2.1.1 Dielectric Confinement of Light

Confinement of light is generally achieved by applying boundary conditions to the electric field in the form of an optical resonator. The simplest way to construct fields with higher spatial resolution is by utilising dielectric cavities, this increases the upper bound on the spatial frequencies contributing to the field by Eq. 1.4. An easily understood example is described by Mie theory, a fully analytical solution for the scattering of light by spherical particles. It is found that spheres exhibit resonances dependant upon relative dielectric function and radius expandable in a series of electric and magnetic multipoles [7]. These modes are leaky but may still reach extremely high quality factors, the largest observed is 10^{10} in Si spheres of radius $\approx 1000\lambda$ [8]. They also exhibit remarkably high scattering efficiencies, with effective cross sections far exceeding the sphere geometrical cross section. Initially the results were used to predict far field behaviours of spherical particles, however more recently the near field has become experimentally accessible and there has been a resurgence in interest. The near field of a dielectric Mie scatterer can be intense as follows from the ability of the particles to draw in radiation far exceeding their geometric cross section. This is well illustrated in [9], here dielectric spheres are dispersed on a substrate and illuminated, the enhanced near field causes melting of the substrate directly below the spheres. This local field enhancement has been applied to Raman spectroscopy [10]. By using a optically trapped dielectric microsphere spatial resolution was improved by an order of magnitude due to concentration of light in the nearfield . Antennas composed of Si spheres have been predicted to enhancement the decay rate of localised dipoles by

an order of magnitude [11]. Albella *et al.* [12] showed that Si sphere dimers support local field enhancements of around an order of magnitude in gap modes. While such field enhancements are useful the modes are diffraction limited remain limited by the materials available. The majority of the results discussed above utilise silicon as a result of its low optical loss and high refractive index, reaching n≈3.45 at telecommunication wavelengths, this is close to the achievable limit.

An alternative approach can be found by analysis of Eq. 1.4. If one or more of the vector components of $\mathbf{k}$ were imaginary then it would allow for a greater bandwidth in the real components. The conditions under which imaginary spatial frequencies are supported can be ascertained by consideration of the planar interface between two dielectrics illustrated in Fig. 2.1 characterised by the dielectric functions $\epsilon_1(\omega)$ for $z>0$ and $\epsilon_2(\omega)$ for $z<0$. If we postulate an evanescent, transverse magnetic (TM) polarised solution to the Maxwell equations as

$$\mathrm{H}_{\parallel}^{1}=\mathrm{H}_0 e^{i\left(\mathrm{k}_{\parallel}\mathrm{r}_{\parallel}-\omega\mathrm{t}\right)-\mathrm{k}_{\mathrm{z},1}|\mathrm{z}|}\hat{\mathbf{e}}_{\perp}, \tag{2.1}$$

$$\mathrm{H}_{\parallel}^{2}=\mathrm{H}_0 e^{i\left(\mathrm{k}_{\parallel}\mathrm{r}_{\parallel}-\omega\mathrm{t}\right)-\mathrm{k}_{\mathrm{z},2}|\mathrm{z}|}\hat{\mathbf{e}}_{\perp}, \tag{2.2}$$

fulfilling continuity of the magnetic field $\mathbf{H}$ tangential to the interface. Here $\mathrm{H}_{\parallel}^{1}, \mathrm{H}_{\parallel}^{2}$ refer to the tangential magnetic field in mediums 1 and 2 respectively, $\mathrm{k}_{\parallel}$ is the in-plane wavevector and $\mathrm{k}_{\mathrm{z},1}, \mathrm{k}_{\mathrm{z},2}$ are the out-of-plane wavevector in mediums 1 and 2, respectively. Now utilising the Maxwell curl equation we see that the in-plane electric field is given by

$$\mathrm{E}_{\parallel}^{1}=\frac{-\mathrm{k}_{\mathrm{z},1}\mathrm{c}}{\omega\epsilon_1}\mathrm{H}_0 e^{i\left(\mathrm{k}_{\parallel}\mathrm{r}_{\parallel}-\omega\mathrm{t}\right)-\mathrm{k}_{\mathrm{z},1}|\mathrm{z}|}\hat{\mathbf{e}}_{\parallel}, \tag{2.3}$$

$$\mathrm{E}_{\parallel}^{2}=\frac{\mathrm{k}_{\mathrm{z},2}\mathrm{c}}{\omega\epsilon_2}\mathrm{H}_0 e^{i\left(\mathrm{k}_{\parallel}\mathrm{r}_{\parallel}-\omega\mathrm{t}\right)-\mathrm{k}_{\mathrm{z},2}|\mathrm{z}|}\hat{\mathbf{e}}_{\parallel}, \tag{2.4}$$

where c is the speed of light in vacuum. Now by applying continuity of the electric field parallel to the interface we find

$$\frac{\mathrm{k}_{\mathrm{z},2}}{\epsilon_2}+\frac{\mathrm{k}_{\mathrm{z},1}}{\epsilon_1}=0, \tag{2.5}$$

which is the condition for the existence of a surface wave. It is apparent that the evanescent solution is only supported if the sign of the dielectric function changes over the interface. In addition by applying the Helmholtz equation in both halfspaces we

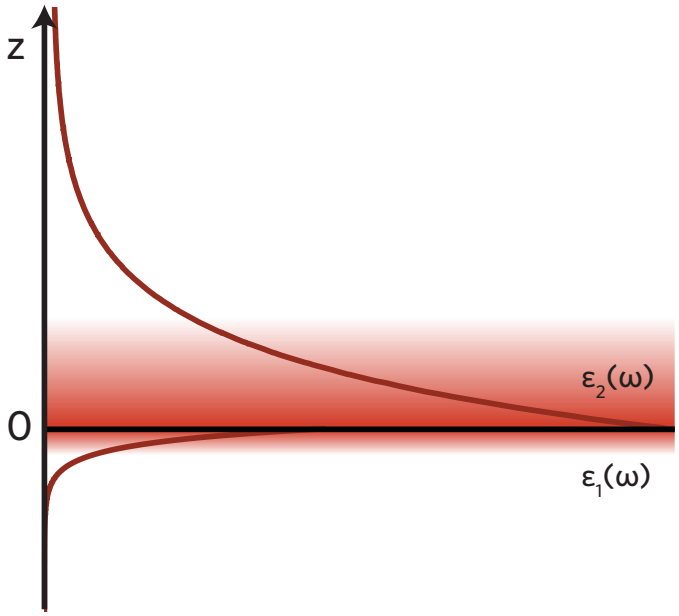


Figure 2.1: An illustration of the planar interface located at $z=0$ between two semi-infinite dielectrics characterised by $\epsilon_1(\omega), \epsilon_2(\omega)$. The field intensity for an evanescent solution to Maxwell's equations is illustrated by the curves.

find

$$k_{\parallel}^2 - k_{z,1}^2 = \epsilon_1 k_0^2, \tag{2.6}$$
$$k_{\parallel}^2 - k_{z,2}^2 = \epsilon_2 k_0^2, \tag{2.7}$$

where k_0 is the wavevector in vacuum. This allows for calculation of the surface wave dispersion as

$$k_{\parallel}^2 = k_0^2 \frac{\epsilon_1 \epsilon_2}{\epsilon_1 + \epsilon_2}. \tag{2.8}$$

This scheme has two benefits. Firstly, the wave is confined evanescently out-of plane as a result of its imaginary out-of plane wavevector $k_{z,i}$ resulting in sub-diffraction confinement around the interface at $z=0$. In addition to this, a higher in-plane spatial frequency bandwidth is achieved by Eq. 1.4 as a result of the imaginary k_z. Physically the evanescent out-of plane confinement is a result of coupling to the longitudinal and transverse resonances of the $\epsilon<0$ halfspace and the in-plane confinement is a result of the increased momentum of the matter-coupled photons.

2.1.2 Plasmonics

The materials most commonly used to supply a negative dielectric function are metals. These are well described by the Drude model for a free electron gas. The resulting dielectric function $\epsilon(\omega)$ is given by

$$\epsilon(\omega) = 1 - \frac{\omega_p^2}{\omega^2 + i\gamma_p\omega}, \tag{2.9}$$

where ω_p is the bulk plasma frequency of the metal, ω is the oscillation frequency and γ_p is the relaxation rate. This description of a metal adequately describes metals at frequencies in the near-infrared where inter-band transitions in the material may be neglected. The dielectric function of a metal is shown in Fig. 2.2(a), it is negative below the plasma frequency. This shows why metals are useful spectrally, the cutoff for evanescent behaviour normally lies in the ultraviolet (UV) portion of the spectrum meaning evanescent fields can be generated across the infrared (IR), visible and near UV parts of the optical spectrum. This is illustrated in Fig. 2.2(b) where the evanescent surface plasmon dispersion is indicated by the lower solid curve curve as calculated from Eq. 2.8. It persists up until the asymptotic frequency given by $\omega_p/\sqrt{2}$.

Experimental conditions for observation of plasmons at planar interfaces were postulated theoretically by Ritchie in 1957 [13] and observed two years later by electron energy loss spectroscopy of thin metal films [14, 15]. Metallic spheres are also exactly described in the Mie approximation supporting, in the non-retarded limit a dipolar resonance on fulfilment of the Fröhlich condition $\epsilon(\omega) = -2$, this resonance is size invariant and has been known since 1949 [16]. More recently the morphological nature of plasmonic resonances has made them a vital area of research [17]. This was instigated by proof of concept works on subdiffraction waveguiding in silver nanowires [18] and nanofocussing by metallic wedges [19] in addition to Ebbesen's observations of extraordinary optical transmission through silver hole arrays [20]. More recently new chemical synthesis procedures allowing for construction of user defined metallic geometries such as disks, cubes, rings and shells and submicrometer lithographic methods for creating easily measurable arrays have allowed these concepts to be exploited more successfully. In addition numerical methods, have also been developed to improve our understanding of the resonances of structures without closed form analytical solutions.

The limit of plasmonic confinement of light is ultimately limited by the electrons themselves, in sub$-$10nm geometries electron-electron interactions cause a smearing of the otherwise tightly confined fields [21]. More generally the electronic component of a plasmon is highly lossy. This is problematic as in very small resonators energy is

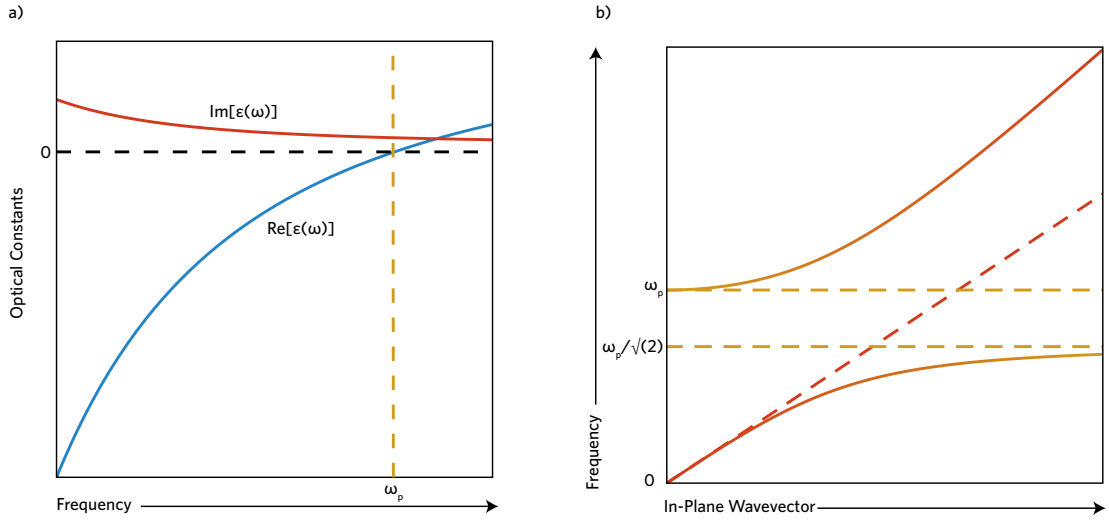


Figure 2.2: a) The real (blue) and imaginary (red) components of the dielectric function given in Eq. 2.9 are plotted. The real component intersects the zero line at the plasma frequency. This marks the end of evanescent wave behaviour. The plasma frequency is indicated by the yellow dashed line. b) The dashed lines represent the plasma frequency (yellow) and free photon dispersion (red). The solid lines represent the coupled modes, the lower of which is the surface plasmon polariton (SPP) and the upper of which is the plasma shifted photon. The coupled modal content is indicated by the line colour.

expected to spend half its time in the electronic component and its dissipation rate will therefore be consummate with that of the electronic component. There are a plethora of ways the energy quanta can decay to an electron-hole pair, either by phonon-assisted absorption, Umklapp electron-electron scattering, interband absorption or in small resonators Landau damping assisted by the high spatial frequencies present in the mode [22]. These processes occur on the 10-fs timescale. The loss may be partially overcome through clever resonator design with recent works having utilised hybrid plasmonic modes to draw the field away from the lossy metal through the use of gap modes generated by strong displacement currents in closely spaced dimers [23] or nanowire waveguides [24]. However generally this means that plasmonics systems present a poor route towards enhancing already efficient processes as any field enhancements are offset by metal loss [25].

Other ways to mitigate loss have been proposed: firstly plasmonics experiments could merely be moved into the infrared where losses are lower [26]. This however negates some of the advantages of utilising plasmonics for light confinement. As the driving frequency falls the real component of the dielectric function, while remaining negative, increases in magnitude. This means that the surface mode dispersion calculated by Eq. 2.8 tends toward the light line and the confinement drops. The incorporation of gain media into plasmonic architectures has been investigated [27], this resulting in complex fabrication and enhanced noise. Other proposals include using graphene [28], metal alloys [29] or highly doped semiconductors [30] however these systems are still fundamentally limited by electron scattering and although the absolute loss rate in these systems is lower than in metals due to the lower electron density, the operational frequency also falls for the same reason. These systems offer useful ways to extend the range of plasmonics into the mid-infrared but do not offer an increase in the quality factors achievable. The problem has also been proposed to lie purely with the metals we have. One route to low-loss is to fabricate a new metal with lattice constant approximately twice that of the original so as to blue shift the second conduction band. At frequencies where loss arises from interband transitions this would eliminate the states where electrons coupled to light can scatter [31]. Although the lossy nature of plasmons may be interesting for certain uses [32] for many others it is a limiting issue.

2.2 Surface Phonon Polaritons

Metals are the most common means of achieving a negative dielectric function but they are not the only way of doing so. Polar dielectrics are described by the dielectric

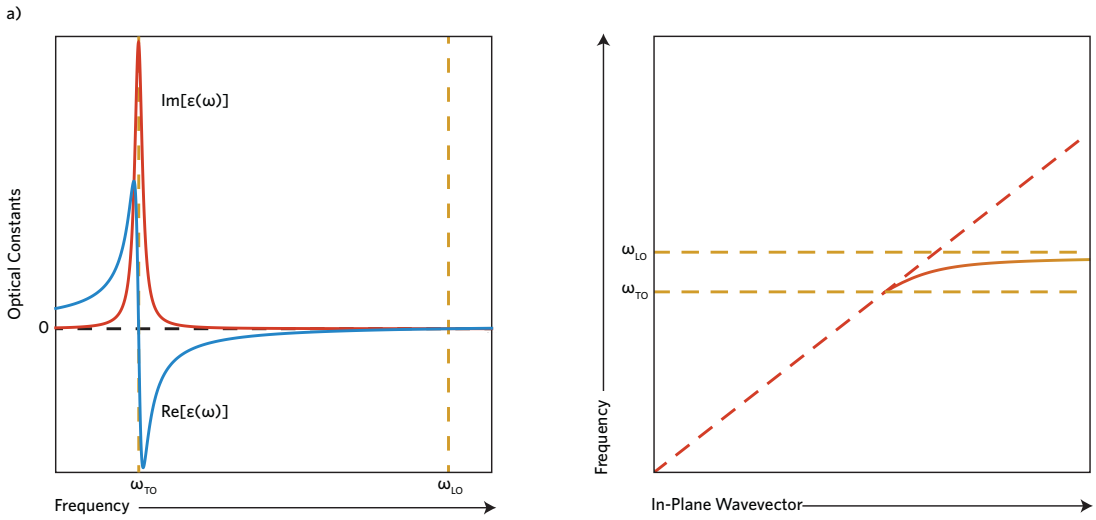


Figure 2.3: a) The real (blue) and imaginary (red) components of the dielectric function given in Eq. 2.10 are plotted. The yellow dashed lines indicate the LO and TO phonon frequencies. b) The dashed lines represent the optical phonon frequencies (yellow) and free photon dispersion (red). The solid line represents the SPhP dispersion with modal content as indicated by the line colour..

function derived from a Lorentz model for the ions

$$\epsilon\left(\omega\right)=1+\frac{\omega_{\mathrm{L}}^{2}-\omega_{\mathrm{T}}^{2}}{\omega_{\mathrm{T}}^{2}-\omega^{2}+i\gamma\omega}, \tag{2.10}$$

where γ is the relaxation rate. The frequencies ω_{T} and ω_{L} are the transverse optic (TO) and longitudinal optic (LO) phonon frequencies corresponding to out-of-phase oscillations of the lattice with wavevectors parallel and perpendicular to the applied field respectively. The dielectric function of a polar dielectric is plotted in Fig. 2.3(a), the real component being negative between the TO and LO phonon frequencies in a region termed the 'Reststrahlen' band [33]. Here the crystal does not permit radiation to propagate, entirely analogous to highly reflective metals below the plasma frequency. The dispersion relation for an evanescent mode at a planar polar dielectric/ vacuum interface is again calculable by use of Eq. 2.8 and is plotted in Fig. 2.3(b). The evanescent solution only exists within the Reststrahlen band and exhibits the same character as the surface plasmon polariton lying outside the lightline. This surface mode is termed a surface phonon polariton (SPhP).

It is informative to consider the origin of the terms within the dielectric function so as to understand how to choose an appropriate material system for a given application.

Optic phonon frequencies $\omega_{\mathrm{T}}, \omega_{\mathrm{L}}$ are predominantly determined by the mass of the lighter atomic species and the strength of their bonding. This is understandable from a 'toy' model of phonons in a diatomic one dimensional chain made up of alternating atoms of mass m_1 and m_2 where $m_1 > m_2$ which interact harmonically with force constant α. We describe the atomic displacements u_n as

$$u_{2n} = A_1 e^{i(2nqa-\omega t)}, \tag{2.11}$$

$$u_{2n+1} = A_2 e^{i((2n+1)qa-\omega t)}, \tag{2.12}$$

where atoms of mass m_1 are located at sites labelled 2n and those of mass m_2 are located at sites labelled 2n+1. Here the excitation wavevector is q, frequency is ω, the atomic spacing is a and A_1, A_2 are constants to be determined. In a tight-binding approximation the equations of motion are given by

$$m_1 \frac{\partial^2 u_{2n}}{\partial t^2} = \alpha \left(u_{2n+1} + u_{2n-1} - 2u_{2n}\right), \tag{2.13}$$

$$m_2 \frac{\partial^2 u_{2n+1}}{\partial t^2} = \alpha \left(u_{2n+2} + u_{2n} - 2u_{2n+1}\right), \tag{2.14}$$

and now by eliminating the amplitude constants A_1, A_2 we find the dispersion relation for the atomic vibrations as

$$\omega^2 = \alpha \left(\frac{1}{m_1} + \frac{1}{m_2}\right) \pm \alpha \left[\left(\frac{1}{m_1} + \frac{1}{m_2}\right)^2 - \frac{4\sin^2 qa}{m_1 m_2}\right]^{0.5}. \tag{2.15}$$

The resulting phonon dispersion is shown in Fig. 2.4a) for $m_1 = 2m_2$. Two phonon branches are clearly visible. Alternatively if $m_1 = m_2$ as in Fig. 2.4b) the optic-acoustic splitting disappears. The upper branch corresponds to the optical phonon branch and has frequency

$$\omega_\Gamma^{\mathrm{O}} = \sqrt{2\alpha \left(\frac{1}{m_1} + \frac{1}{m_2}\right)}, \tag{2.16}$$

at the zone centre point Γ. Here we see that stronger force constants result in larger frequencies and heavier atoms give smaller frequencies. Materials with light constituent atoms like SiC [34–37] or hexagonal BN [38–41] typically result in high optical phonon frequencies in the mid-infrared (mIR) spectral region. This spectral region is interesting for multiple reasons, as the mIR contains infrared active vibrational fingerprints that could be utilised to detect trace elements of chemicals. The infrared atmospheric window lies from $8 \rightarrow 12\mu$m, thus the development of free space optical systems in this region is highly desirable. In addition, room-temperature black body radiation peaks

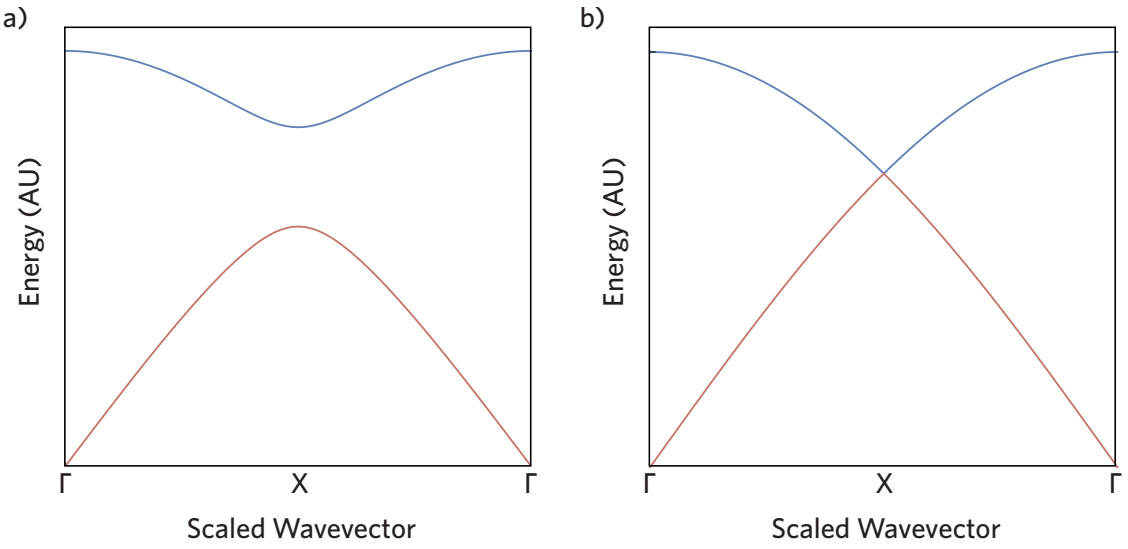


Figure 2.4: Blue lines correspond to optic phonon excitations where adjacent atoms move out of phase and the red to acoustic where adjacent atoms oscillate in phase. The x-axis is labelled by the symmetry points of the lattice. Disperesions are shown for a) Diatomic chain of mass $m_1 = 2m_2$, b) Monoatomic chain of mass $m_1 = m_1$.

in this window. Alternatively those with heavier constituent atoms such as GaAs [42, 43] or InP [44] typically give lower frequencies lying out in the terahertz region with this spectral window containing many interesting molecular rotational transitions.
The existence of SPhP modes is dependant upon the splitting of the LO and TO phonon frequencies. In a non-polar crystal like Si there is no charge transfer between the atoms that make up its covalently bonded zincblende crystal structure. In a polar semiconductor like GaAs however the ionic bonding results in electron transfer from the group V arsenic to the group III gallium atoms. In SiC the bonding is not ionic, being between two group IV atoms and nstead the polar nature of the crystal arises from the asymmetry of the valence charge density of the bonds [45]. In order to describe the interaction of such polar materials with an electromagnetic field it is necessary to augment the diatomic model presented. Denoting the relative charge of adjacent atoms by e^* the atomic equations of motion are now

$$m_1 \frac{\partial^2 u_{2n}}{\partial t^2} = \alpha \left(u_{2n+1} + u_{2n-1} - 2u_{2n}\right) + e^* E, \tag{2.17}$$

$$m_2 \frac{\partial^2 u_{2n+1}}{\partial t^2} = \alpha \left(u_{2n+2} + u_{2n} - 2u_{2n+1}\right) - e^* E, \tag{2.18}$$

where E is the electric field and we have taken a long wavelength approximation in stating that the electric field is constant. This long wavelength limit corresponds to

$q \rightarrow 0$ and therefore we are evaluating at the Γ point and now we no longer need to distinguish atomic sites, as all atoms are displaced equally. Separating variables yields

$$\left(\omega_0^2 - \omega^2\right) u_1 = \frac{e^* E}{m_1}, \tag{2.19}$$

$$\left(\omega_0^2 - \omega^2\right) u_2 = -\frac{e^* E}{m_2}, \tag{2.20}$$

where the frequency ω_0 is just the zone centre optical phonon frequency in the absence of Coulomb interactions found in Eq. 2.16. We can find the electrical polarisation produced by such a chain by

$$P = \frac{Ne^* u}{\epsilon_\infty} = \frac{1}{\epsilon_\infty} \frac{Ne^{*2}}{\omega_0^2 - \omega^2} \left(\frac{1}{m_1} + \frac{1}{m_2}\right) E, \tag{2.21}$$

where the relative displacement $u = u_1 - u_2$, ϵ_∞ is the high frequency dielectric constant and N is the atomic density.
If we now assume a transverse electric field, the polarisation relates to the electric field by

$$P = \frac{1}{\epsilon_\infty} \frac{Ne^{*2}}{\omega_T^2 - \omega^2} \left(\frac{1}{m_1} + \frac{1}{m_2}\right) E, \tag{2.22}$$

and by application of the electromagnetic wave equation

$$\frac{\partial^2 D}{\partial t^2} = c^2 \nabla^2 E, \tag{2.23}$$

$$\omega^2 \left(E + 4\pi P\right) = c^2 q^2 E, \tag{2.24}$$

and solving in conjunction with the atomic equation of motion Eq. 2.21 at the $q = 0$ point we can find a root at $\omega = 0$ corresponding to the acoustic phonon and one at

$$\omega^2 = \omega_T^2 + 4\pi \frac{Ne^{*2}}{\epsilon_\infty} \left(\frac{1}{m_1} + \frac{1}{m_2}\right) = \omega_L^2. \tag{2.25}$$

The polarity of the atomic bonding then results in a splitting between the previously degenerate longitudinal and transverse phonon frequencies as a result of long-range Coulomb interactions. The Coulomb field hybridises with the transverse optic phonons which depresses their frequency, splitting them from the longitudinal optic phonons. This effect results in the 'Reststrahlen' or forbidden band between ω_T and ω_L. Now we

can trivially find the dielectric function $\epsilon(\omega)$ as

$$\epsilon(\omega)=\frac{\mathrm{D}}{\mathrm{E}}=1+\frac{4\pi \mathrm{P_e}}{\mathrm{E}}+\frac{4\pi \mathrm{P}}{\mathrm{E}}, \tag{2.26}$$

where the electronic polarisation is indicated by $\mathrm{P_e}$. As usual we define the high-frequency dielectric constant as

$$\epsilon_\infty=1+\frac{4\pi \mathrm{P_e}}{\mathrm{E}}, \tag{2.27}$$

and can calculate the static dielectric constant

$$\epsilon_0=\epsilon_\infty+\frac{4\pi}{\omega_\mathrm{T}^2}\frac{\mathrm{Ne}^{*2}}{\epsilon_\infty}\left(\frac{1}{\mathrm{m}_1}+\frac{1}{\mathrm{m}_2}\right), \tag{2.28}$$

giving the total dielectric constant of the medium as

$$\epsilon(\omega)=\epsilon_\infty+\frac{\omega_\mathrm{T}^2(\epsilon_0-\epsilon_\infty)}{\omega_\mathrm{T}^2-\omega^2}. \tag{2.29}$$

The splitting of longitudinal and transverse optical phonons is determined by the condition that $\epsilon(\omega_\mathrm{L})=0$, which results in the Lyddane-Sachs-Teller relation [46]

$$\omega_\mathrm{L}^2=\frac{\epsilon_0}{\epsilon_\infty}\omega_\mathrm{T}^2. \tag{2.30}$$

This determines the bandwidth over which SPhPs are supported. The effect of polar bonding is illustrated by the presence of splitting in the polar 3C-SiC phonon dispersion and its absence in the monoatomic Si phonon dispersion (Fig. 2.5).

In a high quality crystal, the SPhP modal lifetime is usually related to the characteristic timescale of intrinsic anharmonic 3 phonon scattering [49] whose rate is dependant upon the ability of the available scattering proccesses to satisfy energy and momentum conservation laws

$$\omega_\mathrm{i}(\mathbf{q})\pm\omega_{\mathrm{i}'}(\mathbf{q}')=\omega_{\mathrm{i}''}(\mathbf{q}''), \tag{2.31}$$

$$\mathbf{q}\pm\mathbf{q}'=\mathbf{q}''+\mathbf{G}, \tag{2.32}$$

where $\mathbf{G}$ is a reciprocal lattice vector, the vectors $\mathbf{q},\mathbf{q}',\mathbf{q}''$ refer to the momentum of the three phonons, frequencies of the three phonons are $\omega_\mathrm{i}(\mathbf{q}),\omega_{\mathrm{i}'}(\mathbf{q}'),\omega_{\mathrm{i}''}(\mathbf{q}'')$ and the index i refers to the type of phonon mode. Higher order processes involving more phonons are also possible and may become important in crystals with strong limitations

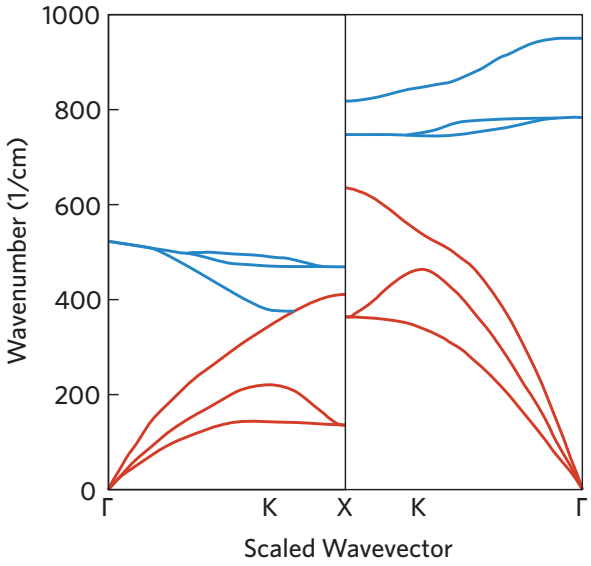


Figure 2.5: The phonon dispersions of Si (adapted from [47]) (left) and 3C-SiC (adapted from [48]) (right). Blue lines represent optical modes and red lines acoustic modes. The SiC exhibits an LO-TO phonon splitting as a result of the polar nature of the diatomic crystal and a TO-LA gap due to the difference in the constituent masses.

on the three phonon scattering phase space, four phonon processes typically occur on timescales around 100 times slower than three phonon processes [50]. Three processes are possible, either OOO, OOA or OAA scattering (A referring to acoustic and O to optical phonons). Generally three optical phonon scattering is disallowed entirely by energy conservation as the phonon splitting defined by Eq. 2.30 is less than the TO phonon frequency. OAA scattering can be dominant in certain materials, but can be severely limited in some classes of polar materials with a large acoustic-optic phonon gap. Such a gap is expected in materials with large differences in mass between the diatomic species as can be seen from consideration of the phonon frequencies of a 1D diatomic chain considered earlier

$$\omega_{\chi}^{\mathrm{A}} = \sqrt{\frac{2\alpha}{\mathrm{m}_1}}, \tag{2.33}$$

$$\omega_{\chi}^{\mathrm{O}} = \sqrt{\frac{2\alpha}{\mathrm{m}_2}}, \tag{2.34}$$

$$\tag{2.35}$$

where $\omega_{\chi}^{\mathrm{A}}$ and $\omega_{\chi}^{\mathrm{O}}$ refer to the acoustic and optical phonon frequencies evaluated at the zone edge χ. In materials wherer the splitting $\omega_{\chi}^{\mathrm{A}} - \omega_{\chi}^{\mathrm{O}}$ is large this can severely restrict

the phase space available for OAA scattering and in some materials prohibit it entirely. Caldwell *et al.* calculate the rates for first-order anharmonic phonon scattering for a variety of polar semiconductors by the first principles approach presented by Lindsay [51]. They find that the materials with the longest optical phonon lifetimes are those with the largest mass differential between the diatomic constituents and attribute this to the reduced phase space for OAA scattering. The lifetime of the optical phonons is typically of the order 1ps [52] which exceeds that of free carriers in a metal by around two orders of magnitude [22, 53]. Realistic materials have additional extrinsic loss channels to which the above intrinsic process merely provide an upper bound. One source of loss is from high densities of point defects arising from a vacancy of one of the diatomic species [54] or an antisite vacancy where the constituents are swapped [55]. Extended defects can also limit the lifetime of optical phonons as can isotope scattering [56]. The effect of these is most pronounced for localised phonon polaritons, resulting a broadening of the resonance due to the decreased optic phonon lifetime. These effects however are highly material specific and will be discussed in-depth in a later section on specialising on a specific material system. Generally speaking these processes result in a decrease in the optic phonon lifetime from the theoretical limit given by the anharmonic three-phonon scattering rate. As these processes are extrinsic it is possible to limit them by improved fabrication and growth procedures [57].

2.2.1 A Thorough Review of Surface Phonon Polaritonics

We will break our discussion of recent advances in surface phonon polaritonics into two distinct sections: The localised phonon resonances of small polar dielectric nano particles and the propagative modes of waveguides or interfaces.

Localised Phonon Polaritons

Surface phonon polariton resonators may be compared to their plasmonic counterparts by consideration of spherical resonators in the non-retarded limit, a system which may be solved analytically [58]. These exhibit a size invariant resonance at the Frölich frequency ω_{F} where the condition $\mathrm{Re}\left[\epsilon\left(\omega\right)\right]=-2\epsilon_a$ is fulfilled [16] given by

$$\omega_{\mathrm{F}}=\sqrt{\frac{\omega_{\mathrm{L}}^2+\frac{2\epsilon_{\mathrm{a}}}{\epsilon_\infty}\omega_{\mathrm{T}}^2}{1+2\frac{\epsilon_{\mathrm{a}}}{\epsilon_\infty}}}, \tag{2.36}$$

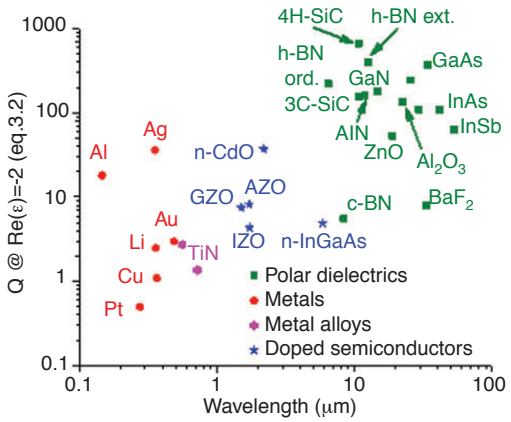


Figure 2.6: A comparison of the quality factors calculated by Eq. 2.37 for a variety of materials at the Fröhlich resonant frequency. Noble metals are indicated by red circles, metal alloys by purple hexagons, doped semiconductors by blue stars and polar dielectrics by green squares. Figure is reproduced from [52].

where ϵ_a is the ambient dielectric constant. At the Frölich resonance it is interesting to examine the modal quality factor Q given by [59]

$$\mathrm{Q}=\frac{\omega\frac{\mathrm{dRe}[\epsilon(\omega)]}{\mathrm{d}\omega}}{2\mathrm{Im}\left[\epsilon\left(\omega\right)\right]}\approx\frac{\omega}{\gamma}, \tag{2.37}$$

where the equality is valid if the reciprocal zone centre SPhP lifetime $\gamma\ll\omega_{\mathrm{T}},\omega_{\mathrm{L}}$. This equation is valid in the small particle limit for isolated particles. We saw earlier that SPhPs offer a reduction in damping of around two orders of magnitude while the driving frequency ω_{F} falls by around an order of magnitude. Additionally phononic materials exhibit stronger dispersion than metallic ones by a factor $\omega_{\mathrm{L}}/2\left(\omega_{\mathrm{L}}-\omega_{\mathrm{T}}\right)$. This results in possible quality factors in excess of 600 in 4C-SiC nanoparticles, where noble metal plasmonic structures and doped semiconductors can only achieve $\mathrm{Q}\approx40-60$, representative values for achievable quality factors are shown in Fig. 2.2.1 [52].

In addition, it is possible to relate the energy stored inside the resonator $\mathcal{U}_{\mathrm{in}}$ to that stored outside $\mathcal{U}_{\mathrm{out}}$ by

$$\frac{\mathcal{U}_{\mathrm{in}}}{\mathcal{U}_{\mathrm{out}}}=\frac{-1}{\epsilon\left(\omega\right)}\frac{\mathrm{d}\left(\omega\epsilon\left(\omega\right)\right)}{\mathrm{d}\omega}, \tag{2.38}$$

where the dispersive dielectric function $\epsilon\left(\omega\right)$ characterises the resonator material. Materials with a stronger dispersion will therefore store a larger proportion of the mode energy within the resonator. As the dielectric function depicted in Fig. 2.3 a) is essentially the metallic dielectric function depicted in Fig. 2.2 a) compressed between

the longitudinal and transverse optic phonon frequencies, the dispersion of the dielectric function for polar dielectrics in the Reststrahlen band typically exceeds that of a metal below the plasma frequency. At the Frölich resonance for a noble metal $\omega\frac{\mathrm{d}\epsilon(\omega)}{\mathrm{d}\omega}\approx 20-30$. Due to the enhancement in dispersion this gives $\omega\frac{\mathrm{d}\epsilon(\omega)}{\mathrm{d}\omega}\approx 60$ in 4H-SiC and $\omega\frac{\mathrm{d}\epsilon(\omega)}{\mathrm{d}\omega}\approx 150$ in GaAs. This means that more energy can be stored in the volume defined by the resonator.

These characteristics render phononic resonators excellent candidates for the confinement of light on the nanoscale. The first investigation of the optical properties of small phononic nanoparticles was carried out by Mutschke *et al.* who studied the resonances of SiC in a menagerie of particle shapes in a variety of polytypes both theoretically and experimentally by Fourier transform infrared microscopy in transmission mode of many particles dispersed in KBr pellets [35]. They found that the resonances observed did not correlate with the sample polytype, instead depending very strongly on the morphology of the particles and the presence of impurities. These localised resonances were exploited by Hillenbrand *el at* who scanned an unpatterned 4H-SiC surface utilising the platinum tip of a scattering scanning near-field optical microscope (s-SNOM) through which the sample is illuminated resonantly by a laser [36]. Back-scattered light was collected through a Cassegrain objective. A sharp enhancement in the scattered field is observed near the Fröhlich resonance corresponding to excitation of the image charge of the illuminating tip in the SiC. This amounts to the first observation of a sharp, single particle SPhP excitation. This concept was later extended to provide sub-wavelength in-plane confinement by patterning a sub-wavelength ($\lambda/50$) checkerboard by focussed ion beam implantation on a SiC substrate, effectively introducing defects to change the local dielectric function. Spatial near-field mapping revealed the electric field to be strongly confined to SiC regions which had not undergone implantation [60]. This was the first example of a subwavelength phonon-photonic fabricated structure. The near field interaction between s-SNOM tip and a planar SiC surface has also been investigated with the resonance in the scattered field observed to red shift as the tip moves toward the surface as a result of hybridisation with an image charge induced in the substrate [61]. This method was also utilised to map the structure and defects of an SiC crystal with a $\lambda/200$ spatial resolution [62]. A spectral shift in the scattering resonance at a boundary between 4H and 6H-SiC due to the change in crystal structure was observed as a contrast in the s-SNOM signal at fixed frequency. Superlensing through a hole array patterned in an SiC film [63] has also been demonstrated by directly mapping the image plane with an s-SNOM tip [64]. With this approach it was possible to resolve holes in the SiC film as small as $\lambda/20$.

Greffet *el al.* made the first demonstration of surface phonon assisted perfect infrared absorption by use of a ruled grating written into an SiC substrate [65]. The grating exhibited absorption dependent on the angle of excitation, a result of the interaction of the organ pipe modes of the striations with the surface mode of the substrate. In addition Kirchoff's law was demonstrated by measurement of the angle-resolved thermal emission which followed the same angular dependance as the absorption. Similar results have been reported in the far-infrared utilising gallium phosphide [66]. Greffet's results led to the work of Schuller *et al.* who utilised long, SiC wires with a sub-wavelength cross section of 1μm [67]. Extinction measurements show four antenna modes which agree well with those predicted by electrostatic theory. In addition the thermal emissivity of the wires was studied and seen to overlap with the absorption, again demonstrating Kirchoff's law and presenting the possibility of sub-wavelength thermal sources in the mid-infrared. Since then a large area meta-surface made up of SiC antennas subwavelength in three dimensions has been demonstrated [68]. The resonances observed in reflection were compared to those predicted utilising finite element simulations and Kirchoff's law was demonstrated by comparison with the thermal emission.

Phononic resonances have also been exploited for a host of other purposes. Enhanced infrared absorption was demonstrated by coating subwavelength SiC spheres with anthracene [69], here a near-field absorption enhancement of around 100 times is estimated in the vicinity of the localised phonon resonances of the spheres. Surface phonon assisted heat transfer has been experimentally demonstrated across a nanoscale gap between a silica sphere and substrate, exceeding predictions by Planck's blackbody radiation by three orders of magnitude [70]. Finite element simulations have also suggested that the optical forces in SiC nanostructures could exceed those in comparable plasmonic structure by up to two orders of magnitude making these structures a promising system for infrared optomechanics [71].

Recent advances have allowed for lithographic fabrication of SPhP resonances with a priori defined resonances. Firstly Caldwell *et al.* demonstrated the fabrication of cylindrical 6H-SiC resonator arrays on an SiC substrate with resonances tuneable by the cylinder free parameters and the array periodicity [2]. This was the first demonstration of LSPhP resonators, sub-wavelength in all three dimensions. The resonances as measured by Fourier transform infrared spectroscopy have narrow linewidths ($7-25$/cm) with corresponding Q factors exceeding the theoretical limit for plasmonic structures (45-135). Further studies have achieved quality factors in excess of 250 [3] and field enhancement factors in excess of 5000 are calculated numerically. Similar results have

been observed in arrays of cylindrical GaN resonator [72]. High quality factors (>60) were also found in SNOM scans of an SiC substrate through a metallic hole array [73].

2.2.2 Propagative Phonon Polaritons

A figure of merit for the propagating surface plasmon at a planar interface is given as the ratio of propagation length to vertical confinement [74]. On comparing for surface plasmon polaritons at metal interfaces and surface phonon polaritons it is found that the phonons offer no improvement over the plasmons [52]. This is especially true when the use of metal-insulator-metal waveguides are considered as these allow for arbitrary out-of-plane confinement even in the mid-infrared where natural plasmonic confinement is weak. Although the phonon polariton lifetime exceeds that of the plasmon polariton the strong dispersion of the dielectric function means that the SPhP group velocity v_g

$$v_g = \frac{d\omega}{dk}, \tag{2.39}$$

is much lower than the plasmonic case.
Despite this, propagating SPhPs have been demonstrated. Laser excitation of SPhPs at a flat SiC interface was observed in the Otto configuration consisting of a prism separated from the SiC surface by a narrow air gap (5μm). The laser beam undergoes total internal reflection at the prism/ air interface exciting evanescent fields in the air which can couple to the SPhP, critical coupling was demonstrated [75]. Real space imaging of propagating SPhPs was first carried out by Huber *et al.* [76]. SPhPs are excited by edge diffraction from an illuminated gold film deposited on an SiC substrate. The SPhP propagates to a SNOM tip placed a distance away, this scatters the SPhP field by the image charge process described in the prior section. By scanning the tip it is possible to map out the SPhP field distribution in real space and by changing the illumination angle to alter the in-plane wavevector the dispersion can be mapped. This was later extended to image focussing of SPhPs utilising a gold lensing element deposited on an SiC substrate [77]. Suspended n-type InP waveguides on InGaAs substrates have also been demonstrated [78].

Chapter 3

Surface Phonon Polariton Resonators

In the last few years it has become possible to fabricate user defined polar dielectric resonators which are sub-wavelength in all three dimensions [2, 3, 41, 72] . The strong field localisations achievable in these systems have potential application both in the sensing of molecules through surface enhanced infrared absorption spectroscopy, in super-resolution imaging or as non-linear optical devices. A deep understanding of the resonator modes is necessary to achieve these goals and allow for design of practical devices with user defined characteristics. This presents a challenge compared to plasmonic analogues because polar dielectric resonators are usually fabricated by etching on same material substrates which also support propagative resonant modes in the Reststrahlen band. In this chapter we address this problem by studying the illustrative system of square arrays of cylindrical SiC resonators on a planar SiC substrate. Beginning with a numerical finite element method (FEM) investigation we consider the resonators as an open system and find the complex resonant frequencies corresponding to their quasi-normal modes in Sec. 3.1. This implementation is described in Sec. 3.1.1. and allows us to investigate the figures of merit for isolated SiC resonators. We then build a coherent model allowing for interactions of the localised resonators with a planar substrate by studying the modes of an isolated resonator above an SiC surface. Finally square arrays of resonators on the substrate surface are analysed by application of Bloch-Floquet boundary conditions to the simulation sidewalls and the coupling between the Bloch-folded delocalised SPhP of the interface and the localised modes of the resonator is studied resulting in the formation of strongly dispersive Bloch-polaritons. Finally we present an experimental analysis of the coupling between the delocalised and localised modes in Sec. 3.2.

3.1 Finite Element Simulations of Silicon Carbide Pillars

3.1.1 Modelling Strategy

Isolated cylindrical resonators have a 2D parameter space defined by height h and diameter d. In the asymptotic case $h \to \infty$ there is an analytical solution, the resonator supports a predictable series of TM and TE polarised resonances characterised by their azimuthal phase dependancy [58, 67]. In the limit of finite $h \gg \lambda$ easily understood Fabry-Pérot resonances are supported along the wire length [79]. In the limit considered by Caldwell *et al.* the cylinders are deep-subwavelength in both h and d ($h \ll \lambda$, $d \ll \lambda$), this system has no closed-form analytical solution and require the use of numerical methods. We utilise the finite element solver COMSOL multiphysics to numerically solve the system [2].
It is instructive to initially consider what defines the cavity modes under study. In the finite element solver we find time harmonic solutions to the sourceless Maxwell equations of form

$$\mathbf{E}(\mathbf{r}, t) = \mathbf{E}(\mathbf{r}, \omega)\, e^{-i\omega t}, \tag{3.1}$$

where the position dependant electric field $\mathbf{E}(\mathbf{r}, \omega)$ solves the electromagnetic wave equation

$$\nabla \times \nabla \times \mathbf{E}(\mathbf{r}, \omega) - k^2 \boldsymbol{\epsilon}(\mathbf{r}, \omega)\, \mathbf{E}(\mathbf{r}, \omega) = 0, \tag{3.2}$$

where $k = \omega/c$ is the ratio of the angular momentum and speed of light in vacuum and $\boldsymbol{\epsilon}(\mathbf{r}, \omega)$ is the position dependant dispersive dielectric tensor. This equation does not have well defined modal solutions. In order to achieve these we also need to impose an appropriate boundary condition on the system, for the system of isolated resonators in a homogeneous background of dielectric constant $\epsilon_B = n_B^2$ we utilise the Silver-Müller radiation condition [80]

$$\hat{\mathbf{r}} \times \nabla \times \mathbf{E}(\mathbf{r}, \omega) + i n_B k \mathbf{E}(\mathbf{r}, \omega) \to 0 \qquad \text{as} \qquad |\mathbf{r}| \to \infty, \tag{3.3}$$

where $\hat{\mathbf{r}}$ is a unit vector pointing in the direction of the radial coordinate $\mathbf{r}$. The application of the radiation condition means that even in case of lossless media ($\mathrm{Im}[\boldsymbol{\epsilon}(\mathbf{r}, \omega)] = 0$) the wave Eq. 3.2 is non-Hermitian having eigensolutions $\mathbf{f}_n$ with discrete complex resonant frequencies $\tilde{\omega}_n = \omega_n - i\gamma_n$ and therefore finite quality factor

$$Q_n = \frac{\omega_n}{2\gamma_n}, \tag{3.4}$$

where the imaginary frequency $\gamma_n > 0$. The application of the Silver-Müller radiation condition then, results in leaky eigensolutions with the expected properties of our cavity modes. The modes of open systems which are non-conservative systems whose operators are non-Hermitian can be described in two ways. The traditional approach is to couple the system to a bath representing the modes of the universe to which the open system can couple. In this way the system taken as a whole is Hermitian and conservative and can be described in the framework of its normal modes [81]. Such a formalism is however cumbersome. A more natural approach to describe open systems is in the framework of quasi-normal modes (QNM) [82]. These are discrete modes of the open system which have a complex eigenfrequency as a result of the elimination of the bath degrees of freedom. The quasi-normal modes of the system are found to be complete under the conditions that a cavity is defined and that there is no mechanism by which energy can scatter back into the cavity.
Such a formalism is convenient however it presents two issues when it comes to electromagnetic modelling of such systems. Firstly, the modes of the resonators acquire complex wavevector $k_0 = k_0^R - ik_0^I$ meaning that at large distances the boundary condition requires outgoing solutions of form

$$\tilde{\mathbf{f}}(\mathbf{r}) \propto \frac{e^{ik_0 r}}{r}, \tag{3.5}$$

in three dimensions where $r = |\mathbf{r}|$ the solutions are divergent. This is illustrated by Kristensen *et al.* for the fundamental eigenmode of a plasmonic nanosphere dimer, such a divergence is not observed when evaluating the field scattered by a plane wave at real frequency [83]. This means that when we wish to calculate the cavity mode volume for a dipole located at $\mathbf{r}_C$ by the standard definition, as a measure of the ratio of the total energy present in the cavity mode and the electric field at $\mathbf{r}_C$

$$V_n^{eff} = \int_V \frac{\boldsymbol{\epsilon}(\mathbf{r}) |\tilde{\mathbf{f}}(\mathbf{r})|^2}{\boldsymbol{\epsilon}(\mathbf{r}_C) |\tilde{\mathbf{f}}(\mathbf{r}_C)|^2} dV, \tag{3.6}$$

the integral involved in the numerator is divergent.
We will solve this problem by following the intuitive approach of Sauvan *et al.* [84]. Firstly we consider a dipole source located at $\mathbf{r}_0$ in the vicinity of the optical resonator, its spontaneous decay rate Γ can be simply determined from Fermi's golden rule as

$$\Gamma = \frac{2}{\hbar} \mathrm{Im}\left[\mathbf{p}^* \cdot \mathbf{E}(\mathbf{r}_0)\right], \tag{3.7}$$

where $\mathbf{E}$ is the total electric field satisfying the Maxwell curl equations

$$\nabla\times\mathbf{E}=i\omega\boldsymbol{\mu}\left(\mathbf{r},\omega\right)\mathbf{H}, \tag{3.8}$$

$$\nabla\times\mathbf{H}=-i\omega\boldsymbol{\epsilon}\left(\mathbf{r},\omega\right)\mathbf{E}+\mathbf{j}, \tag{3.9}$$

with current source $\mathbf{j}=-i\omega\mathbf{p}\delta\left(\mathbf{r}-\mathbf{r}_0\right)$ where $\mathbf{p}$ is the dipole moment. Here $\boldsymbol{\mu}\left(\mathbf{r},\omega\right)$ is the permeability tensor. We now assume that the total field radiated by the dipole $\mathbf{E}\left(\mathbf{r},\omega\right)$ may be expanded on a finite set of quasi-normal modes of the resonator $\tilde{\mathbf{E}}_{\mathrm{n}}\left(\mathbf{r}\right)$

$$\mathbf{E}\left(\mathbf{r},\omega\right)\approx\sum_{\mathrm{n}}\alpha_{\mathrm{n}}\left(\omega\right)\tilde{\mathbf{E}}_{\mathrm{n}}\left(\mathbf{r}\right), \tag{3.10}$$

where $\alpha_{\mathrm{n}}\left(\omega\right)$ is a complex coefficient to be determined. This approximation is valid as long as the emitter emits predominantly into the cavity modes such as for emitters located in the near field of our phononic resonators. Now specialising onto reciprocal materials satisfying $\boldsymbol{\epsilon}=\boldsymbol{\epsilon}^{\mathrm{T}}$, $\boldsymbol{\mu}=\boldsymbol{\mu}^{\mathrm{T}}$ and utilising Lorentz reciprocity which relates two sets of solutions to Maxwell's equations $(\mathbf{E},\mathbf{H},\omega,\mathbf{j})$ and $(\mathbf{E}',\mathbf{H}',\omega',\mathbf{j}')$ and applying the divergence theorem to the vector product $\mathbf{E}'\times\mathbf{H}-\mathbf{E}\times\mathbf{H}'$ we find

$$\begin{aligned}\int\mathrm{dS}\left[\mathbf{E}'\times\mathbf{H}-\mathbf{E}\times\mathbf{H}'\right]=i\int\mathrm{dV}\Big[&\mathbf{E}\left(\omega\boldsymbol{\epsilon}\left(\omega\right)-\omega'\boldsymbol{\epsilon}\left(\omega'\right)\right)\mathbf{E}'\\&-\mathbf{H}\left(\omega\boldsymbol{\mu}\left(\omega\right)-\omega'\boldsymbol{\mu}\left(\omega'\right)\right)\mathbf{H}'-\left(\mathbf{j}\cdot\mathbf{E}'-\mathbf{j}'\cdot\mathbf{E}\right)\Big]=0,\end{aligned} \tag{3.11}$$

where the surface integral on the left is taken over the surface S enclosing the volume V. This is the unconjugated form of Lorentz's reciprocity. We apply this to two pairs of fields, the total field radiated by the dipole $(\mathbf{E},\mathbf{H},\omega,-i\omega\mathbf{p}\delta\left(\mathbf{r}-\mathbf{r}_0\right))$ and the nth QNM of the resonator $\left(\tilde{\mathbf{E}}_{\mathrm{n}},\tilde{\mathbf{H}}_{\mathrm{n}},\tilde{\omega}_{\mathrm{n}},0\right)$ yielding

$$-\omega\mathbf{p}\cdot\tilde{\mathbf{E}}_{\mathrm{n}}\left(\mathbf{r}_0\right)=\int\mathrm{dV}\Big[\mathbf{E}\left(\omega\boldsymbol{\epsilon}\left(\omega\right)-\tilde{\omega}_{\mathrm{n}}\boldsymbol{\epsilon}\left(\tilde{\omega}_{\mathrm{n}}\right)\right)\tilde{\mathbf{E}}_{\mathrm{n}}-\mathbf{H}\left(\omega\boldsymbol{\mu}\left(\omega\right)-\tilde{\omega}_{\mathrm{n}}\boldsymbol{\mu}\left(\tilde{\omega}_{\mathrm{n}}\right)\right)\tilde{\mathbf{H}}_{\mathrm{n}}\Big], \tag{3.12}$$

and utilising Eq. 3.10 we can write the linear system of equations

$$\sum_{m}\mathrm{A}_{\mathrm{nm}}\left(\omega\right)\beta_m\left(\omega\right)=-\omega\mathbf{p}\cdot\tilde{\mathbf{E}}_{\mathrm{n}}\left(\mathbf{r}_0\right), \tag{3.13}$$

where the coefficient

$$\mathrm{A_{nm}}\left(\omega\right)=\frac{1}{\omega-\tilde{\omega}_{\mathrm{m}}}\int\mathrm{dV}\left[\tilde{\mathbf{E}}_{\mathrm{m}}\left(\omega\boldsymbol{\epsilon}\left(\omega\right)-\tilde{\omega}_{\mathrm{n}}\boldsymbol{\epsilon}\left(\tilde{\omega}_{\mathrm{n}}\right)\right)\tilde{\mathbf{E}}_{\mathrm{n}}-\tilde{\mathbf{H}}_{\mathrm{m}}\left(\omega\boldsymbol{\mu}\left(\omega\right)-\tilde{\omega}_{\mathrm{n}}\boldsymbol{\mu}\left(\tilde{\omega}_{\mathrm{n}}\right)\right)\tilde{\mathbf{H}}_{\mathrm{n}}\right], \tag{3.14}$$

and $\beta_{\mathrm{m}}\left(\omega\right)=\left(\omega-\tilde{\omega}_{\mathrm{m}}\right)\alpha_{\mathrm{m}}\left(\omega\right)$ relates to the expansion coefficients. Now at $\omega=\tilde{\omega}_{\mathrm{n}}$ we see immediately that $\mathrm{A_{nm}}\left(\tilde{\omega}_{\mathrm{n}}\right)=0$ for $\mathrm{m}\neq\mathrm{n}$ and therefore the equation set reduces to

$$\mathrm{A_{nn}}\left(\omega\right)\beta_{\mathrm{n}}\left(\omega\right)=-\tilde{\omega}_{\mathrm{n}}\mathbf{p}\cdot\tilde{\mathbf{E}}_{\mathrm{n}}\left(\mathbf{r}_0\right), \tag{3.15}$$

and by the definition of $\beta_{\mathrm{n}}\left(\omega\right)$ we see that $\alpha_{\mathrm{n}}\left(\omega\right)$ must have a pole at $\omega=\tilde{\omega}_n$ with residue $-\tilde{\omega}_{\mathrm{n}}\mathbf{p}\cdot\tilde{\mathbf{E}}_{\mathrm{n}}\left(\mathbf{r}_0\right)/\mathrm{A_{nn}}\left(\omega\right)$. Therefore the complex coefficient is given by

$$\alpha_{\mathrm{n}}\left(\omega\right)=\frac{-i\omega\mathbf{p}\cdot\tilde{\mathbf{E}}_{\mathrm{n}}\left(\mathbf{r}_0\right)}{\left(\omega-\tilde{\omega}_{\mathrm{n}}\right)\int\mathrm{dV}\left[\tilde{\mathbf{E}}_{\mathrm{n}}\frac{\mathrm{d}\left(\omega\epsilon\right)}{\mathrm{d}\omega}\tilde{\mathbf{E}}_{\mathrm{n}}-\tilde{\mathbf{H}}_{\mathrm{n}}\frac{\mathrm{d}\left(\omega\mu\right)}{\mathrm{d}\omega}\tilde{\mathbf{H}}_{\mathrm{n}}\right]}+\mathrm{g_n}\left(\omega\right), \tag{3.16}$$

where $\mathrm{g_n}\left(\omega\right)$ is a non-resonant background contribution. Utilising this definition it is possible to calculate the enhanced spontaneous emission into a single QNM $\tilde{\mathbf{E}}_{\mathrm{n}}$ by Eq. 3.7

$$\frac{\Gamma}{\Gamma_0}=\frac{2}{\hbar\Gamma_0}\mathrm{Im}\left[\alpha_{\mathrm{n}}\left(\omega\right)\mathbf{p}^{*}\cdot\tilde{\mathbf{E}}_{\mathrm{n}}\left(\mathbf{r}_0\right)\right]. \tag{3.17}$$

which leads to

$$\frac{\Gamma}{\Gamma_0}=\mathrm{F_P}\frac{\omega_0^2}{\omega^2}\frac{\omega_0^2}{\omega_0^2+4\mathrm{Q}\left(\omega-\omega_0\right)^2}\left[1+2\mathrm{Q}\frac{\omega-\omega_0}{\omega_0}\frac{\mathrm{Im}\left[\mathrm{V}\right]}{\mathrm{Re}\left[\mathrm{V}\right]}\right], \tag{3.18}$$

where Γ_0 is the spontaneous emission rate of the dipole in free space and $\mathrm{F_P}$ is the Purcell enhancement factor for a dipole on resonance with the QNM given by

$$\mathrm{F_P}=\frac{3}{4\pi^2}\left(\frac{\lambda_0}{\mathrm{n}}\right)^3\mathrm{Re}\left[\frac{\mathrm{Q}}{\mathrm{V}}\right], \tag{3.19}$$

where λ_0 is the free space wavelength and n is the refractive index at the dipole spatial location. The mode volume is therefore given by

$$\mathrm{V}=\frac{\int\mathrm{dV}\left[\tilde{\mathbf{E}}_{\mathrm{n}}\frac{\mathrm{d}\left(\omega\epsilon\right)}{\mathrm{d}\omega}\tilde{\mathbf{E}}_{\mathrm{n}}-\tilde{\mathbf{H}}_{\mathrm{n}}\frac{\mathrm{d}\left(\omega\mu\right)}{\mathrm{d}\omega}\tilde{\mathbf{H}}_{\mathrm{n}}\right]}{2\epsilon_0\mathrm{n}^2\left[\tilde{\mathbf{E}}\left(\mathbf{r}_0\right)\cdot\mathbf{u}\right]}, \tag{3.20}$$

where the unit vector $\mathbf{u}$ is defined from by the dipole moment $\mathbf{p}=\mathrm{p}\mathbf{u}$. This mode volume reduces to the standard definition Eq. 3.6 in the conservative limit where the

system is closed and lossless. The presence of dissipation results in a complex mode volume and a non-Lorentzian spontaneous decay shape [84].
The form of the inner product for the QNMs derived by Sauvan is given by

$$\langle \tilde{\mathbf{E}}_{\mathrm{m}} | \tilde{\mathbf{E}}_{\mathrm{n}} \rangle = \int \mathrm{dV} \left[\tilde{\mathbf{E}}_{\mathrm{n}} \frac{\mathrm{d}\left(\omega\epsilon\right)}{\mathrm{d}\omega} \tilde{\mathbf{E}}_{\mathrm{n}} - \tilde{\mathbf{H}}_{\mathrm{n}} \frac{\mathrm{d}\left(\omega\mu\right)}{\mathrm{d}\omega} \tilde{\mathbf{H}}_{\mathrm{n}} \right], \tag{3.21}$$

or the numerator of the mode volume V. This however is not the only method to normalise the modes of an open optical system. Lai *et al.* derived a normalisation for QNMs in the dispersionless limit by treating the optical cavity as a perturbation on the modes of the universe [85]. By rewriting the magnetic field terms in Eq. 3.21 as a surface integral over the electric field correspondence can also be shown with this formalism [86]. More recently Muljarov derived a normalisation for leaky optical modes by expanding the system Green's function in terms of the QNMs and imposing the Silver-Müller radiation condition [87]. This result is more general as it naturally regularises the integral while the results of Sauvan and Lai require the integral to be regularised by the numerical solution for the fields. We utilise the normalisation of Sauvan, regularising our fields by use of a perfectly matched layer (PML) within the COMSOL simulation, this acts as a complex coordinate transform in Maxwell's equations [88]. Surrounding the simulation domain with a PML has two effects: Firstly it maintains the Silver-Müller radiation condition at the boundary of V_1 and secondly it forces the fields in V_2 to decay, converting radiative losses at the simulation bound to absorptive losses in the simulation domain. Sauvan showed that the inner product is invariant under the PML coordinate transform meaning that any PML in which fields fully decay before reaching the simulation edge can be utilised to truncate the simulation domain and correctly calculate the inner product Eq. 3.21 [84]. Under the appropriate choice of PML equivalence between the results of Muljarov and Sauvan has been shown [86, 87]. The importance of this regularisation may be seen by consideration of an alternative approach, specifically the 1D Green's function approach of Leung *et al.* [89] which was later extended to 3D [90]. A numerical implementation of this form was recently discussed [83]. Muljarov has since shown this approach to be invalid for modes without spherical symmetry due to the poor regularisation of the integral [87].

3.1.2 Pole Finding Procedure

We have derived the form of the complex coefficients α_{n} in the expansion of the total field over the quasi-normal modes Eq. 3.10 and found that it has a pole at $\omega = \tilde{\omega}_{\mathrm{n}}$.

Adopting a scattered field formalism we solve Maxwell's equations without the scatterer for a background field satisfying

$$\nabla \times \mathbf{E}_{\mathrm{b}} = -i\omega\mu_{\mathrm{b}}\mathbf{H}_{\mathrm{b}}, \tag{3.22}$$

$$\nabla \times \mathbf{H}_{\mathrm{b}} = i\omega\epsilon_{\mathrm{b}}\mathbf{E}_{\mathrm{b}} + \mathbf{J}\left(\mathbf{r}\right), \tag{3.23}$$

where $\epsilon_{\mathrm{b}}, (\mu_{\mathrm{b}})$ are the background permittivity (permeability) and $\mathbf{J}\left(\mathbf{r}\right)$ is the source term. In the presence of the scatterer we instead write

$$\nabla \times \mathbf{E} = -i\omega\mu\mathbf{H}, \tag{3.24}$$

$$\nabla \times \mathbf{H} = i\omega\epsilon\mathbf{E} + \mathbf{J}\left(\mathbf{r}\right), \tag{3.25}$$

and now we calculate the scattered fields $\mathbf{E}_{\mathrm{s}} = \mathbf{E} - \mathbf{E}_{\mathrm{b}}, \mathbf{H}_{\mathrm{s}} = \mathbf{H} - \mathbf{H}_{\mathrm{b}}$. As $\omega \to \tilde{\omega}_{\mathrm{n}}$ we know from the form of the $\alpha_{\mathrm{n}}\left(\omega\right)$ that the system response diverges. This means it is possible to find the complex resonant frequency $\tilde{\omega}_{\mathrm{n}}$ by fitting to a pole in the scattered field. To do this it is necessary to evaluate the COMSOL model at complex frequency, this is achieved by solving at a dummy frequency ω_{D} and rescaling the relative permeability to $\mu_{\mathrm{eff}}\left(\omega\right) = \mu\left(\omega\right)\omega/\omega_{\mathrm{D}}$ and permittivity to $\epsilon_{\mathrm{eff}}\left(\omega\right) = \epsilon\left(\omega\right)\omega/\omega_{\mathrm{D}}$ [91]. In addition an analytical dielectric function must be employed to allow for an analytical continuation to a complex argument.

By coupling the COMSOL finite element solver with Matlab we recursively solve Eq. 3.22-3.25 by fitting to the inverse of the scattered field evaluated at a point of interest for the mode under study. A point dipole source is used. It is assumed that the form of the inverse field component can be Padé approximated by

$$\mathrm{Z}\left(\omega\right) = \frac{\omega - \tilde{\omega}}{\mathrm{a}_0 + \mathrm{a}_1\omega} \tag{3.26}$$

which will be minimised by the fitting procedure following the method of Bai *et al.* [91].

Having evaluated the complex resonant frequency $\tilde{\omega}$ we can now evaluate quantities of interest by evaluating the fields at the slightly detuned frequency $\tilde{\omega}'$. Very near to the complex resonant frequency the expansion Eq. 3.10 can be assumed mono-modal and therefore the scattered fields $\mathbf{E}_{\mathrm{s}}$ will be linearly proportional to the true QNM fields $\tilde{\mathbf{E}}$. This means the mode volume may be calculated through Eq. 3.20 and the Purcell enhancement may also be calculated. The accuracy of the approximations entailed here may be tested by comparison with full vectorial simulations. This is shown in Fig 3.1 for a dipole source on resonance with the QNM of a cylindrical rod. The dipole

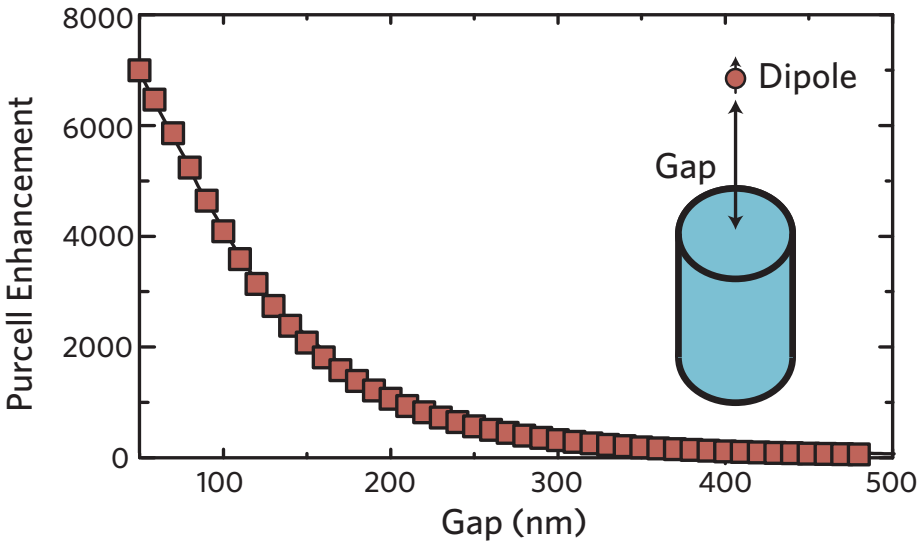


Figure 3.1: The Purcell enhancement for an electric dipole placed on axis above a cylinder of height 800nm and diameter 1000nm as the dipole-cylinder separation is scanned as illustrated. Geometrical singularities are smoothed with a 50nm radius of curvature. The black line shows results arising from the quasi-normal mode theory and the red squares full vectorial calculations of the dipole emission.

is located a distance gap above the end-facet of the rod and the gap is varied. Results calculated utilising the calculated QNM and Eq. 3.19 are shown by the black line, those calculated by full vectorial simulations of the power flow are shown by red squares. The semi-analytical theory reproduces the enhancement in the Purcell factor for near the resonator surface.

3.1.3 Modes of Isolated Cylindrical Resonators

The Fundamental Longitudinal Mode

The field profile for the lowest lying longitudinal mode are illustrated in the inset of Fig. 3.2 b). This mode is an azimuthally symmetric TM_0 mode and corresponds to the fundamental Fabry-Pérot mode of the resonator. This mode was first predicted by Takahara *et al.* for a sub-wavelength silver nanowire [18]. We investigate the real resonant frequency, calculated by the pole-finding procedure in the previous section, over two slices of the 2D parameter space defined by the cylinder height h and diameter d. Results are shown in Fig. 3.2 a). Red squares indicate variation of the cylinder height at constant d=800nm and blue circles indicate variation of the cylinder diameter

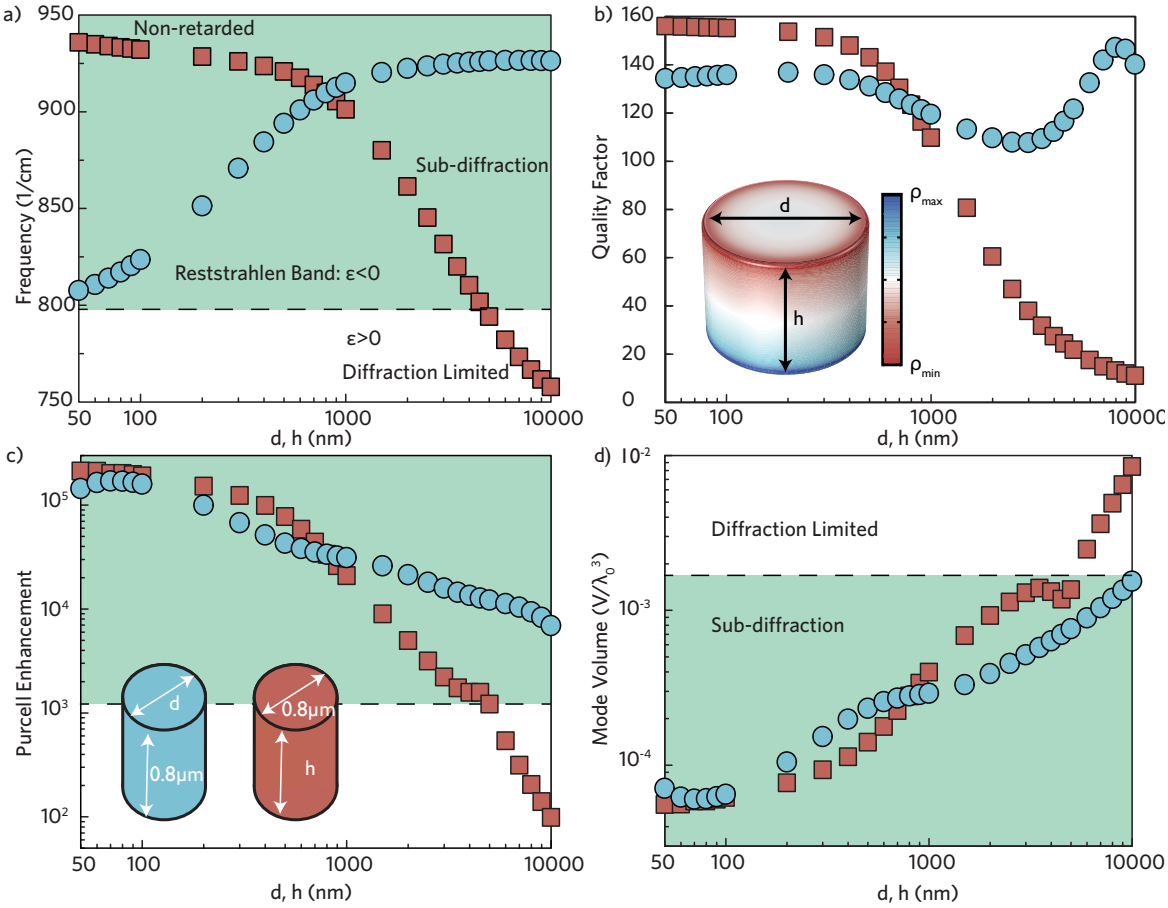


Figure 3.2: a) Real part of the resonant frequency of the longitudinal mode as a function of diameter at 800nm height (circles) and as a function of height at 800nm diameter (square). The three regimes discussed in the main text are indicated. The sub-diffraction modes are indicated by green shading. b) Quality factor of the longitudinal mode as a function of diameter at 800nm height (circles) and as a function of height at 800nm diameter (square). Inset shows the surface charge distribution of the mode. c) Purcell enhancement of the longitudinal mode as a function of diameter at 800nm height (circles) and as a function of height at 800nm diameter (square) d) Mode volume of the longitudinal mode as a function of diameter at 800nm height (circles) and as a function of height at 800nm diameter (square).

at constant h=800nm as shown in the inset. In the limit h/d→0 the resonant frequency trends to the asymptotic value ≈934cm^{-1} where for SiC Re$[\epsilon(\omega)]\approx-2$. For h→0 this corresponds to the non-retarded limit as indicated. As expected for a Fabry-Pérot resonance along the cylinder length increasing h results in a red shift of the resonant frequency, approximately proportional to 1/h. At around h=5μm the resonance leaves the Reststrahlen band. This results in a fundamental change in it's character, from an evanescent sub-diffraction mode to the diffraction limited mode of a high-index dielectric. Weaker dependance on the diameter of the resonator is observed as the mode is longitudinal with confinement predominantly dependant on the end-facet separation. We can evaluate the quality factor from the complex resonant frequency by Eq. 3.4. This is plotted over the same slices of the parameter space in Fig 3.2 c). In the non-retarded limit as a function of height a limit of around 160 is reached. As the cylinder height is increased Q decreases monotonically giving a smooth transition to the leaky, diffraction-limited mode at h=5μm.

We can calculate the Purcell enhancement by Eq. 3.19. Care must be taken when evaluating this expression. At distance z from the resonator surface a divergence in the Purcell factor is expected as 1/z^3 as a result of non-radiative decay [92]. Also in the limit of large emitter-resonator separation where the Purcell factor approaches unity, the approximation of predominant coupling to the resonator modes falls apart and coupling to the free-space continuum becomes significant. These effects can be included *a posteriori* if necessary through calculation of the QNM Green's function if necessary [93]. We elect not to do this and instead operate in the intermediate region, calculating the Purcell enhancement on a line 5nm from the resonator edge to ensure quenching effects are avoided. Results for the longitudinal mode are given in Fig. 3.2 c), the corresponding real component of the mode volumes are given in Fig. 3.2 d). As before three regimes are observed. In the small particle, non-retarded limit, the Purcell enhancements trend toward a limit of around 10^5 corresponding to an ultra-small mode volume of less than $10^{-4}(\lambda_0/\mathrm{n})^3$. This Purcell enhancement represents an order of magnitude improvement over the theoretical limit for plasmonics. Larger resonators see a monotonous fall in Purcell enhancement. The kink in the height-scanned Purcell enhancement and mode volume results near h=5μm is a result of the change in mode character from sub-diffraction to diffraction limited, these phases are illustrated by the shading of the plots.

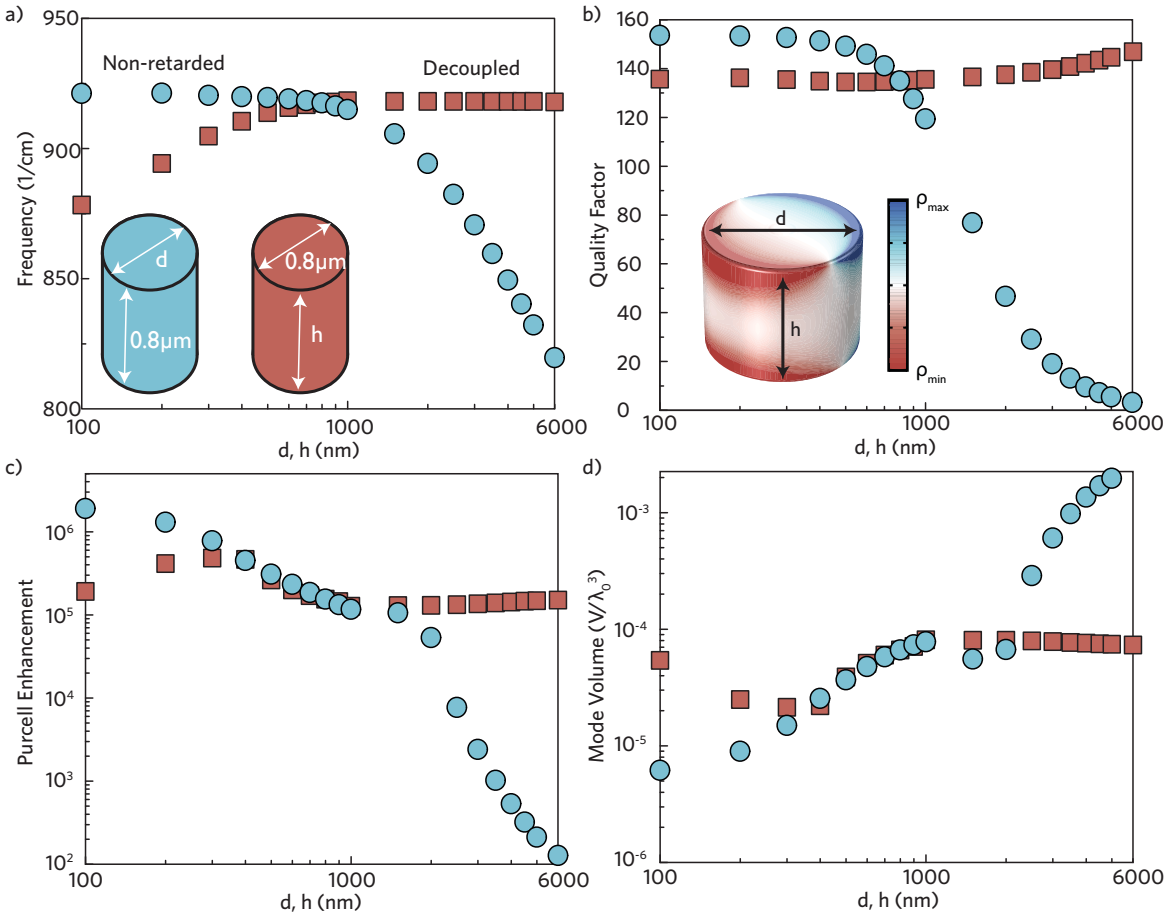


Figure 3.3: a) Real part of the resonant frequency of the transverse mode as a function of diameter at 800nm height (circles) and as a function of height at $800nm$ diameter (squares). The non-retarded and decouple limits are indicated b) Quality factor of the transverse mode as a function of diameter at 800nm height (circles) and as a function of height at $800nm$ diameter (squares). c) Purcell enhancement of the transverse mode as a function of diameter at 800nm height (circles) and as a function of height at $800nm$ diameter (squares) d) Mode volume of the transverse mode as a function of diameter at 800nm height (circles) and as a function of height at $800nm$ diameter (squares).

The Fundamental Transverse Mode

The fundamental transverse resonance electric field intensity is plotted in the inset of Fig. 3.3 b). The real resonant frequency is calculated by the pole fitting procedure outlined with results shown in Fig. 3.3 a). Two slices of the 2D parameter space are investigated, red squares indicate variation of the cylinder height at constant d=800nm and blue circles indicate variation of the cylinder diameter at constant h=800nm. The behaviour is entirely analogous to that observed for the longitudinal mode in Fig. 3.2 b) under the exchange of h and d. In the d/h$\rightarrow$0 limit the real modal frequency tends to the asymptotic value 923/cm corresponding to $\mathrm{Re}\left[\epsilon\left(\omega\right)\right]\approx-3$. In the small diameter, d$\rightarrow$0 limit this can be understood as the non-retarded limit where the entire resonator oscillates in phase. In the large height limit h$\rightarrow\infty$ the same result is achieved due to the decoupling of the transverse excitations at each end facet. In the large diameter limit the mode red shifts dramatically toward the transverse-optic phonon frequency where it will become a leaky, diffraction-limited mode. These trends are also observed in the quality factor calculations presented in Fig. 3.3b). In the small diameter limit the quality factor trends toward $\approx$920. For $d>$800nm the resonator is no longer in the non-retarded limit and the quality factor drops concurrent with the red shift in mode energy.

Purcell enhancement for the transverse mode is shown over the 2D parameter space in Fig. 3.3 c). As for the longitudinal mode in Fig. 5.1 c) stronger Purcell enhancements are typically seen in smaller geometries, in this case exceeding 10^6 for d=100nm, h=800nm. Two different regimes are apparent in the plots, in the non-retarded limit there is a gradual increase in Purcell factor (decrease in mode volume). On leaving this regime the Purcell factor drops rapidly (d>1000nm) due to the shift in mode energy toward ω_{T} which both results in increased optical loss and an increased in the proportion of the mode energy stored in ion potential energy. The peak result exceeds the plasmonic limit by two orders of magnitude, however remains around 1 order of magnitude less than that previously reported [2]. This could be a result of the radius of curvature chosen for the sharp cylinder vertices which has been observed to have a strong effect on the calculated Purcell enhancement. For our results the cylinder corners are smoothed with a 5nm radius of curvature.

The Effect of the Substrate

We have considered the morphological dependance of isolated cylindrical silicon carbide resonators. We studied the bright dipolar modes which couple strongly to plane-wave excitation. In reality the QNM spectrum of the resonator is made up of a selection of bright modes with a net dipole moment and dark modes without one [94]. For the isolated resonator these modes are decoupled and provide the complete set of QNMs in Eq. 3.10. Now we wish to place our cylinders onto a planar SiC substrate. The planar substrate supports a surface mode as discussed in Sec. 2.2 between the limiting frequencies ω_{L} and ω_{T} with dispersion relation

$$\mathrm{k}_{\parallel}=\frac{\omega}{\mathrm{c}}\sqrt{\frac{\epsilon\left(\omega\right)}{\epsilon\left(\omega\right)+1}}, \tag{3.27}$$

where $\mathrm{k}_{\parallel}$ is the in-plane wavevector, $\epsilon\left(\omega\right)$ is the dispersive dielectric function of the substrate and c is the speed of light. The dispersion of this mode is reiterated by the black dashed line in Fig. 3.4 a), for an unpatterned substrate the majority of the oscillator strength lies at the asymptotic frequency $951\mathrm{cm}^{-1}$ as illustrated by the blue peak.

The effect of the substrate may be understood in the context of the plasmon hybridisation model proposed by Nordlander *et al.* to explain the plasmonic resonances of complex nanostructures in terms of their more easily understood constituent particles. This theory was initially utilised to analyse the separation dependance of the modes of plasmonic nanosphere dimers [23]. As the spheres are brought together their resonances split into red-shifted, bright, bonding modes and blue-shifted, dark, anti-bonding modes with energetic separation dependant on the inter-sphere gap. This model was later extended to account for the hybridisation of the modes of a single sub-wavelength plasmonic sphere on a planar metallic substrate [95] where it was found that when the plasma frequency of the substrate tends to infinity the charging of the surface is instantaneous and the nanosphere plasmons interact with both their image and the image of other plasmons with the same azimuthal symmetry resulting in a red shift of the modes. When the plasma frequency lies just above the surface plasmon frequency the red shift dramatically increases, this is explained as a result of hybridisation with the propagative surface plasmon described in Sec. 2.1.2.

Our system is illustrated in Fig. 3.4a). The surface mode is dispersive between the transverse and longitudinal optic phonon frequencies with a strong frequency asymptote labelled ω_{SPhP}. This asymptote results in accumulation of the surface phonon density

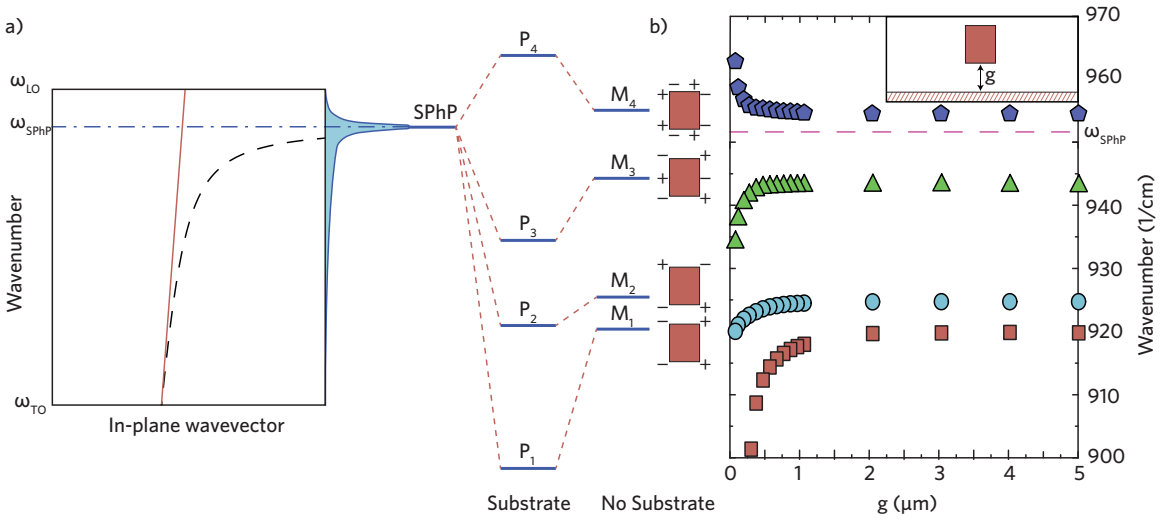


Figure 3.4: a) The graph illustrates the dispersion of the surface phonon polariton mode supported by a vacuum/ SiC interface is indicated by the black dashed, the light line by the red solid and the asymptotic surface phonon frequency at ω_{SPh} by a blue dot-dashed line. The density of states is sketched on the right of the plot, peaking at ω_{SPh}. Also illustrated are the surface charge distributions of the four lowest lying m=1 modes of the resonator in the absence of a substrate $\mathrm{M}_1 \rightarrow \mathrm{M}_4$. Hybridised modes of the resonator on substrate system are labelled $\mathrm{M}_1 \rightarrow \mathrm{M}_4$. b) An illustration of the transverse (m=1) mode shifts as a cylindrical resonator of height 800nm and diameter 1μm is lowered onto a substrate.

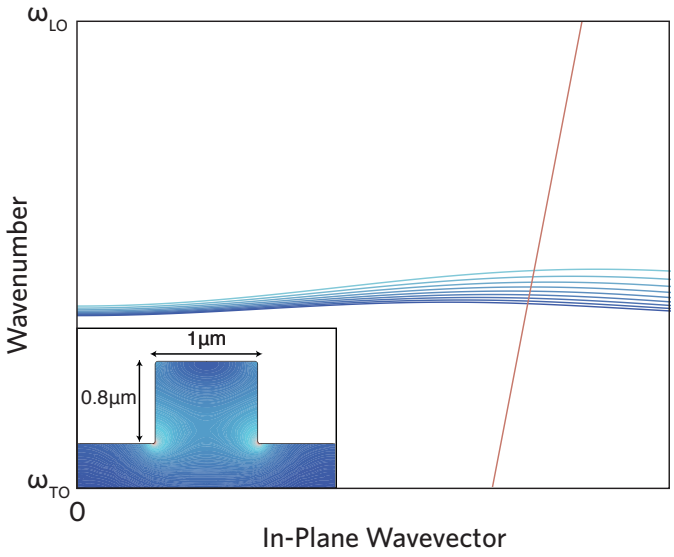


Figure 3.5: The dispersion of the longitudinal mode calculated from COMSOL simulations is indicated by the blue curves for an array of pitches from 5μm (light) to 7μm (dark). The light line is indicated by the red curve. The cylinders are of height 1μm and height 800nm. The inset illustrates a slice of the longitudinal modes electric field norm.

of states close to ω_{SPhP} as illustrated by the blue shaded curve. The sub-diffraction resonator modes considered in Sec. 3.1.3 also lie in the window $\omega_{\mathrm{TO}} \rightarrow \omega_{\mathrm{LO}}$ and are therefore spectrally local to ω_{SPhP}. The surface charge distributions of the four lowest energy resonator modes with $e^{i\phi}$ azimuthal dependance are sketched and the modes are labelled $\mathrm{M}_1 \rightarrow \mathrm{M}_4$. As the modes are spectrally local from hybridisation theory we expect them to couple strongly to the surface mode. For resonators on a substrate this will result in the hybridised modes $\mathrm{P}_1 \rightarrow \mathrm{P}_4$ in Fig. 3.4a).
To explore this behaviour, a single SiC cylinder was lowered onto a planar SiC surface and the energy shifts of the modes recorded. The results are shown in Fig. 3.4b) as a function of the resonator-substrate separation, the inset illustrate the simulation. The three modes lying below the asymptotic surface phonon frequency ω_{SPh}, which is indicated by the dashed line, are seen to red shift and the one above is seen to blue shift. This is in agreement with the theory of Nordlander [95].

3.1.4 Resonator Arrays

In order to achieve experimentally measurable observables it is necessary to measure arrays of resonators. In this study we restrict ourselves to square 2D arrays of resonators.

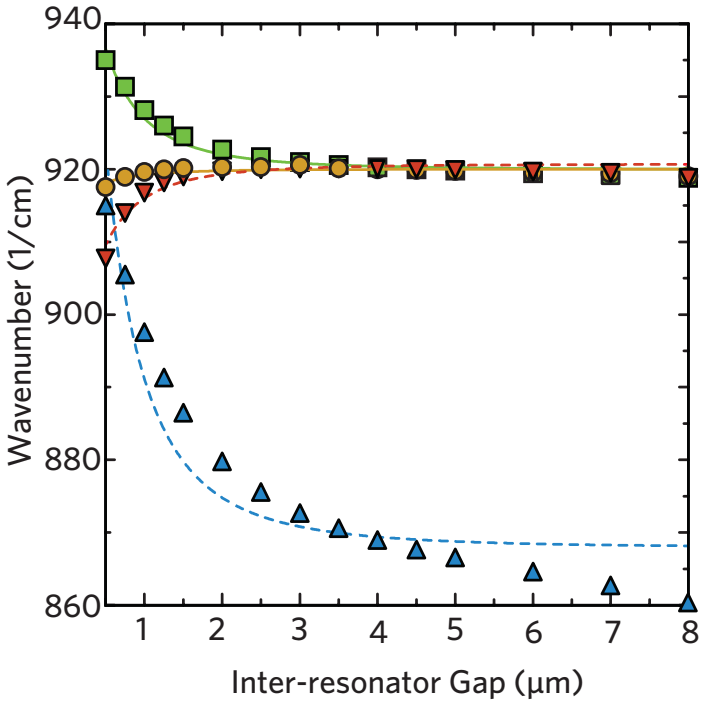


Figure 3.6: Symbols represent the real resonant frequency $\mathrm{Re}\left[\tilde{\omega}_{\mathrm{m}}\right]$ calculated from the pole fitting algorithm at the $\mathrm{k}_{\|}=0$ point for a square array of cylinders of height 800nm and diameter 1μm. Green squares (orange circles) represent the longitudinal (lowest transverse) mode in free cylinders. Blue triangles (red inverted triangles) represent the longitudinal (lowest transverse) mode for cylinders in contact with an SiC substrate. The overlapping lines represent a fit with a simple dipole-dipole coupling model.

We follow the procedure of Yariv *et al.* [96] by defining the mode of the periodic array as a linear combination of the individual resonator modes $\mathrm{E}_{\mathrm{n}}\left(\mathbf{r}\right)$ along a straight line parallel to the illumination wavevector, which is defined to lie along the principle axis of the array. The dispersion of the mode of the periodic system in the lossless case may be calculated utilising a tight-binding approximation as

$$\omega_{\mathrm{k}_{\|},\mathrm{n}}=\omega_{\mathrm{n}}\left(1-\frac{\Delta\gamma}{2}+\left(\beta_1-\gamma_1\right)\cos\left(\mathrm{k}_{\|}\mathrm{R}\right)\right), \tag{3.28}$$

where $\omega_{\mathrm{k}_{\|},\mathrm{n}}$ is the dispersive frequency, $\mathrm{k}_{\|}$ is the in-plane wavevector, ω_{n} is the frequency of the single resonator and the $\Delta\gamma$, β_1, γ_1 are as defined in [96]. An example of the dispersion of the longitudinal mode of the cylinder on substrate system is shown in Fig. 3.5

We briefly study the inter-resonator coupling in square arrays of cylinders with h=800nm and d=1000nm. We study square arrays of cylinders in vacuum and analyse

the hybridisation of the modes labelled M in the prior section. This is compared to the analogous result for hybridisation of the substrate coupled modes labelled P in the prior section. The pole-finding method discussed in Sec. 3.1.2 can be adapted for periodic systems by the application of Bloch-Floquet periodic boundary conditions on the in-plane simulation edges. The Silver-Müller radiation condition is retained on the other simulation edges, enforced by the presence of a perfectly matched layer. In these calculations the inter-resonator gap is varied and the real resonant frequencies of the fundamental longitudinal and transverse modes considered in Sec. 3.1.3 are calculated, results are illustrated by the symbols in Fig. 3.6. The lines represent fits to the results assuming simple $1/r^3$ dipole-dipole coupling. The longitudinal mode is seen to blue shift as the inter-resonator gap decreases, this is because their dipole moments are all aligned out of plane and therefore interact repulsively. The transverse modes red shift as their dipole moments are aligned in-plane and interfere attractively. Larger shifts are observed in the resonant frequencies of the on substrate P modes. This is predominantly a result of increased coupling through the substrate.

3.1.5 Coherent Coupling Between Propagative and Localised Phonon Polaritons

Now we consider more carefully the resonator arrays on a substrate. When we introduce periodic patterning to the substrate surface the simple picture presented in Sec. 3.1.3 changes. The delocalised SPhP is now a Bloch mode meaning its in-plane wavevector is no longer unique. Its dispersion folds back at the edge of the first Brillouin zone defined by $2\pi/a$ where a is the lattice period. The SPhP may now exist within the light-cone at experimentally accessible in-plane wavevectors. The folding as a function of array periodicity is illustrated in Fig. 3.7 for square arrays of the indicated period, it is obvious that by tuning the array period it is possible to tune the folded SPhP frequency. This means that the assumption made in Sec. 3.1.3, namely that the oscillator strength of the mode is concentrated at a single frequency is no longer valid. The coupling to the surface mode must be dealt with in two parts, coupling to the asymptotic branch at ω_{SPh} and coupling to the folded local branch.

We describe this system by taking as the uncoupled basis the modes of a single resonator on substrate (The modes labelled P in Sec. 3.1.3) and the local folded branches of the SPhP dispersion. This amounts to assuming that the effect of the local branches have a perturbative effect on the modes. We will limit our discussion of the cylinder modes to the three lowest lying resonator modes in our geometry. These are the lowest order

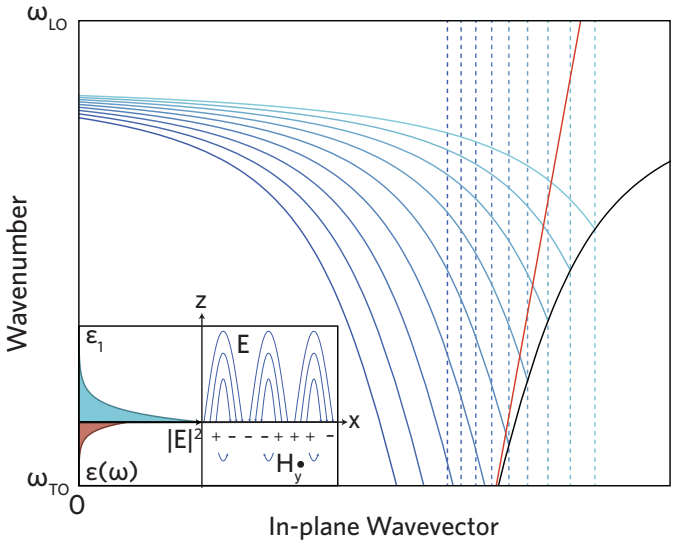


Figure 3.7: The first folded branch of the SPhP dispersion is indicated for a selection of array periods between 5 and 7μm. Vertical dashed lines indicate the edge of the first Brillouin line.

longitudinal (m=0) mode labelled l with creation (annihilation) operators $\hat{a}^{\dagger}_{k_{\parallel}}$ $\left(\hat{a}_{k_{\parallel}}\right)$ and the two lowest transverse (m=1) modes labelled t1 with creation (annihilation) operators $\hat{b}^{\dagger}_{k_{\parallel}}$ $\left(\hat{b}_{k_{\parallel}}\right)$ and t2 with creation (annihilation) operators $\hat{c}^{\dagger}_{k_{\parallel}}$ $\left(\hat{c}_{k_{\parallel}}\right)$ .When only a single folded SPhP branch lies in the neighbourhood of the resonator modes we can describe this system utilising a Hamiltonian composed of two terms. The Hamiltonian of the uncoupled modes is

$$\mathcal{H}_0 = \hbar \sum_{k_{\parallel}} \left[\omega^{l}_{k_{\parallel}} \hat{a}^{\dagger}_{k_{\parallel}} \hat{a}_{k_{\parallel}} + \omega^{t1}_{k_{\parallel}} \hat{b}^{\dagger}_{k_{\parallel}} \hat{b}_{k_{\parallel}} + \omega^{t2}_{k_{\parallel}} \hat{c}^{\dagger}_{k_{\parallel}} \hat{c}_{k_{\parallel}} + \omega^{s}_{k_{\parallel}} \hat{d}^{\dagger}_{k_{\parallel}} \hat{d}_{k_{\parallel}}\right], \tag{3.29}$$

where $k_{\parallel}$ is the in-plane wavevector, $\omega^{s}_{k_{\parallel}}$ is the angular frequency of the local SPhP branch and $\hat{d}^{\dagger}_{k_{\parallel}}$ $\left(\hat{d}_{k_{\parallel}}\right)$ are the local SPhP branch creation (annihilation) operators. The angular frequencies $\omega^{l}_{k_{\parallel}}$, $\left(\omega^{t1}_{k_{\parallel}}, \omega^{t2}_{k_{\parallel}}\right)$ are those of the lowest lying longitudinal (transverse) modes of the substrate coupled resonator. The resonator modes couple to the local surface mode through the interaction term

$$\mathcal{H}_{int} = \hbar \sum_{k_{\parallel}} \left[f_0 \left(\hat{a}^{\dagger}_{k_{\parallel}} \hat{d}_{k_{\parallel}} + \hat{d}^{\dagger}_{k_{\parallel}} \hat{a}_{k_{\parallel}}\right) + g_0 \left(\hat{b}^{\dagger}_{k_{\parallel}} \hat{d}_{k_{\parallel}} + \hat{d}^{\dagger}_{k_{\parallel}} \hat{b}_{k_{\parallel}}\right) + h_0 \left(\hat{c}^{\dagger}_{k_{\parallel}} \hat{d}_{k_{\parallel}} + \hat{d}^{\dagger}_{k_{\parallel}} \hat{c}_{k_{\parallel}}\right)\right], \tag{3.30}$$

where f_0, g_0 and h_0 are the coupling rates of the longitudinal, first transverse and second transverse modes respectively with the local SPhP branch. The rotating wave approxi-

mation has been taken, valid when the couplings fulfil $f_0, g_0, h_0 \ll \omega^{m}_{k_\parallel}, \omega^{t1}_{k_\parallel}, \omega^{t2}_{k_\parallel}, \omega^{s}_{k_\parallel}$.

If the coupling rates f_0, g_0 and h_0 exceed radiative and non-radiative loss rates from the system then it is expected that the mode energies deviate from the bare ones. This is exactly what we observed in Sec. 3.1.3 due to coupling to the asymptotic branch of the SPhP. In this situation the modes of the system are found as linear superposition of the bare modes given by

$$Y^{i}_{k_\parallel} = m^{i}_{k_\parallel} a_{k_\parallel} + n^{i}_{k_\parallel} b_{k_\parallel} + o^{i}_{k_\parallel} c_{k_\parallel} + p^{i}_{k_\parallel} d_{k_\parallel}, \tag{3.31}$$

where $m^{i}_{k_\parallel}, n^{i}_{k_\parallel}, o^{i}_{k_\parallel}\, p^{i}_{k_\parallel}$ are the Hopfield coefficients of the ith polariton mode $Y^{i}_{k_\parallel}$ which detail the modal composition [97]. By postulating this solution as an eigenmode of $\mathcal{H}$ we solve the problem

$$\left[Y^{i}_{k_\parallel}, \mathcal{H}\right] = \Omega^{i}_{k_\parallel} Y^{i}_{k_\parallel}. \tag{3.32}$$

Written in matrix form this problem is

$$\begin{pmatrix} \omega^{m}_{k_\parallel} - \Omega^{i}_{k_\parallel} & 0 & 0 & f_0 \\ 0 & \omega^{t1}_{k_\parallel} - \Omega^{i}_{k_\parallel} & 0 & g_0 \\ 0 & 0 & \omega^{t2}_{k_\parallel} - \Omega^{i}_{k_\parallel} & h_0 \\ f_0 & g_0 & h_0 & \omega^{s}_{k_\parallel} - \Omega^{i}_{k_\parallel} \end{pmatrix} \begin{pmatrix} m^{i}_{k_\parallel} \\ n^{i}_{k_\parallel} \\ o^{i}_{k_\parallel} \\ p^{i}_{k_\parallel} \end{pmatrix} = \Omega^{i}_{k_\parallel} \begin{pmatrix} m^{i}_{k_\parallel} \\ n^{i}_{k_\parallel} \\ o^{i}_{k_\parallel} \\ p^{i}_{k_\parallel} \end{pmatrix}, \tag{3.33}$$

the solutions of which are the modal frequencies $\Omega^{i}_{k_\parallel}$. The coupled modes are analogous to those previously observed in plasmonic systems and termed waveguide plasmon polaritons. Christ *et al.* provide a neat demonstration of the coupling of the plasmonic modes of gold ridges with 1D periodicity on an indium tin oxide waveguide layer. They observed a clear anticrossing between the waveguide and plasmonic modes [98].

We calculate these frequencies numerically in the usual way with results given by the symbols in Fig. 3.8 a), b) and c) for array periods 6μm, 6.5μm and 7μm respectively. The benefit of our mode solving approach is apparent compared to simply illuminating with a plane wave and measuring the reflectance. Our method allows for calculation of the complex modal frequency even in regions far away from the cylinder resonances where the coupling to light is weak. In these regions where coupling to plane waves is small, the field enhancement at the pole can still be very large. This is illustrated in

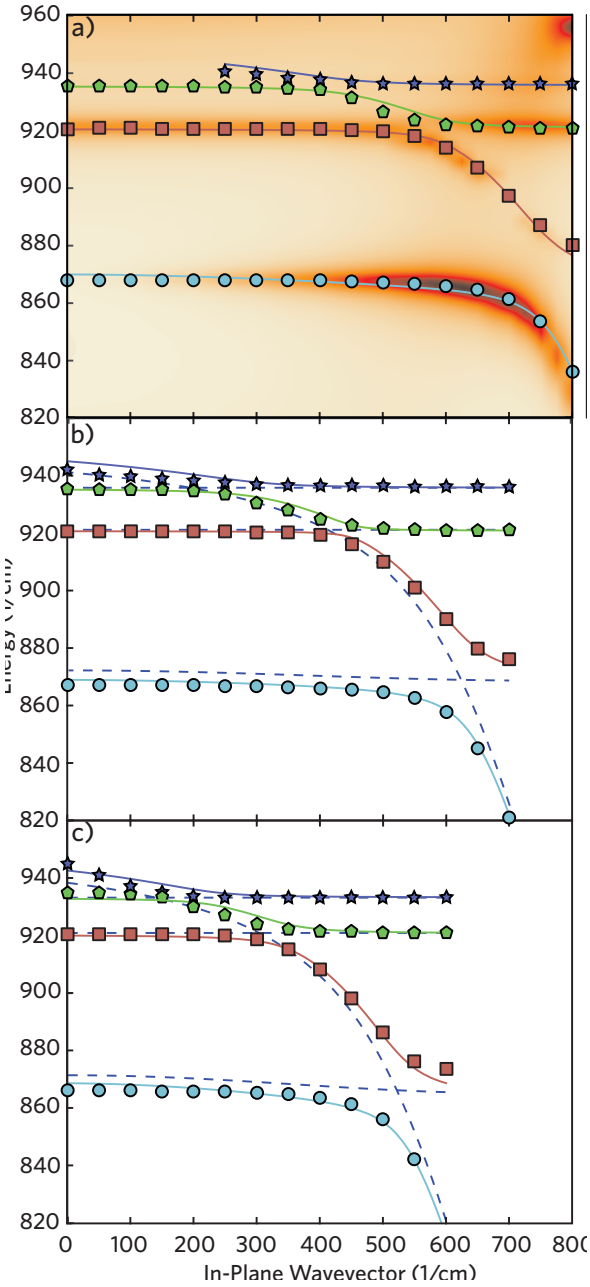


Figure 3.8: Plots of the real resonant frequency $\mathrm{Re}\,[\tilde{\omega}]$ as a function of the in-plane wavevector for array periods a) 6μm, b) 6.5μm and c) 7μm. The symbols represent numerical data and the lines fits to the energy calculated at the root of Eq. 3.33. Each plot is truncated to restrict to the first Brillouin zone. a) Is overlain on a numerical reflectance map calculated using COMSOL multiphysics. The dashed lines in b), c) represent the constituent modes.

Fig. 3.8a) which is overlain on a numerical plane-wave reflectance map, in regions where the polaritons are predominantly SPhP in nature the reflectance dip disappears. A clear anti-crossing is observed in each data set resulting from coupling of the resonator modes to the folded branch of the surface mode. Each plot has been truncated before the edge of the first Brillouin zone to maintain the validity of the approximation of a single folded branch. A wider portion of the dispersion can be treated at the expense of greater analytical complexity. For larger in plane wavevector more branches of the SPhP must be considered. Fits calculated by the roots of Eq. 3.33 are given by the lines. Excellent agreement is seen between numerics and theory. The peak Rabi frequency is 15.84cm^{-1}, this represents ≈2% of the bare mode energy. Fitting deviations can be attributed to the lossless approximation of the longitudinal mode dispersion calculated by Eq. 3.28 and the dispersionless approximation of transverse modes which were taken to reduce the quantity of fitting variables. The calculated frequencies for the higher polariton are systematically depressed from the fit, this is due to coupling of the surface mode to higher energy, close-spaced resonances which have been omitted for simplicity.

By further manipulation of Eq. 3.33 it is possible to calculate the Hopfield coefficients $m^i_{k_\parallel}$, $n^i_{k_\parallel}$, $o^i_{k_\parallel}$ $p^i_{k_\parallel}$ whose squares weight ea unsch of the polaritonic components in Eq. 3.31 . These are shown in Fig. 3.9 for array period 6μm. The lowest lying polariton shown in Fig. 3.9 a) transforms from being completely longitudinal in character near $k_\parallel$=0 to an anticrossing with the surface mode at $k_\parallel$=750cm^{-1}. The second polariton illustrated in Fig. 3.9 b) is composed of the lowest lying transverse mode near $k_\parallel$=0, anticrossing with the surface mode near $k_\parallel$=600cm^{-1} and then with the longitudinal mode at $k_\parallel$=750cm^{-1}. The third polariton illustrated in Fig. 3.9 c) is mainly composed of the second transverse mode at $k_\parallel$=0, anticrossing with the surface mode around $k_\parallel$=400cm^{-1} and with the lowest transverse mode at 600cm^{-1}. Finally the fourth polariton illustrated in Fig. 3.9 d) is mainly composed of the surface mode near $k_\parallel$=0, anticrossing with the second transverse mode near $k_\parallel$=250cm^{-1}. Note that in all regions where the polariton is composed predominantly of the delocalised surface wave it acquires finite character in all the resonator modes as a result of surface mediated mixing.

The linewidths of the coupled mode are expected to vary predictably as linear superpositions of the bare linewidths according to the Hopfield coefficients [99]. This will give a dispersion in the linewidths of each mode as a function of the in-plane wavevector as a result of the change of mixing ratios of the modes. The linewidth of

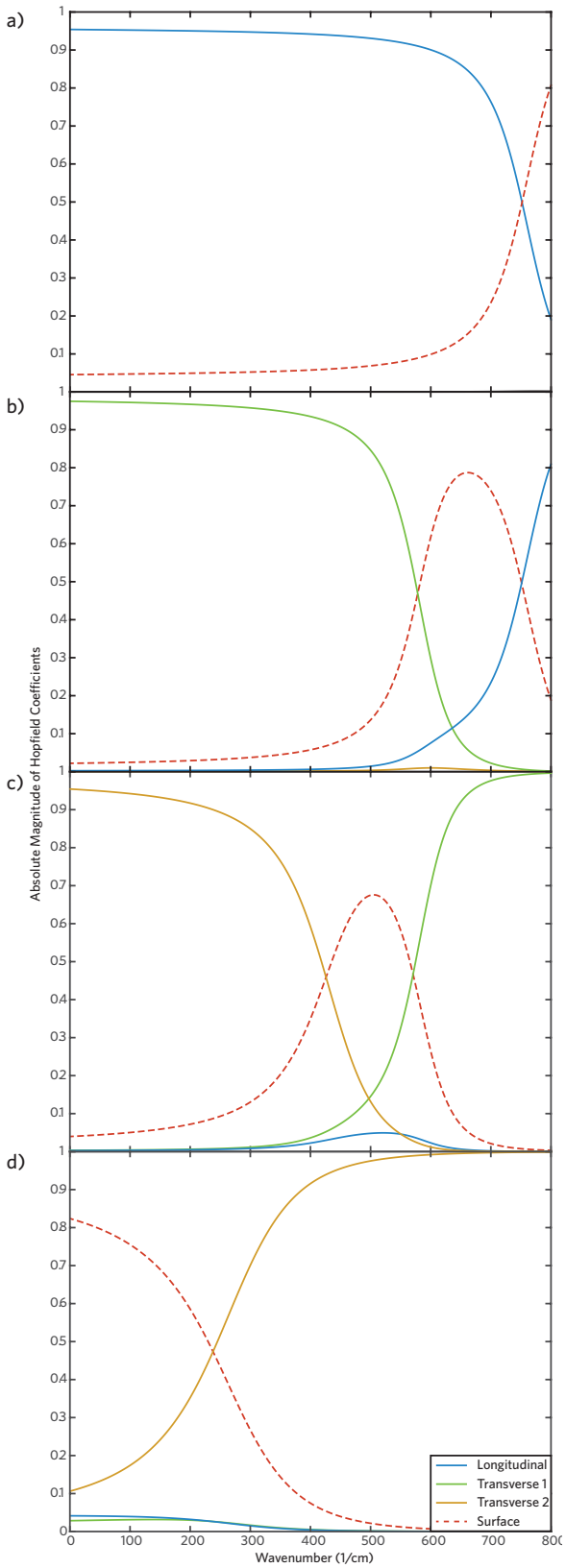


Figure 3.9: Plots of the absolute magnitude of the Hopfield coefficients for array period 6μm. The plots a)-d) show each polariton individually in order of ascending energy at $k_{\|}$=0.

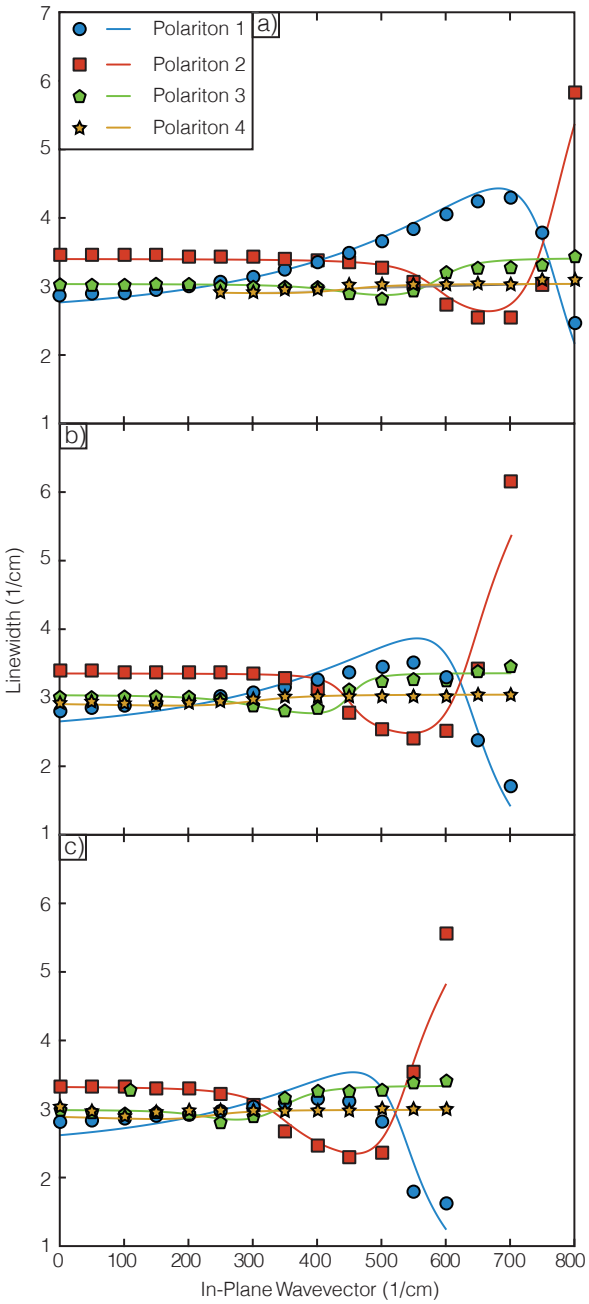


Figure 3.10: Polariton linewidths for array periods a) 6μm, b) 6.5μm and c) 7μm. Symbols indicate numerical values. Lines indicate theoretical fits calculated utilising Eq. 3.40. Each plot is truncated to restrict to the first Brillouin zone.

the ith polariton mode may be written

$$\Gamma^{i}_{k_\parallel} = \left|m^{i}_{k_\parallel}\right|^2 \Gamma^{m}_{k_\parallel} + \left|n^{i}_{k_\parallel}\right|^2 \Gamma^{t1}_{k_\parallel} + \left|o^{i}_{k_\parallel}\right|^2 \Gamma^{t2}_{k_\parallel} + \left|p^{i}_{k_\parallel}\right|^2 \Gamma^{s}_{k_\parallel} \tag{3.34}$$

where $\Gamma^{m}_{k_\parallel}, \Gamma^{t1}_{k_\parallel}, \Gamma^{t2}_{k_\parallel}, \Gamma^{s}_{k_\parallel}$ are the linewidths of the uncoupled longitudinal, transverse, second transverse and surface mode respectively. The numerical linewidths of the coupled modes are calculated from the complex modal frequency. Numerical results for array periods 6μm, 6.5μm and 7μm are given by the symbols in Fig. 3.10. We fit to this with Eq. 3.40. The linewidth of the surface mode $\Gamma^{s}_{k_\parallel}$ is dispersive and is calculated analytically from our choice of dielectric function. The monopole linewidth $\Gamma^{m}_{k_\parallel}$ is also dispersive. We fit it by a phenomenological $a+bk^2_\parallel$ relationship, which is verified by fitting to the already dispersive monopolar linewidth in the absence of the substrate. The transverse mode linewidths $\Gamma^{t1}_{k_\parallel}, \Gamma^{t2}_{k_\parallel}$ are modelled as dispersionless. The results of the fit are given by the lines in Fig. 3.10. Excellent agreement between theory and numerics is once again observed. We can understand the dispersive behaviour of the linewidths by comparison with the Hopfield coefficients calculated earlier and plotted for the 6μm array in Fig. 3.9. For the 6μm data in Fig. 3.10 a) the first polariton follows the monopole linewidth dispersion out to $k_\parallel \approx 700\text{cm}^{-1}$ where it falls toward the surface mode linewidth. This is where the modal character of the polariton changes as evidenced by the Hopfield coefficients plotted in Fig. 3.9 a). The other linewidth data is interpreted similarly. These calculations of linewidths provide dual verification of the frequency calculations presented in Fig. 3.8, verifying the validity of our model.

3.2 Measurements of the Coherent Coupling

In order to observe the coherent coupling we verified numerically in the previous section Alberto Politi and Francesco Martini fabricated 70×70 square arrays of 3C-SiC cylindrical resonators on a polished 9.7μm thick layer of <100> orientated SiC grown on Si by inductively coupled plasma reactive ion etching. This depth of SiC substrate was found to be sufficient to achieve convergence in reflectance measurements. The cylinders were of diameter 1μm and height 800nm and the period of the array was varied from 5−7μm. An example image of the fabricated array is shown in Fig. 3.11.

Optical data was measured utilising a Bruker Hyperion Fourier transform infrared (FTIR) microscope in reflectance mode. A grazing angle objective was utilised to allow observation at large in-plane wavevector. This objective works by rotating the light cone onto the sample by use of the angled mirror illustrated in Fig. 3.12 a). This breaks

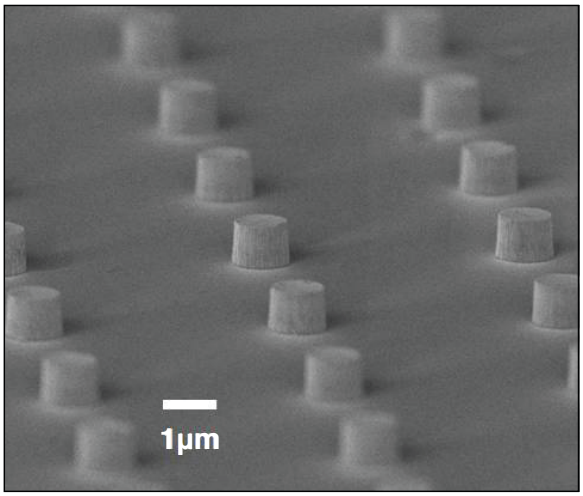


Figure 3.11: A scanning electron microscope image of a fabricated SiC pillar array

the illuminations cylindrical symmetry, resulting in a highly directional illumination which can be orientated along the principle axis of the square nanopillar array. The angle-resolved illumination peaks at two distinct angles due to the action of the mirror allowing for collection of light at two fixed in-plane wavevectors. An example of the sampled data for the 6.25μm pitch sample is shown in Fig. 3.12 b). Rather than scanning the illumination angle to map out the dispersion as in the previous section we instead tune the surface mode frequency by altering the array period as shown in Fig. 3.7.

The experimental reflectance map is shown as a function of the array period in Fig. 3.13. The longitudinal mode of the resonator is seen to exhibit a clear anticrossing with the folded surface mode branch. No anticrossing is observed with the transverse resonator mode at 915cm^{-1}. This is attributed to the experimental broadening, although our illumination is directed along the array principle axis it maintains a finite azimuthal aperture. In addition, the illumination will have a finite angular spread. Both will result in a smearing of the observed modes. There could also be additional intrinsic loss in our system as a result of defects in the SiC. This allows us to simplify the model described in Sec. 3.1.5 onto two coupled modes described by the Hamiltonian

$$\mathcal{H}=\sum_{k_\parallel}\left[\hbar\omega^{m}_{k_\parallel}\hat{a}^{\dagger}_{k_\parallel}\hat{a}_{k_\parallel}+\hbar\omega^{s}_{k_\parallel}\hat{b}^{\dagger}_{k_\parallel}\hat{b}_{k_\parallel}+\hbar f_0\left(\hat{a}^{\dagger}_{k_\parallel}\hat{b}_{k_\parallel}+\hat{a}_{k_\parallel}\hat{b}^{\dagger}_{k_\parallel}\right)\right], \tag{3.35}$$

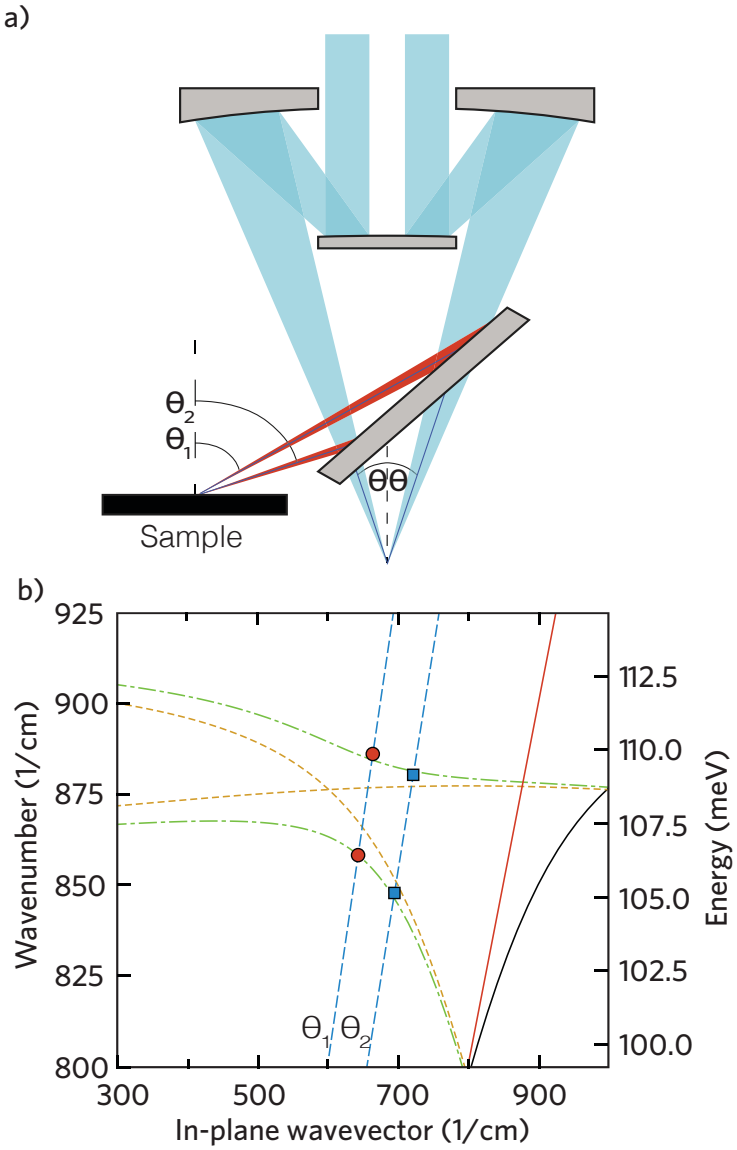


Figure 3.12: b) An illustration of the grazing incidence objective utilised in the experiment. The angled mirror rotates the light cone of the Schwarschild objective onto the sample providing a highly directional, dual peaked illumination. b) An illustration of the measurement points for array period 6.25μm assuming the surface-transverse mode couplings are zero and the surface-longitudinal mode coupling f_0=13.1/cm. The polariton dispersions are indicated by the green dot-dashed line. The bare mode dispersions are indicated by the gold dashed lines. The illumination light lines are indicated by the blue dashed lines. The circles and squares indicate the peak positions sampled by the measurement.

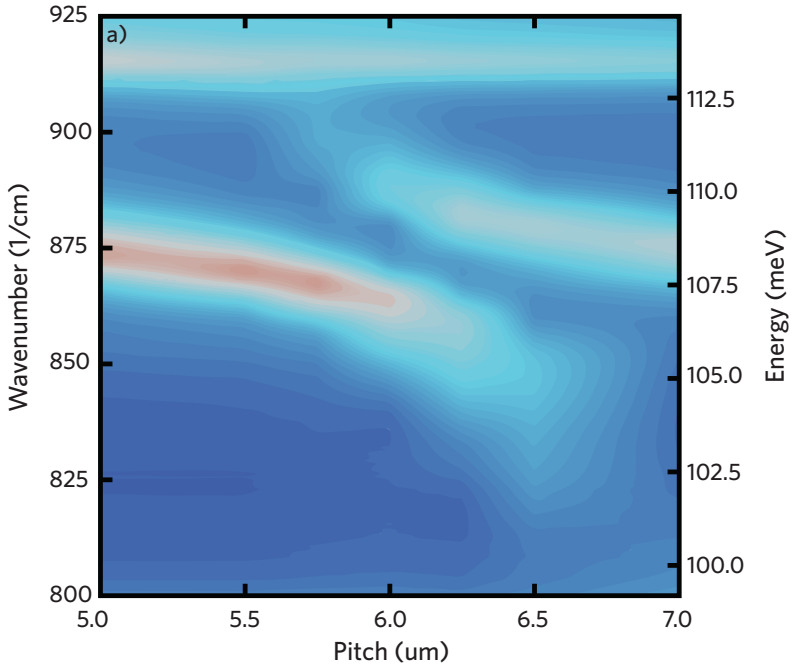


Figure 3.13: Experimental reflectance map as a function of the array period. A clear anticrossing is visible around 6μm.

where $\hat{a}_{k_\parallel}$ and $\hat{b}_{k_\parallel}$ are the bosonic creation operators for the longitudinal cylinder mode and surface mode respectively and f_0 is a phenomenological coupling parameter. The rotating wave approximation has been made. This Hamiltonian may be put in diagonal form by diagonalising the corresponding Hopfield-Bogoliubov matrix for each value of the in-plane wavevector $k_\parallel$

$$H_{k_\parallel} = \begin{bmatrix} \omega^{l}_{k_\parallel} & f_0 \\ f_0 & \omega^{s}_{k_\parallel} \end{bmatrix}, \tag{3.36}$$

diagonalised by use of the polaritonic operators

$$\hat{p}^{+}_{k_\parallel} = X_{k_\parallel}\hat{a}_{k_\parallel} + Y_{k_\parallel}\hat{b}_{k_\parallel}, \tag{3.37}$$

$$\hat{p}^{-}_{k_\parallel} = Y_{k_\parallel}\hat{a}_{k_\parallel} - X_{k_\parallel}\hat{b}_{k_\parallel}, \tag{3.38}$$

where $X_{k_\parallel}$ and $Y_{k_\parallel}$ are the Hopfield coefficients [97] as described before and the eigenfrequency is given by

$$\Omega^{\pm}_{k_\parallel} = \frac{\omega^{m}_{k_\parallel} + \omega^{s}_{k_\parallel} \pm \sqrt{\left(\omega^{m}_{k_\parallel} - \omega^{s}_{k_\parallel}\right)^2 + 4f_0^2}}{2}, \tag{3.39}$$

where ± refers to upper and lower branches of polaritons. To fit to the reflectance map in Fig. 3.13 we carry out least square fits for the tight binding parameters $\alpha_1=(\beta_1-\gamma_1)$, $\Delta\gamma, \omega_{\mathrm{m}}$ described in Sec. 3.1.4 and the two incident angles θ_1, θ_2 illustrated in Fig. 3.12. The coupling strength is assumed to have a superradiant dependance on the resonator density, we fit for the parameter ζ linked to the coupling strength as $g_0=\zeta\sqrt{\rho}$ [100]. The results of this fit are shown in Fig. 3.14 a).Agreement is seen with the experimental data, the anticrossing being clearly reproduced. We attribute discrepancies in the fit to changes due to strain induced by the lattice parameter mismatch between the SiC layer and the Si substrate [101]. The situation can be greatly improved by allowing free variation of the parameters $\epsilon_0, \epsilon_\infty$ and ω_{T} from the book values [37]. This fit is shown in Fig. 3.14 b), requiring variations in the static and high frequency dielectric constants of less than 5%. The peak Rabi frequency is calculated for the 5μm period sample as $\mathrm{f_0}$=20.57cm^{-1} or around 2.5% of the bare mode energy. This places the system far below the ultrastrong coupling (USC) regime and justifies the use of the rotating wave approximation (RWA) in our analysis [102]. The fitting procedure yielded $\theta_1=(48.54\pm0.05)^\circ$, $\theta_2=(55.08\pm0.08)^\circ$, $\epsilon_0=9.26\pm0.22$, $\epsilon_\infty=6.68\pm0.17$ and $\omega_{\mathrm{T}}=97.85\pm0.07$meV (789.3±0.6/cm).

In addition, we extract the normal mode linewidths from the reflectance map Fig. 3.13. To model them we assume as in Sec. 3.1.5 they are linear combinations of the constituent mode linewidths weighted by the Hopfield coefficients [99]

$$\Gamma^{+}_{\mathrm{k}_\parallel}=\Gamma^{\mathrm{l}}|\mathrm{X}_{\mathrm{k}_\parallel}|^2+\Gamma^{\mathrm{s}}_{\mathrm{k}_\parallel}\ |\mathrm{Y}_{\mathrm{k}_\parallel}|^2, \tag{3.40}$$

$$\Gamma^{-}_{\mathrm{k}_\parallel}=\Gamma^{\mathrm{l}}|\mathrm{Y}_{\mathrm{k}_\parallel}|^2+\gamma^{\mathrm{s}}_{\mathrm{k}_\parallel}\ |\mathrm{X}_{\mathrm{k}_\parallel}|^2, \tag{3.41}$$

where Γ^{l} is the linewidth of the longitudinal mode, which we assume to be constant over the measured region, and $\Gamma^{\mathrm{s}}_{\mathrm{k}_\parallel}$ is the dispersive linewidth of the surface mode which can be described analytically.

As the SPhP is itself a result of the strong coupling of photons to the crystals transverse phonon resonance we can describe it within the same Hopfield-Bogoliubov framework we use for the system eigenmodes as a linear superposition of free photons and optical phonon components with Hopfield coefficients $C_{k_\parallel}$ and $D_{k_\parallel}$ respectively. As a result of the steep dispersion of the free photon the composition of the SPhP is strongly wavevector dependant, becoming less photonic as the SPhP dispersion in Fig. 2.3 b) moves away from the lightline. Its linewidth therefore obeys

$$\gamma^{\mathrm{s}}_{\mathrm{k}_\parallel}=\Gamma^{\mathrm{ph}}\left|\mathrm{C}_{\mathrm{k}_\parallel}\right|^2+\Gamma^{\mathrm{TO}}\left|\mathrm{D}_{\mathrm{k}_\parallel}\right|^2, \tag{3.42}$$

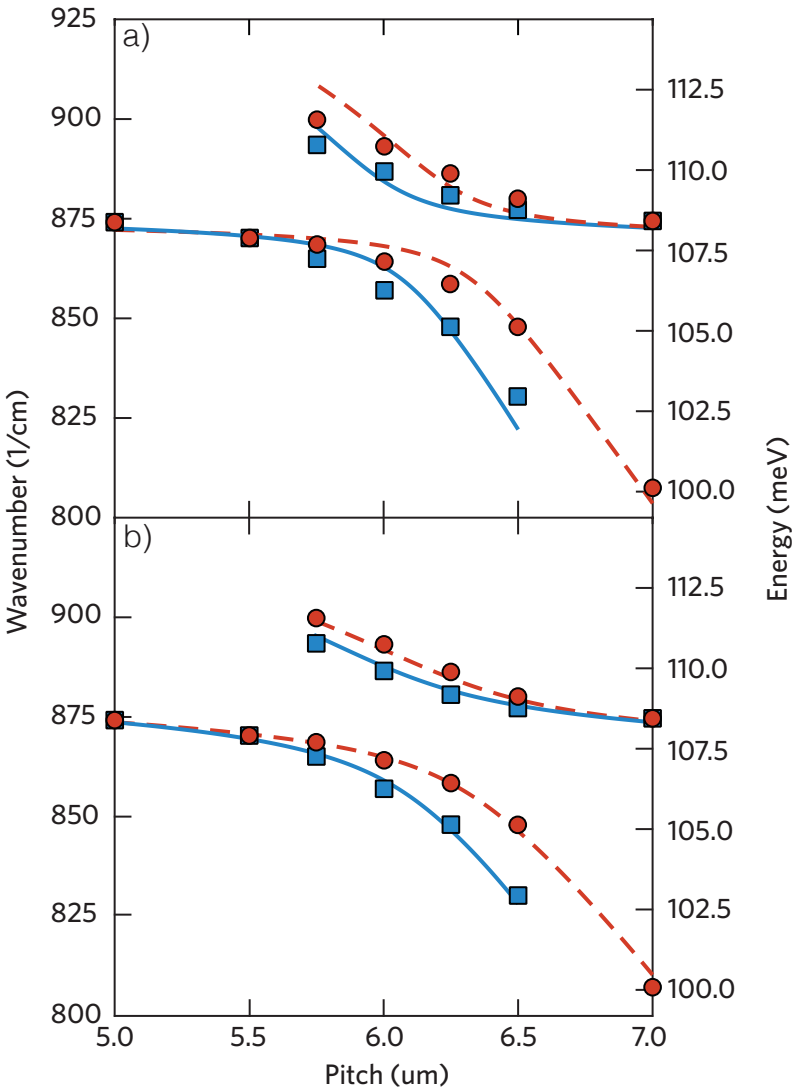


Figure 3.14: a) Experimental reflectance minima for the small (squares) and large (circles) angle beams. The corresponding lines indicate fits to the data utilising the book values of the SiC optical constants. b) As (a). This time the SiC optical constants are determined by the fitting procedure.

where Γ^{ph} and Γ^{TO} are the dispersionless loss rates of the SPhP photonic and phononic components. This equation is analogous to Eq. 3.40. We assume the intrinsic photonic loss, which mainly results from the impact of surface roughness being small when compared to the intrinsic phonon damping and approximate $\Gamma^{\mathrm{ph}} \approx 0$.
In addition to this we also have the instrumental broadening previously discussed as a result of the finite angular aperture of our objective and its finite azimuthal spread. To first order we approximate this as being proportional to the slope of the modal dispersion and therefore

$$\Gamma^{\mathrm{ds}}_{\mathrm{k}_\parallel} = \frac{\partial \omega^{\pm}_{\mathrm{k}_\parallel}}{\partial \theta} \Delta\theta = \frac{\partial \omega^{\pm}_{\mathrm{k}_\parallel}}{\partial \mathrm{k}_\parallel} \frac{\partial \mathrm{k}_\parallel}{\partial \theta} \Delta\theta = \omega^{\pm}_{\mathrm{k}_\parallel} \frac{\mathrm{v}^{\pm}_{\mathrm{k}_\parallel}}{\mathrm{c}} \cos\theta \Delta\theta, \tag{3.43}$$

where θ is the peak illumination angle along $\mathrm{k}_\parallel$, , ${\mathrm{v}_{\mathrm{k}_\parallel}}^{\pm}$ is the polariton group velocity and $\Delta\theta$ is the angular aperture. The experimental data and fit are given together in Fig. 3.15. The lower polariton modes broaden dramatically at larger pitches where the dispersion is stronger as a result of the instrument broadening discussed. A least squares fitting procedure yields $\Gamma^{\mathrm{TO}} = 4.1\mathrm{cm}^{-1}, \gamma^{\mathrm{m}} = 10.6\mathrm{cm}^{-1}$ and $\Delta\theta = 0.1\mathrm{rad}$, the predominant effect is the instrument broadening. We calculate a Q-factor for the longitudinal resonator mode of 81 with this falling in the centre of the range measured for similar samples previously [2]. The fit calculated is poor as book value of the TO phonon damping is given by $\Gamma^{\mathrm{TO}} = 6\mathrm{cm}^{-1}$ [37]. Instrument broadening then precludes us from making a thorough analysis of the experimental linewidths as for the numerical data in Sec. 3.1.5.

3.3 Conclusions

We have numerically investigated the morphological dependance of the resonances of cylindrical subwavelength SiC resonators. By changing the geometrical parameters of the cylinder it was shown that both longitudinal and transverse modes are tuneable across the Reststrahlen band. It was also shown that smaller resonators tend to support modes with a higher quality factor with a maximum calculated quality factor approaching 160. This is four times the theoretical limit for plasmonics and corresponds to an absolute lifetime around two orders of magnitude greater than the plasmonic case. In addition ultrahigh spontaneous emission enhancements approaching 10^6 were calculated for dipoles located near the field antinodes.
The interaction of localised SPhP resonances with a planar substrate supporting delocalised SPhPs was also investigated. For isolated resonators it was found that the

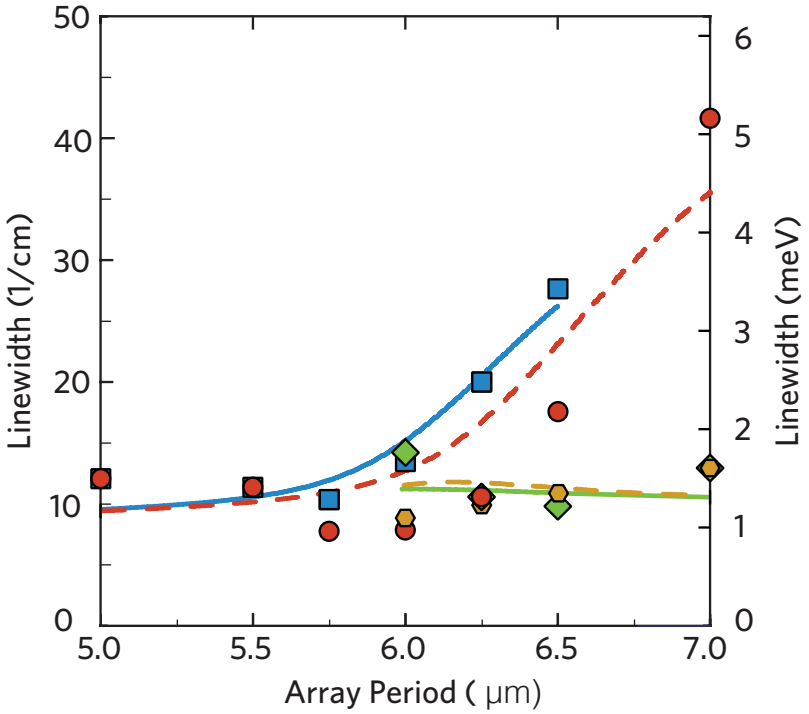


Figure 3.15: Experimental linewidths of the lower (upper) normal mode for the smaller angle data are given by red circles (yellow hexagons), and the respective fits are the red (yellow) dashed line. Blue squares (green diamonds) and blue (green) solid lines are instead used for the larger angle lower (upper) polariton data.

predominant effect of placing the resonator on a substrate is to hybridise the resonator modes by coupling to the delocalised modes of the substrate. Square periodic arrays of cylindrical resonators were also investigated and coherent coupling was observed between the folded Bloch modes of the surface and the localised resonances of the cylinders. The observed resonant frequencies and linewidths were seen to fit well to a Hopfield model where the system eigenmodes are linear superpositions of the constituents.

The deep-subwavelength modes exhibited in these systems confine the electric field strongly near to the surface of the SiC presenting obvious applications in surface enhanced infrared absorption spectroscopy of functionalised molecules and similar providing a low-loss plasmonic analogue in the mid-infrared. More interestingly the strong confinement of light in mixed light-matter modes can allow for enhancement of non-linear three-body photon scattering processes such as generation of harmonic signal by annihilation of two sub-harmonic photons. These processes depend on the square of the field amplitude [103]. This enhancement of second harmonic generation was recently observed in arrays of 4H-SiC nanopillars [104], in these experiments strong harmonic radiation intensities were seen to spectrally overlap with the resonator modes, confirming that the second harmonic is driven by the field confinement in the structures. While three body scattering events are novel and interesting in the context of mid-infrared nonlinear optics they require destruction of polaritonic modes in order to conserve energy as the width of the Reststrahlen band is always less than its energy. Four body scattering events on the other hand would allow interaction of the polaritonic modes while conserving total polariton number. This would permit thermalisation of the polaritons and in conjunction with our demonstration of a dispersion relation tuneable by patterning could allow for design of a phonon-polariton parametric oscillator as already demonstrated in the microcavity polariton systems to be discussed extensively in the following chapter [105].

In microcavity polariton systems more generally non-linear four body interactions between polaritons mediated by the polariton matter component (exciton-exciton scattering) drive exotic physical processes such as Bose-Einstein condensation [5]. Microcavity polariton systems are however limited in two senses. Firstly the polariton matter component is problematic. In inorganic systems delocalised Wannier-Mott excitons are utilised, these interact but also dissociate at ambient temperatures. In organic systems the Frenkel excitons are localised on single molecules, this allows for strong binding and room temperature operation but weak exciton-exciton interactions. The microcavity system is also diffraction limited meaning the large field intensities

required to drive these transitions are only achievable by extremely strong optical pumping. The sub-diffraction nature of phonon-polariton modes in these resonator arrays could allow for this threshold to be lowered by orders of magnitude. In the final chapter we will discuss a scheme by which the polaritonic eigenmodes of arbitrary light-matter systems may be derived. This will provide an excellent framework for evaluating the non-linear scattering rates between the polaritonic modes and assessing the suitability of these systems for non-linear polaritonics.

This work could also be extended by optimisation. The investigation of resonators on substrate presented was somewhat limited in scope as a result of the computational load required to map out the dispersion relations in Fig. 3.8 meaning that the resonator geometry investigated on the substrate was not optimised. Despite this we still achieve a peak Rabi splitting corresponding to around 2% of the bare resonance energy but by careful resonator design it would be possible to increase the coupling between localised and delocalised modes. One possible way to achieve this would be by Green's function methods which allow for explicit calculation of the surface mode scattering cross section of a single resonator located near a planar interface which supports them [106]. This would allow for estimation of the coupling for a given resonator from a single simulation and in this way it might be possible to tune resonator geometry to achieve ultrastrong coupling in these systems as discussed in Chapter 4 [107].

Chapter 4

Electrical Pumping of Microcavity Polaritons

In Chapter 3 strong coupling between the localised modes of cylindrical SiC resonators and the delocalised modes of a planar SiC interface was demonstrated. This coherent coupling can also occur in other systems under the condition that the Rabi frequency Ω describing the coupling rate is faster than all rates of loss from the system. Under this condition, energy is reversibly exchanged between the constituent modes and the coupling is coherent. The system most commonly utilised to study this behaviour is the planar optical microcavity holding some material with a resonant transition in its interstitial region, such systems are discussed in Sec. 4.1. In these systems the coherent excitations are termed microcavity polaritons. By filling the microcavity with a material possessing a large oscillator strength it is possible to leave the regime of validity for the Hamiltonian utilised in Chapter 2 requiring consideration of additional terms, this is termed the ultrastrong coupling regime and is discussed in Sec. 4.2. The remainder of this chapter discusses our experimental observations of electroluminescence (EL) from planar optical microcavities operating in the ultrastrong coupling regime and their implications for our understanding of the process of microcavity polariton formation by electrical pumping.

4.1 Microcavity Polaritons

One diffraction limited scheme to achieve strong coupling is by confinement of light within a planar optical microcavity. Cavity termination may be achieved either by use of a distributed Bragg reflector (DBR) or metallic mirrors. A DBR allows for achievement of a higher quality factor at the expense of a larger mode volume, however

such reflectors are difficult to design as the stopband must be broad enough to reflect both coupled modes [4]. Metallic mirrors constrict the mode over the active region resulting in an increase in Rabi splitting $\hbar\Omega$ [108], provide very broad stopbands allowing simultaneous confinement of both polaritons and also provide means for electrical injection [109].

The fundamental TE polarised Fabry-Perot mode energy of a planar optical microcavity as illustrated in Fig. 4.1 a) is found by consideration of the electromagnetic boundary conditions as

$$\mathrm{E_{cav}}\left(\theta\right)=\frac{\mathrm{E_{cav}}\left(0\right)}{\sqrt{1-\frac{\sin^2\theta}{\mathrm{n_b^2}}}}, \tag{4.1}$$

where $\mathrm{E_{cav}}\left(0\right)$ is the mode energy at normal incidence, θ the angle of incidence and $\mathrm{n_b}$ the refractive index of the interstitial region. The dispersive nature of the microcavity mode renders microcavity polaritons experimentally practical, by merely rotating the pump an entire polariton dispersion can be measured. For dielectric terminated cavities the TM mode dispersion is the same as the TE. Small metallic mirrored cavities however display a polarisation splitting [110] ascribed to the hybridisation of two plasmonic modes localised at the cavity walls (metal-insulator-metal (MIM) plasmon) [111]. This was described analytically by Kena-Cohen *et al.* [112] and results in an effective index for TM polarised light of

$$\mathrm{n_{eff}}=\frac{\mathrm{n_b}\left(2\mathrm{d_p}+\mathrm{L}\right)}{\sqrt{\mathrm{L}^2-\left(2\mathrm{d_p}\right)^2}}, \tag{4.2}$$

where $\mathrm{d_p}=\mathrm{c}/\omega_\mathrm{p}$ is the plasmon penetration depth and L the cavity length. This results in a higher effective index for TM polarisation and allows two full polariton dispersions to be measured from a single microcavity. An example polariton dispersion calculated using Eq. 3.39 with $\omega_{\mathrm{k}_\parallel}=\mathrm{E_{cav}}\left(\theta\right)/\hbar$ is shown in Fig. 4.1 b). The polariton modes exhibit a clear anticrossing at the point where the constituent dispersions cross.

The matter mode may be chosen dependant on application. Early experiments involved the Wannier-Mott excitons of inorganic semiconductor quantum wells [4]. These are delocalised, bound electron-hole pairs with a Bohr radius of $10-100$Å (extending therefore over many lattice sites) and a binding energy of $10-100$meV. These systems were the first to make use of angle-resolved measurements to map the polariton dispersion curve [113] and since experiments on such systems have exhibited many interesting phenomena such as stimulated scattering [114], polariton lasing [115] and quantum fluidic behaviours [6, 116] at cryogenic temperatures. The low binding energy of Wannier-Mott excitons is however limiting when it comes to making practical devices as at room temperature the exciton lifetime is often short and increasing

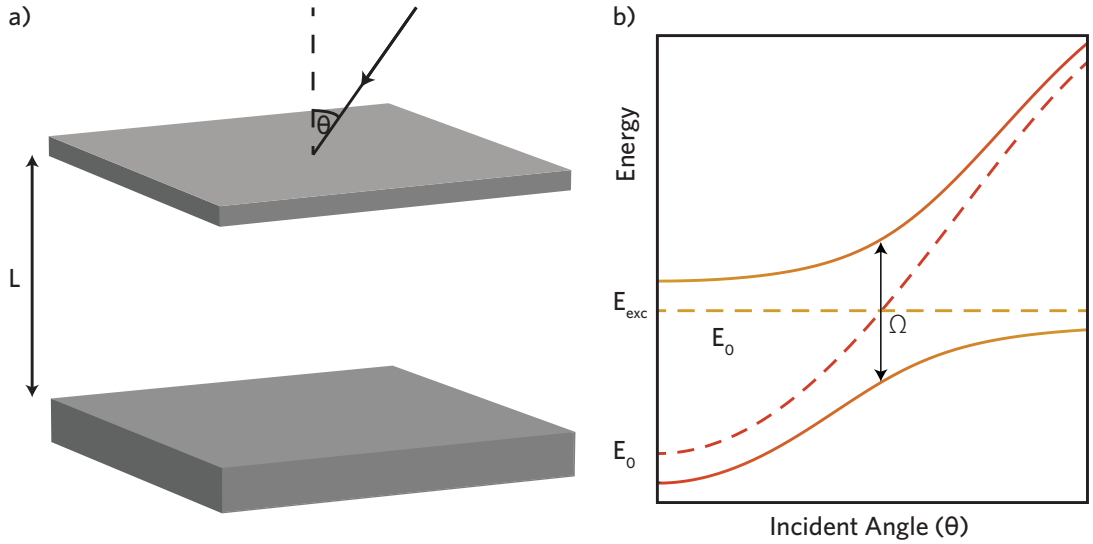


Figure 4.1: (a) An illustration of a planar optical microcavity of length L. Light is incident at angle θ from the normal. (b) Illustration of the dispersion of the microcavity mode as a function of incident angle (red dashed line) as governed by Eq. 4.1. The yellow dashed line illustrates an electronic resonance of the cavity fill. The solid lines indicate the resulting coupled mode dispersions with composition indicated by the line colour.

the coupling strength by increasing pump fluence only works up until the Mott limit [117]. One way of circumventing this is by use of intersubband (ISB) polaritons in semiconductor quantum wells where the upper density of bosonic operation is controllable by doping [118]. Intersubband polaritons were first observed in the mid-infrared [119] and since ISB polariton light emitting device have been demonstrated [120]. The increased exciton densities achievable in these systems also allow for probing of the ultrastrong coupling regime [102], to be discussed in Section. 4.2.

A third option is to utilise the Frenkel polaritons of organic semiconductors. These are localised on individual molecules of the semiconductor and as a result of reduced screening compared to inorganics exhibit binding energies from $0.1-1$eV rendering them stable at room temperature. Frenkel excitons possess a far larger oscillator strength than Wannier-Mott excitons meaning they will couple to the cavity mode more effectively, larger Rabi splittings are therefore achievable. Frenkel linewidths are broadened by the presence of a progression of discrete vibronic levels which themselves are inhomogeneously broadened. The exciton linewidth is often of the order of 1eV rendering strong coupling difficult to achieve. For this reason initial works focussed upon organic molecules with especially narrow linewidths such as porphyrins [121]

or cyanine dyes [122]. More recently the advantages of using materials with broad linewidths has been reported, these materials can offer huge increases in oscillator strength and therefore in achievable Rabi splitting [112]. They have allowed stable room temperature demonstrations of lasing [123] and Bose-Einstein condensation [5, 124].

4.2 Ultrastrong Coupling

The use of organic molecules with giant oscillator strengths and ISB excitons in strongly doped systems has opened up a new arena of optical interactions termed the ultrastrong coupling regime. This is characterised by Rabi splittings of the same magnitude as the bare mode energies. Now the analysis in Section. 3.1.5 becomes invalid and it is necessary to consider the full Hamiltonian. This results in the addition of two extra terms to the Hamiltonian. An anti-resonant term

$$\mathcal{H}_{\text{anti}}=\hbar\sum_{\mathrm{k}_\parallel} \mathrm{g}_0\left(\mathrm{a}_{\mathrm{k}_\parallel}\mathrm{b}_{-\mathrm{k}_\parallel}+\mathrm{a}^\dagger_{\mathrm{k}_\parallel}\mathrm{b}^\dagger_{-\mathrm{k}_\parallel}\right), \tag{4.3}$$

which arises from not taking the rotating wave approximation. Secondly we require a term corresponding to the square of the magnetic vector potential

$$\mathcal{H}_{\mathrm{A}^2}=\hbar\sum_{\mathrm{k}_\parallel} \mathrm{D}_{\mathrm{k}_\parallel}\left(\mathrm{a}^\dagger_{\mathrm{k}_\parallel}\mathrm{a}_{\mathrm{k}_\parallel}+\mathrm{a}_{\mathrm{k}_\parallel}\mathrm{a}^\dagger_{\mathrm{k}_\parallel}+\mathrm{a}_{\mathrm{k}_\parallel}\mathrm{a}_{-\mathrm{k}_\parallel}+\mathrm{a}^\dagger_{\mathrm{k}_\parallel}\mathrm{a}^\dagger_{-\mathrm{k}_\parallel}\right), \tag{4.4}$$

where $\mathrm{D}(\mathrm{q})=\mathrm{g}_0^2/4\omega_{\text{exc}}$ quantifies the magnetic vector potential contribution [125, 126]. This is the full Hamiltonian as diagonalised by Hopfield in his seminal paper [97]. The Hamiltonian is now 4×4 due to the anti-resonant coupling between states of opposite wavevector. The problem now therefore requires introduction of polaritonic operators of form

$$\mathrm{p}_{\mathrm{k}_\parallel}=\mathrm{w}\mathrm{a}_{\mathrm{k}_\parallel}+\mathrm{x}\mathrm{b}_{\mathrm{k}_\parallel}+\mathrm{y}\mathrm{a}^\dagger_{-\mathrm{k}_\parallel}+\mathrm{z}\mathrm{b}^\dagger_{-\mathrm{k}_\parallel}, \tag{4.5}$$

where the Hopfield coefficients are given by $\mathrm{w},\mathrm{x},\mathrm{y},\mathrm{z}$. The eigenvalue problem is therefore

$$\begin{pmatrix} \omega_{\mathrm{k}_\parallel}+2\mathrm{D}_{\mathrm{k}_\parallel} & -i\Omega_{\mathrm{k}_\parallel}/2 & -2\mathrm{D}_{\mathrm{k}_\parallel} & -i\Omega_{\mathrm{k}_\parallel}/2 \\ i\Omega_{\mathrm{k}_\parallel}/2 & \omega_{\text{exc}} & -i\Omega_{\mathrm{k}_\parallel}/2 & 0 \\ 2\mathrm{D}_{\mathrm{k}_\parallel} & -i\Omega_{\mathrm{k}_\parallel}/2 & -\omega_{\mathrm{k}_\parallel}-2\mathrm{D}_{\mathrm{k}_\parallel} & -i\Omega_{\mathrm{k}_\parallel}/2 \\ -i\Omega_{\mathrm{k}_\parallel}/2 & 0 & i\Omega_{\mathrm{k}_\parallel}/2 & -\omega_{\text{exc}} \end{pmatrix} \begin{pmatrix} \mathrm{w} \\ \mathrm{x} \\ \mathrm{y} \\ \mathrm{z} \end{pmatrix} = \omega \begin{pmatrix} \mathrm{w} \\ \mathrm{x} \\ \mathrm{y} \\ \mathrm{z} \end{pmatrix}, \tag{4.6}$$

the roots of which give the coupled mode frequencies $\omega^{+}_{\mathrm{k}_{\|}}, \omega^{-}_{\mathrm{k}_{\|}}$.
As the Rabi splitting $\Omega_{k_{\|}}$ increases so do the anomalous Hopfield coefficients y, z also affecting the ordinary Hopfield coefficients x, w. The ground state of the system is a vacuum of polaritons defined $\mathrm{p}_{\mathrm{k}_{\|}} |\mathrm{G}\rangle = 0$ meaning it contains finite numbers of photon and excitons [126]. These are virtual and do not normally contribute to the extra-cavity fields. It has been proposed to collect this virtual radiation by modulation of the Rabi splitting through time-modulated bias of an intersubband polariton quantum well [127]. Ultrastrong coupling using ISB polaritons has been demonstrated in the infrared [102, 128, 129] and THz [130]. Recently the use of organic semiconductors has allowed for comparable Rabi splittings to be achieved in the visible. Huge Rabi splittings of 1eV were achieved using a thin film of the molecule 2,7-bis[9,9-di(4-methylphenyl)-fluoren-2-yl]-9,9-di(4-methylphenyl)fluorene (TDAF) [112, 131]. Cyanine dies have also been used to demonstrate Rabi splittings of 700meV [132].

4.3 Excitation and Relaxation of Microcavity Polaritons

The most common experimental scheme to excite microcavity polaritons is optical pumping as this allows for simplistic cavity architectures. The only design consideration in such systems is placing the active region at the cavity mode antinode. In an inorganic cavity under optical pumping the picture of polariton formation is simple: collective excitons form by absorption of photons into a narrow electronic resonance and the strong intermolecular interaction which hybridise with the cavity field forming polaritons. The wave vector is a good quantum number for these hybrid states. In organic materials the electronic resonance is broad and the intermolecular interaction is small. When excitons are formed by optical pumping they are therefore localised, non-collective excitations. Polaritons form as follows, a coherent polarisation is formed in the medium by the cavity mode. If the coupling is strong enough, the cavity and exciton modes hybridise giving coherent polaritonic states that propagate with group velocity defined by the polariton dispersion as opposed to the random hopping of localised, incoherent excitons. Polaritons in organic microcavities can only form for certain values of the wavevector, for example it has been shown that for large wavevectors coherent states cannot form due to strong dephasing destroying the coherent polarisation [133]. The result is that the number of coherent, polariton states is far less than the number of localised, incoherent exciton states. Non-resonant optical pumping then excites predominantly incoherent states which radiatively decay and pump the coherent polariton states, the

lower polariton states may be excited by emission of one or two optical phonons from the incohorent states [134, 135]. Emission from the upper polariton branch is generally weak due to the possibility of fast, non-radiative decay to the bath of incoherent states [136].
A preferable alternative to excite microcavity polaritons is electrical pumping. Direct electrical excitation was first demonstrated in 2005 by embedding an active layer of the J aggregate TDBC in an RC organic light emitting diode (OLED) structure with silver electrodes exhibiting strong coupling with a Rabi splitting of 265meV [109]. Indirect electrical excitation has also been attempted by electrical pumping of an adjacent weakly-coupled layer with the additional benefit of achieving equality between upper and lower branch emission by eliminating the requirement for an incoherent exciton reservoir [137]. One key issue with polariton electroluminescence is the achievable device efficiency. Efficiencies comparable to commercial OLEDs will be necessary to make practical, room temperature equivalents of recently demonstrated polariton lasers [138]. Recently the efficiency of a strongly coupled OLED was compared to that of the corresponding weakly coupled architecture and was found to be around 6 times smaller due to weak scattering toward the bottom of the lower polariton branch [139]. Secondly, the process of polariton formation by electrical injection is not well understood and development of a picture analogous to that for nonresonant optical pumping is necessary for a good understanding of the system. These problems are the subject of the work in the next section.

4.4 Polariton Electroluminescence from an Ultrastrongly Coupled Organic Light-Emitting Diode

The light matter interaction quantified by the Rabi energy is proportional to the emitter density and oscillator strength and inversely proportional to the mode volume [112, 133]. Often works focus on materials with narrow linewidth and high peak absorbance such as J-aggregates [122] or porphyrins [121]. To maximise the coupling strength in our system, a molecule with an extremely broad optical transition and therefore a large oscillator strength was utilised. Fabricated microcavities consist of an active layer of the oligomer 2,7-bis[9,9-di(4-methylphenyl)-fluoren-2-yl]-9,9-di(4-methylphenyl)fluorene (TDAF), which has previously been used to achieve ultrastrong coupling with Rabi splittings of 1eV [112] and to demonstrate organic polariton condensation [5]. TDAF is ambipolar, allowing for electron and hole transport [140]. Its exciton resonance is located at E_{ex}=3.5eV. Metallic mirrors were employed to constrict the cavity mode

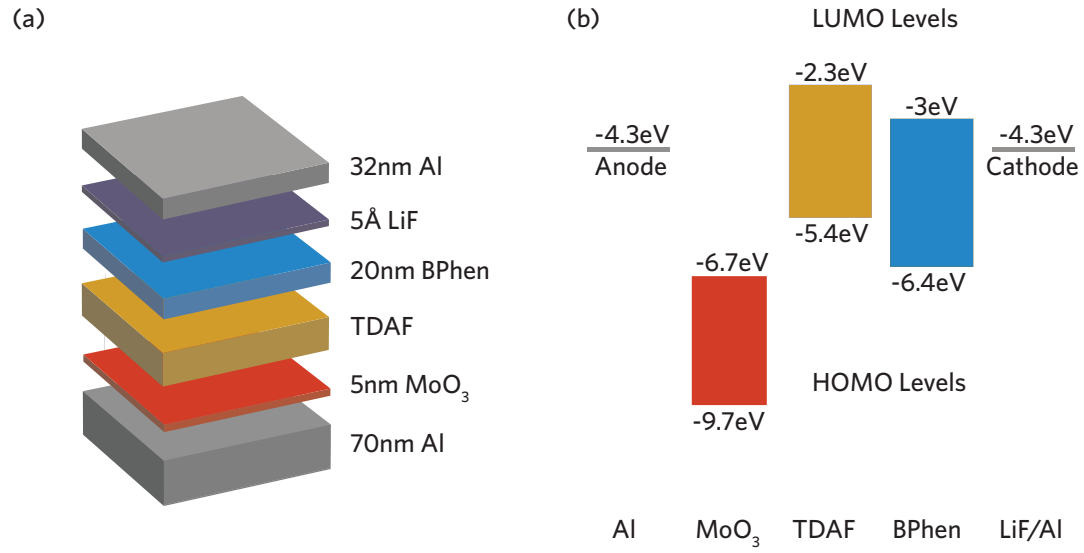


Figure 4.2: a) The physical structure of the device b) Electrode work functions and lowest unoccupied/ highest occupied molecular orbitals (LUMO/HOMO) of the interstitial materials.

volume and allow for electrical injection.

Direct electrical injection onto the TDAF active layer would be highly inefficient. To ease the transport of holes onto the active layer, a 5nm MoO_3 hole injection layer was employed which permits hole-transport through defect states [141]. A 20nm hole blocking layer of 4,7-diphenyl-1,10-phenanthroline (BPhen) was utilised to prevent holes migrating to the cathode. Electrical injection proceeded through a 0.5nm LiF layer and the leaky 32nm Al cathode. The Al anode was 70nm thick. The device structure is illustrated in Fig. 4.2 a). The electronic structure of the device is shown in Fig. 4.2 b), excitons are expected to form at the TDAF/BPhen interface due to an accumulation of holes as a result of the deep highest occupied molecular orbital (HOMO) of BPhen. Devices were fabricated by thermal evaporation at 10^{-7}millibar on cleaned fused silica substrates. The width of the TDAF active layer was varied from 55-65nm in 5nm steps to allow for detuning of the cavity mode relative to the exciton energy.

To confirm the operation of the devices in the ultrastrong coupling regime, angle-resolved electroluminescence measurements were carried out at 3.75V. Both transverse electric and transverse magnetic polarisations were measured due to the expected polarisation splitting discussed in Section. 4.1. Resulting electroluminescence contour plots normalised to the peak intensity at normal incidence for each device are shown

in Fig. 4.3. Lower polariton emission is strong and peaked at normal incidence. The lower polariton energy is seen to increase with energy as expected from the model of Section. 4.1.

There is no observed electroluminescence from the upper polariton branch due to the huge Rabi splitting and its corresponding high energy. To find the position of the upper polariton angle-resolved reflectivity measurements were carried out on the samples. Reflectivity minima corresponding to the upper and lower polaritons are indicated by the black squares in Fig. 4.3.

The ultrastrong coupling Hamiltonian of Section. 4.2 may be adapted to this system by adoption of a constant Rabi frequency. The resulting eigenvalue equation is given by

$$\begin{pmatrix} \mathrm{E_{ph}}(\theta)+2\mathrm{D} & -i\hbar\Omega/2 & -2\mathrm{D} & -i\hbar\Omega/2 \\ i\hbar\Omega/2 & \mathrm{E_{exc}} & -i\hbar\Omega/2 & 0 \\ 2\mathrm{D} & -i\hbar\Omega/2 & -\mathrm{E_{ph}}(\theta)-2\mathrm{D} & -i\hbar\Omega/2 \\ -i\hbar\Omega/2 & 0 & i\hbar\Omega/2 & -\mathrm{E_{exc}} \end{pmatrix} \begin{pmatrix} \mathrm{w} \\ \mathrm{x} \\ \mathrm{y} \\ \mathrm{z} \end{pmatrix} = \mathrm{E} \begin{pmatrix} \mathrm{w} \\ \mathrm{x} \\ \mathrm{y} \\ \mathrm{z} \end{pmatrix} \tag{4.7}$$

where $\mathrm{E_{ph}}(\theta)$ is the angle dependant energy of the cavity mode. Fitting to this system yields the results of Table. 4.1. It is seen that the Rabi splitting is reduced compared to that achievable for a cavity solely filled with TDAF [112], this is due to the presence of the injection and blocking layers giving a reduction in active molecular density in the microcavity. The plasmon-mediated polarisation splitting discussed in Section. 4.1 is apparent in the larger effective index of the TM-polarised microcavity polaritons. These exhibit reduced Rabi splittings due to decreased overlap of the cavity mode with the active layer. Ultrastrong coupling effects onset when the normalised coupling strength $\Omega/\mathrm{E_{exc}}$ exceeds 20% [102]. TE-polarised light in our devices exhibits normalised couplings $\Omega/\mathrm{E_{exc}}=0.21-0.23$ and TM polarised light $\Omega/\mathrm{E_{exc}}=0.17-0.19$ which are both around a sixth of the largest value reported thusfar [142].

Now that the devices are confirmed to be operating in the ultrastrong coupling regime, their electrical performance bears analysis. The total emitted optical power as a function of forward bias was recorded utilising a large-area calibrated photodiode. Results are shown in Fig. 4.4. A constant optical turn on voltage is observed at 3.1V for all the devices despite the differing lower polariton energies illustrated in Fig. 4.3. The exciton energy of TDAF lies above the turn-on voltage at 3.5eV. These results indicate that polaritons are not formed directly by electrical injection which is to be expected as polaritons are also not formed directly by optical pumping [133]. It also contradicts previous reports which suggest that ultrastrong coupling facilitates a

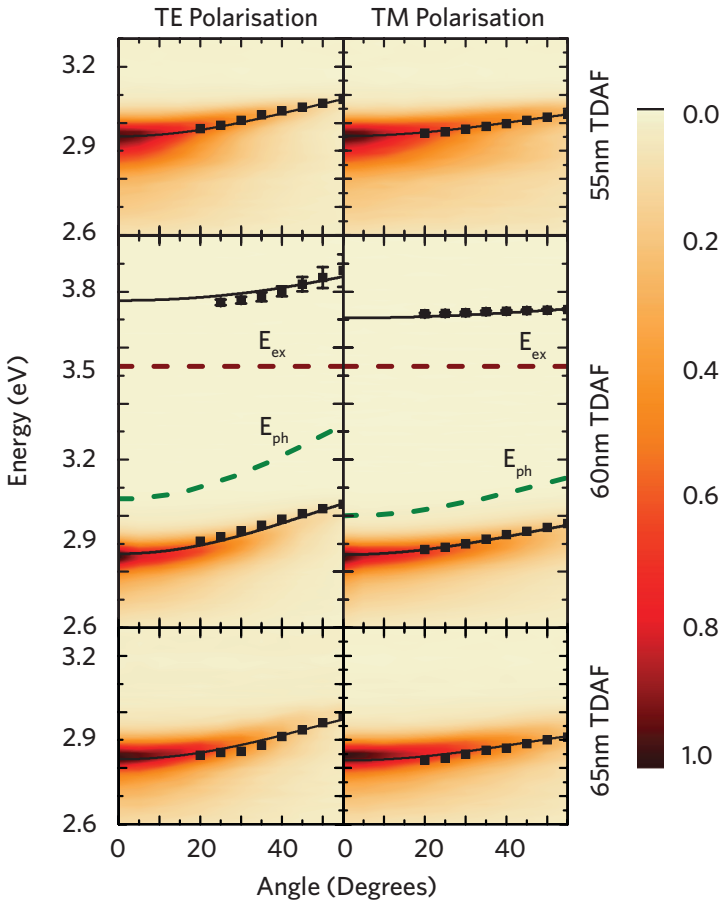


Figure 4.3: a) Angle-resolved EL measured at 3.75 V. TE polarization is shown on the left, while TM polarization is on the right. The corresponding TDAF thicknesses are indicated on the right hand side. The black squares correspond to reflectivity minima, while the solid lines were obtained from a fit of reflectivity and EL to Eq. 4.7. The entire spectral range is only shown for the 60 nm-thick film, where dashed lines also show the bare photon and exciton dispersions

Table 4.1: Results from fitting a Hopfield model to the electroluminescence from our OLED samples. The exciton energy E_{exc} was fixed at 3.5eV. The Rabi frequency Ω, cavity effective index n_{eff} and normal incidence cavity mode energy $E_{cav}(0)$ are given.

Thickness	Ω (meV)	n_{eff}	$E_{cav}(0)$(eV)
55nm (TE)	770 ± 30	2.40 ± 0.30	3.17 ± 0.033
60nm (TE)	790 ± 20	2.10 ± 0.10	3.06 ± 0.019
65nm (TE)	750 ± 30	2.42 ± 0.07	3.00 ± 0.014
55nm (TM)	655 ± 3	$3,25 \pm 0.05$	3.11 ± 0.003
60nm (TM)	670 ± 5	2.82 ± 0.07	3.00 ± 0.006
65nm (TM)	610 ± 30	3.20 ± 0.10	2.94 ± 0.012

change in the system work function [143].

These results allow us to draw a picture of polariton formation by electroluminescence in organic systems analogous to that sketched out in Section. 4.3 for photoluminescence. Initially, electrons and holes combine on a TDAF molecule to form an incoherent (localised) exciton. The energy required to do so corresponds to a vibrationally relaxed exciton out in the optical absorption tail. As TDAF has an extremely broad optical resonance, this lies far below the main exciton peak at around 3.1eV. This is not however the state which couples strongly to the cavity mode. That state is the direct transition from ground, which possesses the largest oscillator strength and corresponds to a vibrationally excited nuclear configuration of the singlet state. These states interactions with light yield the hybrid polariton modes observed above. The localised, relaxed excitons excited by electrical pumping can scatter into the coherent (delocalised) modes due to the large Rabi splitting, which moves the hybrid state to energies similar to or below those of the relaxed exciton. The scattering can either proceed radiatively [144] or by phonon emission [134, 145]. The latter is favoured in systems with large Stokes shifts. These processes are illustrated by Fig. 4.5.

Finally, we calculate the external quantum efficiency (EQE) of the device by measurement of the ratio of emitted photons to injected electrons. The results are illustrated in Fig. 4.6 and the values take into account the efficiency of polariton formation and their subsequent radiative decay to free space. To carry out the calculation the angle-resolved EL was parameterised and the known dispersion used to account for radiation emitted without the detectors θ=75° light cone. Reflections from the measurement apparatus were accounted for by use of the appropriate Fresnel coefficients. An EQE of 0.1% is obtained for all devices, representing a 5 order of magnitude improvement over the only previously reported case of ultrastrong coupled electroluminescence [146]. This is still an order of magnitude below that for weakly coupled TDAF devices however

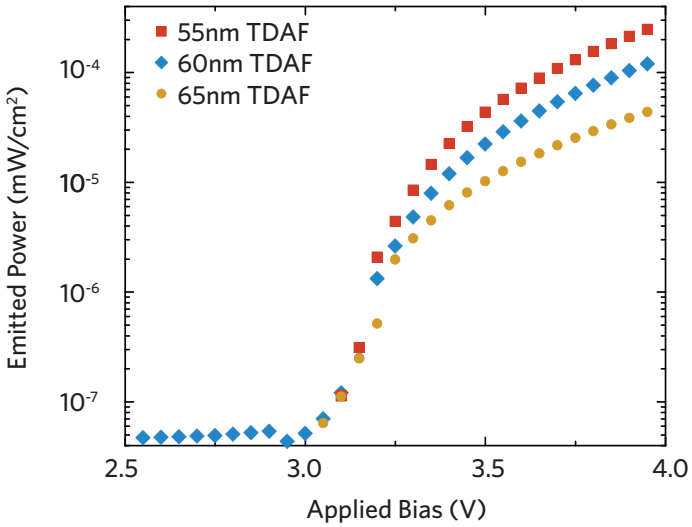


Figure 4.4: Emitted optical power, scaled by device area, as a function of increasing forward bias. Note the identical turn-on voltage of 3.1 V for all devices

[140]. This is due to the additional non-radiative loss channels introduced by the metal microcavity, such as the excitation of Al/air and short-range surface plasmons, the sub-optimal placement of the heterojunction for coupling to LPs, and inefficient leakage of polaritons to free space.

4.5 Conclusions

In this Chapter we have demonstrated electroluminescence from a metal terminated microcavity OLED containing an active layer of the oligomer 2,7-bis[9,9-di(4-methylphenyl)-fluoren-2-yl]-9,9-di(4-methylphenyl)fluorene (TDAF). We made measurements of the angle-resolved electroluminescence to record the dispersion of the device emission and found that the coupling between the bare microcavity mode and the Frenkel exciton mode of the TDAF oligomers was coherent. Moreover the Rabi frequency exceeded 20% of the bare frequencies clearly placing our devices in the ultrastrong coupling regime where the rotating wave approximation fails. In addition by analysis of the total emitted optical power from our devices we were able to form a clear picture of the process of microcavity polariton formation by electrical injection. Similar results were recently confirmed elsewhere [147]. The improved understanding of polariton formation afforded by our experimental data will aid future studies of

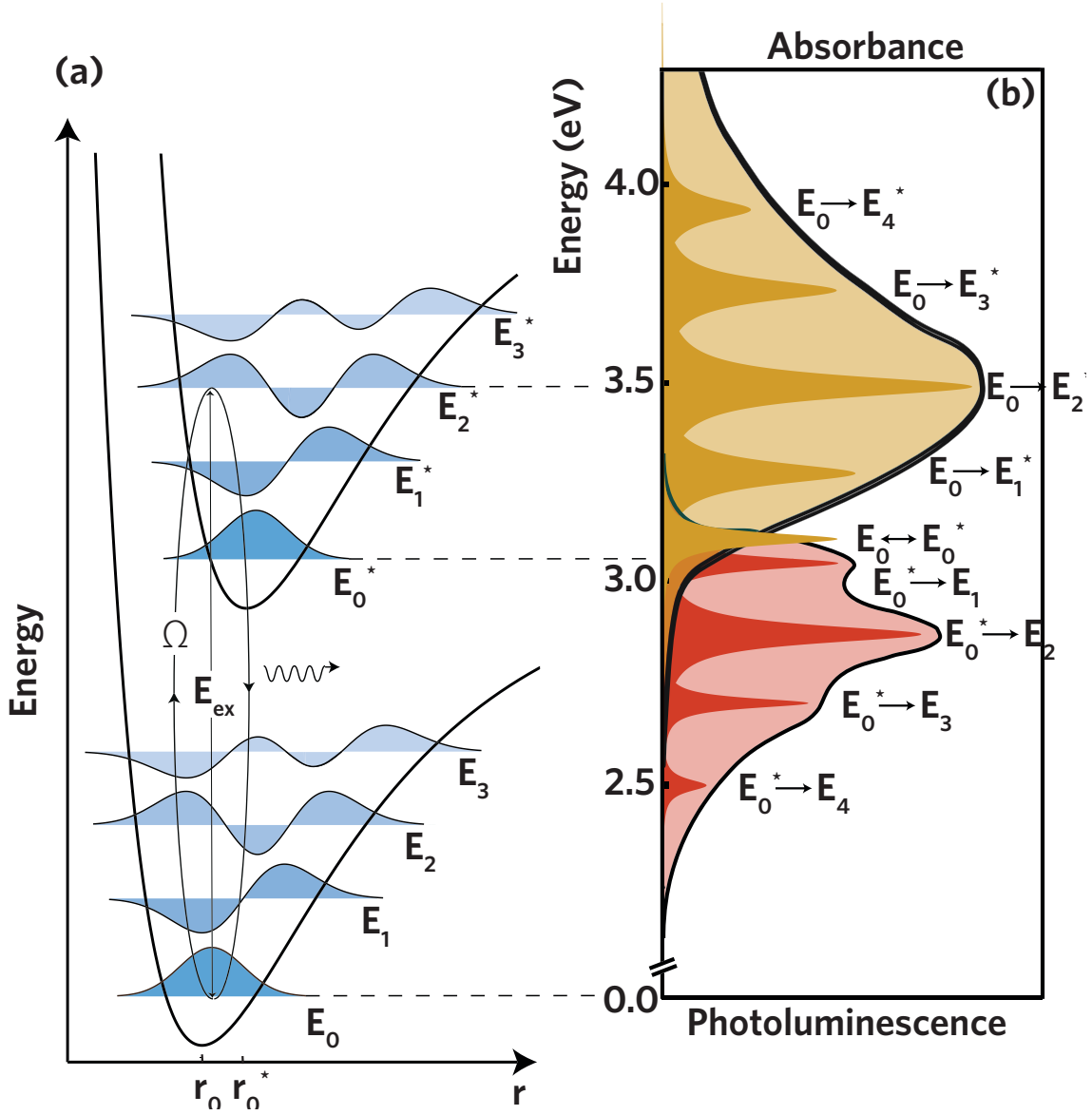


Figure 4.5: (a) Ground and excited-state electronic manifolds as function of the nuclear coordinate. The strongest optical transition is the direct transition possessing the largest wavefunction overlap (labeled Eex). Its dipole moment is strongly coupled to the cavity photon field. The resulting polaritons correspond to a reversible exchange of energy between this excited state and the cavity field at the Rabi frequency. This definition of bare exciton energy corresponds to the broad absorption maximum identified in (b). (b) Absorption and photoluminescence (PL) of TDAF. Note that the turn on voltage corresponds approximately to the relaxed exciton energy, which is in good agreement with the onset of optical absorption. The PL exhibits a Stokes shift, which allows for direct radiative pumping of the polaritons within its spectral range

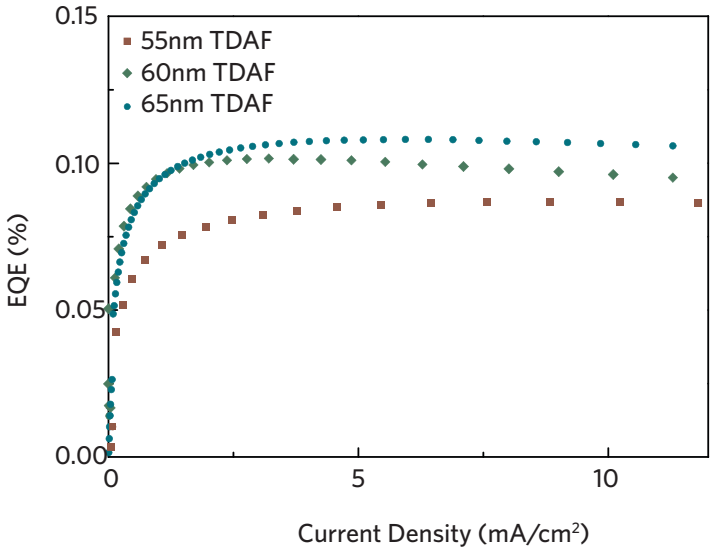


Figure 4.6: External quantum efficiency for all detunings, this is adjusted to account for emission outside the detector collection angle. Thinner devices exhibit smaller EQE despite emitting larger intensities of light as they permit more current.

novel physics in these systems such as the ground state electroluminescence recently predicted [148] or in the creation of practical devices such as polariton lasers [138].

Chapter 5

Free Space Hopfield Diagonalisation of Inhomogeneous Light Matter Systems

Development of a quantum theory of surface phonon polaritons is an important goal. It would allow for analysis of quantum effects such as quantum correlations, single-photon excitation or single SPhP interference. In addition it would allow for modelling of stimulated emission and could be utilised to describe laser operation. Quantisation of surface modes is usually treated with a macroscopic approach, describing the matter with a phenomenological dielectric function [149]. *Ad hoc* microscopic quantisation procedures where the matter is treated explicitly have also been attempted but with limitations [150]. This chapter will develop a microscopic model of field quantisation in arbitrary inhomogeneous dielectric environments. In Sec. 5.1 we will discuss the problem of field quantisation in spectral regions far from any material resonances. In Sec. 5.2 the problem of field quantisation in dispersive environments in the absence of loss will be discussed. The application to the surface phonon polariton will be discussed in Sec. 5.3. Finally we extend our model to encompass dissipation in Sec. 5.4.

5.1 Quantisation in the Absence of Dispersion

In a system without free charges, the Maxwell divergence equations stipulate that the magnetic field $\mathbf{H}$ and displacement field $\mathbf{D}$ obey

$$\nabla\cdot\mathbf{D}\left(\mathbf{r},\mathrm{t}\right)=0, \tag{5.1}$$
$$\nabla\cdot\mathbf{H}\left(\mathbf{r},\mathrm{t}\right)=0, \tag{5.2}$$

or alternatively that the fields are transverse. Then the Maxwell curl equations in the absence of sources

$$\dot{\mathbf{H}}\left(\mathbf{r},\mathrm{t}\right)=-\mathrm{c}^{2}\nabla\times\mathbf{D}\left(\mathbf{r},\mathrm{t}\right), \tag{5.3}$$
$$\dot{\mathbf{D}}\left(\mathbf{r},\mathrm{t}\right)=\nabla\times\mathbf{H}\left(\mathbf{r},\mathrm{t}\right), \tag{5.4}$$

allow the transversality of the fields to be satisfied at all times if enforced as an initial constraint. Treating the curl equations as the dynamical equations of the fields we can find the Hamiltonian $\mathcal{H}$ which satisfies the Heisenberg equations of motion

$$i\hbar\dot{\mathbf{H}}\left(\mathbf{r},\mathrm{t}\right)=\left[\mathbf{H}\left(\mathbf{r},\mathrm{t}\right),\mathcal{H}\right], \tag{5.5}$$
$$i\hbar\dot{\mathbf{D}}\left(\mathbf{r},\mathrm{t}\right)=\left[\mathbf{D}\left(\mathbf{r},\mathrm{t}\right),\mathcal{H}\right], \tag{5.6}$$

by defining $\mathcal{H}$ as the free space energy of the photon field given by

$$\mathcal{H}=\int\mathrm{d}\mathbf{r}\left[\frac{1}{2\epsilon_{0}}\mathbf{D}\left(\mathbf{r},\mathrm{t}\right)\cdot\mathbf{D}\left(\mathbf{r},\mathrm{t}\right)+\frac{\mu_{0}}{2}\mathbf{H}\left(\mathbf{r},\mathrm{t}\right)\cdot\mathbf{H}\left(\mathbf{r},\mathrm{t}\right)\right], \tag{5.7}$$

subject to the usual equal time commutation relations on the Cartesian components of the canonical variables denoted by subscripts

$$\left[\mathrm{D_{i}}\left(\mathbf{r},\mathrm{t}\right),\mathrm{D_{j}}\left(\mathbf{r}',\mathrm{t}\right)\right]=0, \tag{5.8}$$
$$\left[\mathrm{H_{i}}\left(\mathbf{r},\mathrm{t}\right),\mathrm{H_{j}}\left(\mathbf{r}',\mathrm{t}\right)\right]=0, \tag{5.9}$$
$$\left[\mathrm{D_{i}}\left(\mathbf{r},\mathrm{t}\right),\mathrm{H_{j}}\left(\mathbf{r}',\mathrm{t}\right)\right]=\frac{\mathrm{i}\hbar}{\mu_{0}}\epsilon_{\mathrm{jkl}}\frac{\partial}{\partial\mathrm{l}'}\boldsymbol{\delta}\left(\mathbf{r}-\mathbf{r}'\right)=\frac{\mathrm{i}\hbar}{\mu_{0}}\nabla\times\boldsymbol{\delta}\left(\mathbf{r}-\mathbf{r}'\right), \tag{5.10}$$

where ϵ_{jkl} is the Levi-Civita tensor. This is the approach adopted in the earliest attempts to quantise the radiation field [151, 152] and can be easily adapted to encompass dielectric media in regions far away from any resonances or dissipation by

the substitutions $\epsilon_0 \rightarrow \epsilon_0\epsilon$ and $\mu_0 \rightarrow \mu_0\mu$. The Hamiltonian in this case is given by

$$\mathcal{H} = \int \mathrm{d}\mathbf{r} \left[\frac{1}{2\epsilon_0\epsilon} \mathbf{D}(\mathbf{r},\mathrm{t}) \cdot \mathbf{D}(\mathbf{r},\mathrm{t}) + \frac{\mu_0\mu}{2} \mathbf{H}(\mathbf{r},\mathrm{t}) \cdot \mathbf{H}(\mathbf{r},\mathrm{t}) \right] \tag{5.11}$$

and solving the Heisenberg equations of motion for the canonical variables yields the Maxwell equations in matter [153–157]

$$\dot{\mathbf{H}}(\mathbf{r},\mathrm{t}) = -\mathrm{c}^2 \nabla \times \frac{\mathbf{D}(\mathbf{r},\mathrm{t})}{\epsilon}, \tag{5.12}$$

$$\dot{\mathbf{D}}(\mathbf{r},\mathrm{t}) = \nabla \times \mu \mathbf{H}(\mathbf{r},\mathrm{t}), \tag{5.13}$$

where the approach is valid given that the dispersion of the material over the bandwidth of the light is small.

5.2 Field Quantisation in Dispersive, Non-Dissipative Media

To describe the field quantisation procedure in spectral regions where material dispersion is important requires more care. Two approaches are possible. Macroscopic approaches assume a phenomenological dielectric function and begin from the Maxwell equations for non-dissipative media. Milonni calculates classically the electromagnetic energy density in a dispersive dielectric and utilises the result to normalise the electromagnetic fields [158]. Loudon and Santos make an equivalent modal expansion of the electromagnetic fields, applying the appropriate commutation relations to fix the orthonormality of the mode functions [159]. Alternatively a microscopic approach can be taken, explicitly modelling the medium as a bosonic field coupled to the electromagnetic fields. Such an approach is rigorous, allowing for the quantisation of the coupled light-matter system and for subsequent calculation of the system eigenmodes. This was first carried out by Hopfield who diagonalised the Hamiltonian of an isotropic dispersive dielectric. The normal modes of the coupled light-matter system were found to be linear superpositions of the uncoupled modes with dispersive frequencies dependant on the uncoupled mode dispersion [97]. Huttner *et al.* utilised a Hopfield model finding that the total energy in the system differed from the electromagnetic energy by a factor dependant on the photonic group velocity demonstrating the necessity of treating the matter correctly in dispersive systems [160]. This condition is equivalent to that derived by Milonni [158].

Free Space Hopfield Diagonalisation of Inhomogeneous Light Matter Systems

The method was extended to the inhomogeneous case of a planar, dispersive microcavity where it was shown that a modal expansion of the fields is possible under appropriate redefinitions of the orthonormality and completeness relations [161]. Drummond and Hillery extended this microscopic approach to describe multiple resonances of the matter [162] eventually recovering the Sellmeir dispersion relation [163]. Even in this complex example, the normalisation was found to obey a simple relation to the group velocity. In this section we follow the microscopic approach, describing the system by the Lagrangian density for the electromagnetic field interacting with a resonant dielectric characterised by an inhomogeneous transverse frequency $\omega_{\mathrm{T}}(\mathbf{r})$ and density $\rho(\mathbf{r})$

$$\mathcal{L}_0(\mathbf{r})=\int d\mathbf{r}\left[\frac{\epsilon_0}{2}\mathrm{E}(\mathbf{r})^2-\frac{1}{2\mu_0}\mathrm{B}(\mathbf{r})^2+\frac{\rho(\mathbf{r})}{2}\dot{\mathrm{X}}(\mathbf{r})^2-\frac{\rho(\mathbf{r})\omega_{\mathrm{T}}(\mathbf{r})^2}{2}\mathrm{X}(\mathbf{r})^2 \right. \\ \left. -\kappa(\mathbf{r})\dot{\mathbf{X}}(\mathbf{r})\cdot\mathbf{A}(\mathbf{r})-\mathrm{U}(\mathbf{r})\nabla\left[\kappa(\mathbf{r})\mathbf{X}(\mathbf{r})\right]\right],$$

where the electric and magnetic field components $\mathbf{E}(\mathbf{r}),\mathbf{B}(\mathbf{r})$, relate to the vector and scalar potentials $\mathbf{A}(\mathbf{r})$ and $\mathrm{U}(\mathbf{r})$ by

$$\mathbf{E}(\mathbf{r})=-\nabla\mathrm{U}(\mathbf{r})-\dot{\mathbf{A}}(\mathbf{r}), \tag{5.14}$$

$$\mathbf{B}(\mathbf{r})=\nabla\times\mathbf{A}(\mathbf{r}), \tag{5.15}$$

and the field $\mathbf{X}(\mathbf{r})$ describes the degrees of freedom of the matter resonance [160]. The strength of the light-matter coupling is dependent upon a spatially inhomogeneous constant $\kappa(\mathbf{r})$. Now in order to simplify the interaction term we add to our Lagrangian the time derivative of the function $\kappa(\mathbf{r})\mathbf{X}(\mathbf{r})\cdot\mathbf{A}(\mathbf{r})$, this is a unitary transform

$$\hat{\mathrm{U}}=\exp\left[\frac{i}{\hbar}\int\mathrm{d}\mathbf{r}\kappa(\mathbf{r})\mathbf{X}(\mathbf{r})\cdot\mathbf{A}(\mathbf{r})\right], \tag{5.16}$$

and is known as the Power-Zienau-Wooley (PZW) transform [164]. The transformed Lagrangian density is given by

$$\mathcal{L}_0'(\mathbf{r})=\int d\mathbf{r}\left[\frac{\epsilon_0}{2}\mathrm{E}(\mathbf{r})^2-\frac{1}{2\mu_0}\mathrm{B}(\mathbf{r})^2+\frac{\rho(\mathbf{r})}{2}\dot{\mathrm{X}}(\mathbf{r})^2-\frac{\rho(\mathbf{r})\omega_{\mathrm{T}}(\mathbf{r})^2}{2}\mathrm{X}(\mathbf{r})^2 \right. \\ \left. +\kappa(\mathbf{r})\mathbf{X}(\mathbf{r})\cdot\dot{\mathbf{A}}(\mathbf{r})-\mathrm{U}(\mathbf{r})\nabla\left[\kappa(\mathbf{r})\mathbf{X}(\mathbf{r})\right]\right].$$

Calculation of the canonical momenta

$$\mathbf{\Pi}=\frac{\partial\mathcal{L}_0'}{\partial\dot{\mathbf{A}}}=\epsilon_0\left(\dot{\mathbf{A}}+\nabla U\right)+\kappa\mathbf{X}=-\mathbf{D}, \tag{5.17}$$

$$\mathbf{P}=\frac{\partial\mathcal{L}_0'}{\partial\dot{\mathbf{X}}}=\rho\dot{\mathbf{X}}, \tag{5.18}$$

allows us to calculate the Hamiltonian density of the system in the usual way as

$$\mathcal{H}_0\left(\mathbf{r}\right)=\frac{\mathrm{D}^2}{2\epsilon_0}+\frac{\mu_0\mathrm{H}^2}{2}+\frac{\mathrm{P}^2}{2\rho}+\frac{\rho\omega_\mathrm{L}^2\mathrm{X}^2}{2}-\frac{\kappa}{\epsilon_0}\mathbf{X}\cdot\mathbf{D}, \tag{5.19}$$

where we have utilised the renormalised frequency

$$\omega_\mathrm{L}^2=\omega_\mathrm{T}^2+\frac{\kappa^2}{\epsilon_0\rho}, \tag{5.20}$$

and the magnetic field $\mathbf{H}=\mathbf{B}/\mu_0$. In the PZW gauge the canonical momentum $\mathbf{D}$ is purely transverse and the matter couples to the fields through a simple quadratic interaction term. The Hamiltonian is quantised by imposition of the usual commutation relations between canonical variables

$$[\mathbf{X}(\mathbf{r}),\mathbf{P}(\mathbf{r}')]=i\hbar\boldsymbol{\delta}(\mathbf{r}-\mathbf{r}'), \tag{5.21}$$

$$[\mathbf{D}(\mathbf{r}),\mathbf{A}(\mathbf{r}')]=i\hbar\boldsymbol{\delta}^\mathrm{T}(\mathbf{r}-\mathbf{r}'), \tag{5.22}$$

where $\boldsymbol{\delta}^\mathrm{T}\left(\mathbf{r}-\mathbf{r}'\right)$ is the transverse delta function. From Eq. 5.21 we can derive the further commutation relation between electric displacement and magnetic fields

$$[\mathbf{D}(\mathbf{r}),\mathbf{H}(\mathbf{r}')]=\frac{i\hbar}{\mu_0}\nabla'\times\boldsymbol{\delta}(\mathbf{r}-\mathbf{r}'), \tag{5.23}$$

where the prime on ∇ denotes its action upon primed variables. At this stage we elect to retain the position-momentum basis rather than the equivalent creation-annihilation one utilised by Hopfield to make our theory as clear as possible. As our Hamiltonian is quadratic we now follow the method of [97, 160, 162] and propose a normal mode with the form of a linear superposition of the constituent fields termed a polariton. The form of this mode is

$$\mathcal{K}=\int\mathrm{d}\mathbf{r}\left[\boldsymbol{\alpha}\cdot\mathbf{D}+\boldsymbol{\beta}\cdot\mathbf{H}+\boldsymbol{\gamma}\cdot\mathbf{P}+\boldsymbol{\eta}\cdot\mathbf{X}\right], \tag{5.24}$$

where the weightings $\boldsymbol{\alpha}, \boldsymbol{\beta}, \boldsymbol{\gamma}, \boldsymbol{\eta}$ are to be referred to as the Hopfield coefficients of the polaritonic mode $\mathcal{K}$. As we expect this mode to diagonalise the Hamiltonian $\mathcal{H}_0$, it must obey the Heisenberg equation of motion

$$[\mathcal{K}, \mathcal{H}_0] = \hbar\omega\mathcal{K} \tag{5.25}$$

which gives by use of Eq. 5.19-5.24

$$\begin{aligned}[\mathcal{K}, \mathcal{H}_0] = i\hbar \int \mathrm{d}\mathbf{r} \Bigg[& [\nabla\times\boldsymbol{\alpha}]\cdot\mathbf{H} - c^2\,[\nabla\times\boldsymbol{\beta}]\cdot\mathbf{D} + \kappa\, c^2\,[\nabla\times\boldsymbol{\beta}]\cdot\mathbf{X} \\ & - \rho\omega_{\mathrm{L}}^2\boldsymbol{\gamma}\cdot\mathbf{X} + \frac{\kappa}{\epsilon_0}\boldsymbol{\gamma}\cdot\mathbf{D} + \frac{1}{\rho}\boldsymbol{\eta}\cdot\mathbf{P}\Bigg], \\ = \hbar\omega \int \mathrm{d}\mathbf{r}\, & \boldsymbol{\alpha}\cdot\mathbf{D} + \boldsymbol{\beta}\cdot\mathbf{H} + \boldsymbol{\gamma}\cdot\mathbf{P} + \boldsymbol{\eta}\cdot\mathbf{X},\end{aligned} \tag{5.26}$$

which we can restate by collecting like terms as the equation system

$$\omega\boldsymbol{\alpha} = -ic^2\nabla\times\boldsymbol{\beta} + i\frac{[\kappa\boldsymbol{\gamma}]^{\mathrm{T}}}{\epsilon_0}, \tag{5.27}$$

$$\omega\boldsymbol{\beta} = i\nabla\times\boldsymbol{\alpha}, \tag{5.28}$$

$$\omega\boldsymbol{\gamma} = i\frac{\boldsymbol{\eta}}{\rho}, \tag{5.29}$$

$$\omega\boldsymbol{\eta} = i\kappa\, c^2\nabla\times\boldsymbol{\beta} - i\rho\omega_{\mathrm{L}}^2\boldsymbol{\gamma}. \tag{5.30}$$

and we have therefore transformed the equation over the field operators Eq. 5.25 into a differential one over the Hopfield coefficients. This equation system is equivalent to the Maxwell equations in dispersive, non-dissipative media. It has been shown that polarisable matter is stable against superradiant phase transitions in both the homogeneous case with the stability condition for the inhomogeneous case coinciding with the point-wise condition of stability for the corresponding homogeneous system [165]. In the homogeneous case, by evaluating Eq. 5.27 and Eq. 5.30 for $\omega=0$, we infer the stability condition $\omega_{\mathrm{T}}>0$ and for the remainder we will assume this to be satisfied with ω_{T} at least arbitrarily small and positive. We can solve the equation system by introduction of the discrete eigenmodes

$$|\boldsymbol{\Psi}_{\mathrm{n}}\rangle = (\boldsymbol{\alpha}_{\mathrm{n}}, \boldsymbol{\beta}_{\mathrm{n}}, \boldsymbol{\gamma}_{\mathrm{n}}, \boldsymbol{\eta}_{\mathrm{n}}), \tag{5.31}$$

with corresponding discrete eigenvalues ω_{n}. By inspection it is obvious that the set also admits solutions of form

$$|\boldsymbol{\Psi}_{\bar{\mathrm{n}}}\rangle=\left(\bar{\boldsymbol{\alpha}}_{\mathrm{n}},\bar{\boldsymbol{\beta}}_{\mathrm{n}},\bar{\boldsymbol{\gamma}}_{\mathrm{n}},\bar{\boldsymbol{\eta}}_{\mathrm{n}}\right), \tag{5.32}$$

with the discrete eigenvalue $\omega_{\bar{\mathrm{n}}}=-\omega_{\mathrm{n}}$. This means that each positive frequency eigenmode $|\boldsymbol{\Psi}\rangle_{\mathrm{n}}$ corresponds to a negative frequency one $|\boldsymbol{\Psi}\rangle_{\bar{\mathrm{n}}}$. We refer to positive (negative) energy polaritonic operators as creation (annihilation) operators for the coupled excitations.

To proceed in convenient fashion we introduce the new variable $\boldsymbol{\theta}$ by adding to the pure transverse quantity $\boldsymbol{\alpha}$ a term proportional to the longitudinal component of $\boldsymbol{\gamma}$ to eliminate the reference to the transverse component of $\boldsymbol{\gamma}$ in Eq. 5.27

$$\boldsymbol{\theta}=\boldsymbol{\alpha}+i\frac{\left[\kappa\boldsymbol{\gamma}\right]^{\mathrm{L}}}{\omega\epsilon_0}, \tag{5.33}$$

where L refers to the longitudinal component of the bracketed term. Now manipulating Eq. 5.27-5.30 to eliminate the other variables through

$$\boldsymbol{\alpha}=\boldsymbol{\theta}^{\mathrm{T}}, \tag{5.34}$$

$$\boldsymbol{\beta}=\frac{i}{\omega}\nabla\times\boldsymbol{\theta}, \tag{5.35}$$

$$\boldsymbol{\gamma}=i\frac{\kappa\omega}{\rho\left(\omega_{\mathrm{T}}^2-\omega^2\right)}\boldsymbol{\theta}, \tag{5.36}$$

$$\boldsymbol{\eta}=\frac{\kappa\omega^2}{\omega_{\mathrm{T}}^2-\omega^2}\boldsymbol{\theta}, \tag{5.37}$$

we can rewrite the set as a function of $\boldsymbol{\theta}$

$$\nabla\times\nabla\times\boldsymbol{\theta}=\frac{\omega^2\epsilon\left(\omega\right)}{\mathrm{c}^2}\boldsymbol{\theta}, \tag{5.38}$$

where

$$\epsilon\left(\omega\right)=\frac{\omega_{\mathrm{L}}^2-\omega^2}{\omega_{\mathrm{T}}^2-\omega^2}, \tag{5.39}$$

is the dispersive dielectric function equivalent to that derivable from an undamped Lorentz model of a dielectric if ω_{L} and ω_{T} are recognised as longitudinal and transverse resonant frequencies. This converges to the Drude model describing a metal in the limit $\omega_{\mathrm{T}}\rightarrow 0^{+}$. This result being equivalent to the electromagnetic wave-equation in

magnetically inactive media allows for the application of the techniques of classical electromagnetism to be utilised to calculate the Hopfield coefficients. The dispersive nature of the dielectric function however means the operator on $\boldsymbol{\theta}$ is frequency dependant and therefore it is not in the form of an eigenvalue equation. To proceed we revert to the full equation set 5.27-5.30 and consider the algebraic structure of our solutions. Once the eigenmodes have been calculated we need to apply an appropriate normalisation found from the bosonic nature of the polariton modes

$$\left[\mathcal{K}_{\mathrm{m}}, \mathcal{K}_{\mathrm{n}}^{\dagger}\right] = \delta_{\mathrm{m,n}} \operatorname{sgn}(\omega_{\mathrm{n}}), \tag{5.40}$$

where $\operatorname{sgn}(\omega) = \frac{\omega}{|\omega|}$ is the sign function. This gives the usual solution on restricting both m and n to the positive frequency solutions. On expanding the commutator we find

$$\begin{aligned}
\left[\mathcal{K}_{\mathrm{m}}, \mathcal{K}_{\mathrm{n}}^{\dagger}\right] &= i\hbar \int \mathrm{d}\mathbf{r}\, \frac{1}{\mu_0} \boldsymbol{\alpha}_{\mathrm{m}} \cdot \nabla \times \bar{\boldsymbol{\beta}}_{\mathrm{n}} - \frac{1}{\mu_0} \nabla \times \boldsymbol{\beta}_{\mathrm{m}} \cdot \bar{\boldsymbol{\alpha}}_{\mathrm{n}} + \boldsymbol{\eta}_{\mathrm{m}} \cdot \bar{\boldsymbol{\gamma}}_{\mathrm{n}} - \boldsymbol{\gamma}_{\mathrm{m}} \cdot \bar{\boldsymbol{\eta}}_{\mathrm{n}}, \\
&= \hbar \epsilon_0 \int \mathrm{d}\mathbf{r} \frac{\epsilon(\omega_{\mathrm{m}}) \omega_{\mathrm{m}}^2 - \epsilon(\omega_{\mathrm{n}}) \omega_{\mathrm{n}}^2}{\omega_{\mathrm{m}} - \omega_{\mathrm{n}}} \boldsymbol{\theta}_{\mathrm{m}} \cdot \bar{\boldsymbol{\theta}}_{\mathrm{n}}, \qquad (5.41) \\
&= \delta_{\mathrm{m,n}} \operatorname{sgn}(\omega_{\mathrm{n}}). \qquad (5.42)
\end{aligned}$$

Note that in the case m=n we can easily express this as

$$2\hbar\omega_{\mathrm{n}}\epsilon_0 \int \mathrm{d}\mathbf{r}\, \epsilon\left(\omega_{\mathrm{n}}\right) \nu(\omega_{\mathrm{n}})\, \boldsymbol{\theta}_{\mathrm{n}} \cdot \bar{\boldsymbol{\theta}}_{\mathrm{n}} = \operatorname{sgn}(\omega_{\mathrm{n}}), \tag{5.43}$$

where the function $\nu(\omega)$ is given by

$$\nu(\omega) = 1 + \frac{1}{\epsilon\left(\omega\right)} \frac{\mathrm{d}\left[\epsilon(\omega)\omega\right]}{\mathrm{d}\omega} = \frac{\mathrm{v}^{\mathrm{G}}\left(\omega\right)}{\mathrm{v}^{\mathrm{P}}\left(\omega\right)}, \tag{5.44}$$

which is equivalent to the ratio of the local group and phase velocities $\mathrm{v}^{\mathrm{G}}\left(\omega\right)$ and $\mathrm{v}^{\mathrm{P}}\left(\omega\right)$ [166]. This result is equivalent to the normalisation condition applied from energetic arguments by Milonni [158], from application of commutation relations by Loudon [159] and by Huttner from quantising the electromagnetic flux in the homogeneous case [160].

Now it is informative to invert the system, expressing the macroscopic field operators in the Lagrangian as linear combinations of the polaritonic operators

$$\mathbf{D}=\sum_{\mathrm{n}}\mathbf{f}_{\mathrm{n}}^{\mathrm{D}}\mathcal{K}_{\mathrm{n}}=\sum_{\mathrm{n}}{}'\left[\mathbf{f}_{\mathrm{n}}^{\mathrm{D}}\mathcal{K}_{\mathrm{n}}+\bar{\mathbf{f}}_{\mathrm{n}}^{\mathrm{D}}\mathcal{K}_{\mathrm{n}}^{\dagger}\right], \tag{5.45}$$

$$\mathbf{H}=\sum_{\mathrm{n}}\mathbf{f}_{\mathrm{n}}^{\mathrm{H}}\mathcal{K}_{\mathrm{n}}=\sum_{\mathrm{n}}{}'\left[\mathbf{f}_{\mathrm{n}}^{\mathrm{H}}\mathcal{K}_{\mathrm{n}}+\bar{\mathbf{f}}_{\mathrm{n}}^{\mathrm{H}}\mathcal{K}_{\mathrm{n}}^{\dagger}\right], \tag{5.46}$$

$$\mathbf{P}=\sum_{\mathrm{n}}\mathbf{f}_{\mathrm{n}}^{\mathrm{P}}\mathcal{K}_{\mathrm{n}}=\sum_{\mathrm{n}}{}'\left[\mathbf{f}_{\mathrm{n}}^{\mathrm{P}}\mathcal{K}_{\mathrm{n}}+\bar{\mathbf{f}}_{\mathrm{n}}^{\mathrm{P}}\mathcal{K}_{\mathrm{n}}^{\dagger}\right], \tag{5.47}$$

$$\mathbf{X}=\sum_{\mathrm{n}}\mathbf{f}_{\mathrm{n}}^{\mathrm{X}}\mathcal{K}_{\mathrm{n}}=\sum_{\mathrm{n}}{}'\left[\mathbf{f}_{\mathrm{n}}^{\mathrm{X}}\mathcal{K}_{\mathrm{n}}+\bar{\mathbf{f}}_{\mathrm{n}}^{\mathrm{X}}\mathcal{K}_{\mathrm{n}}^{\dagger}\right], \tag{5.48}$$

where the primed sums are intended to be only on positive energy solutions. We can calculate the positive energy expansion coefficients by application of the field commutation relations in Eq. 5.21-5.23 and the definition of the polariton operator in Eq. 5.24

$$\mathbf{f}_{\mathrm{n}}^{\mathrm{D}}=\left[\mathbf{D},\mathcal{K}_{\mathrm{n}}^{\dagger}\right]=-i\frac{\hbar}{\mu_0}\nabla\times\bar{\boldsymbol{\beta}}_{\mathrm{n}}, \tag{5.49}$$

$$\mathbf{f}_{\mathrm{n}}^{\mathrm{H}}=\left[\mathbf{H},\mathcal{K}_{\mathrm{n}}^{\dagger}\right]=i\frac{\hbar}{\mu_0}\nabla\times\bar{\boldsymbol{\alpha}}_{\mathrm{n}}, \tag{5.50}$$

$$\mathbf{f}_{\mathrm{n}}^{\mathrm{P}}=\left[\mathbf{P},\mathcal{K}_{\mathrm{n}}^{\dagger}\right]=-i\hbar\bar{\boldsymbol{\eta}}_{\mathrm{n}}, \tag{5.51}$$

$$\mathbf{f}_{\mathrm{n}}^{\mathrm{X}}=\left[\mathbf{X},\mathcal{K}_{\mathrm{n}}^{\dagger}\right]=i\hbar\bar{\boldsymbol{\gamma}}_{\mathrm{n}}. \tag{5.52}$$

To verify that the polaritonic operator Eq. 5.24 in fact diagonalises the Hamiltonian Eq. 5.19 we need to prove that the system Eq. 5.27-5.30 is self adjoint for all choices of $|\boldsymbol{\Psi}_{\mathrm{n}}\rangle=(\boldsymbol{\alpha}_{\mathrm{n}},\boldsymbol{\beta}_{\mathrm{n}},\boldsymbol{\gamma}_{\mathrm{n}},\boldsymbol{\eta}_{\mathrm{n}})$. In order to achieve this we define the inner product between two wavefunctions $|\boldsymbol{\Psi}\rangle\,,|\boldsymbol{\Psi}'\rangle$ as the bosonic commutator given in Eq. 5.151

$$\langle\boldsymbol{\Psi}|\boldsymbol{\Psi}'\rangle=i\hbar\int\mathrm{d}\mathbf{r}\left[\frac{1}{\mu_0}\boldsymbol{\alpha}\cdot\nabla\times\bar{\boldsymbol{\beta}}'-\frac{1}{\mu_0}\nabla\times\boldsymbol{\beta}\cdot\bar{\boldsymbol{\alpha}}'+\boldsymbol{\eta}\cdot\bar{\boldsymbol{\gamma}}'-\boldsymbol{\gamma}\cdot\bar{\boldsymbol{\eta}}'\right]. \tag{5.53}$$

This choice of normalisation would ensure the orthonormality of the eigenmodes, however from Eq. 5.41 we see immediately that the inner product is not positive-definite meaning the space of wavefunction $|\boldsymbol{\Psi}\rangle$ does not form a Hilbert space over the inner product Eq. 5.53. We can however form a Kreĭn space [167] with a signature

operator given by [99]

$$\eta = \sum_{\mathrm{n}}{}' \left[|\mathbf{\Psi}_{\mathrm{n}}\rangle \langle \mathbf{\Psi}_{\mathrm{n}}| - |\mathbf{\Psi}_{\bar{\mathrm{n}}}\rangle \langle \mathbf{\Psi}_{\bar{\mathrm{n}}}| \right], \tag{5.54}$$

which allows for recovery of all the usual properties of orthonormality and completeness. If we rewrite the equation set 5.27-5.30 in operatorial form as

$$\mathcal{B}_0 \, |\mathbf{\Psi}\rangle = \omega \, |\mathbf{\Psi}\rangle \, , \tag{5.55}$$

we need impose that the operator $\mathcal{B}_0$ is self-adjoint with respect to the inner product we defined in 5.53 meaning

$$\langle \mathbf{\Psi'} | \mathcal{B}_0 \mathbf{\Psi} \rangle - \langle \mathcal{B}_0 \mathbf{\Psi'} | \mathbf{\Psi} \rangle = 0, \tag{5.56}$$

which can be rewritten by use of Eq. 5.27-5.30 and 5.53 as

$$\int \mathrm{d}\mathbf{r} \left[\boldsymbol{\alpha} \cdot \nabla \times \nabla \times \bar{\boldsymbol{\alpha}}' - \bar{\boldsymbol{\alpha}}' \cdot \nabla \times \nabla \times \boldsymbol{\alpha} \right] = 0, \tag{5.57}$$

which is satisfied if the space is restricted by $\nabla \cdot \boldsymbol{\alpha}$ or the transversality of the displacement field $\nabla \cdot \mathbf{D} = 0$. We can recast this as a boundary condition on the edge of the quantisation volume V

$$\int_{\partial \mathrm{V}} \mathrm{d}\mathbf{S} \cdot \mathbf{f} = 0, \tag{5.58}$$

where $\mathrm{d}\mathbf{S}$ is the unit vector normal to the infinitesimal surface element, and $\mathbf{f}$ is a current operator, which is given in Cartesian coordinates as

$$\mathrm{f_j} = \mathrm{i}\boldsymbol{\alpha} \cdot \partial_{\mathrm{j}} \bar{\boldsymbol{\alpha}} - \mathrm{i}\bar{\boldsymbol{\alpha}} \cdot \partial_{\mathrm{j}} \boldsymbol{\alpha}. \tag{5.59}$$

If these conditions are satisfied, then our equation system is self adjoint and a complete set of polaritonic operators may be derived. We can rewrite our boundary condition as a function of the macroscopic field operators as

$$\int_{\partial \mathrm{V}} \mathrm{d}\mathbf{S} \cdot \langle \mathbf{\Psi}_{\mathrm{n}}| : \mathbf{D} \times \mathbf{H} : |\mathbf{\Psi}_{\mathrm{n}}\rangle = 0, \tag{5.60}$$

which is an expression of the conservation of momentum. The completeness relation in our Kreĭn space is given by

$$\langle \mathbf{\Psi} | \mathbf{\Psi'} \rangle = \langle \mathbf{\Psi} | \, \eta \, | \mathbf{\Psi'} \rangle \, , \tag{5.61}$$

which is expandable in terms of the relations between the Hopfield coefficients as

$$\sum_{\mathrm{n}}{}' \left[\boldsymbol{\alpha}_{\mathrm{n}}(\mathbf{r}') \cdot \nabla \times \bar{\boldsymbol{\beta}}_{\mathrm{n}}(\mathbf{r}) - \bar{\boldsymbol{\alpha}}_{\mathrm{n}}(\mathbf{r}') \cdot \nabla \times \boldsymbol{\beta}_{\mathrm{n}}(\mathbf{r}) \right] = i \frac{\mu_0}{\hbar} \delta^{\mathrm{T}}(\mathbf{r} - \mathbf{r}'), \tag{5.62}$$

which allows us to calculate the commutation relations between the macroscopic fields utilising the relations we used to quantise the theory allowing for verification of the consistency of our procedure

$$[\mathbf{D}(\mathbf{r}), \mathbf{H}(\mathbf{r}')] = \frac{\hbar^2}{\mu_0^2} \sum_{\mathrm{n}}{}' \left[\nabla \times \bar{\boldsymbol{\beta}}_{\mathrm{n}}(\mathbf{r}) \cdot \nabla' \times \boldsymbol{\alpha}_{\mathrm{n}}(\mathbf{r}') - \nabla \times \boldsymbol{\beta}_{\mathrm{n}}(\mathbf{r}) \cdot \nabla' \times \bar{\boldsymbol{\alpha}}_{\mathrm{n}}(\mathbf{r}') \right], \tag{5.63}$$

$$= \frac{\hbar^2}{\mu_0^2} \sum_{\mathrm{n}}{}' \nabla' \times \left[\nabla \times \bar{\boldsymbol{\beta}}_{\mathrm{n}}(\mathbf{r}) \cdot \boldsymbol{\alpha}_{\mathrm{n}}(\mathbf{r}') - \nabla \times \boldsymbol{\beta}_{\mathrm{n}}(\mathbf{r}) \cdot \bar{\boldsymbol{\alpha}}_{\mathrm{n}}(\mathbf{r}') \right], \tag{5.64}$$

$$= i \frac{\hbar}{\mu_0} \nabla' \times \delta^{\mathrm{T}}(\mathbf{r} - \mathbf{r}'), \tag{5.65}$$

equivalent commutation relations for the other macroscopic components are derivable. Finally we proved that the Hamiltonian in 5.19 can be put in the diagonal form

$$\mathcal{H}_0 = \sum_{\mathrm{n}}{}' \hbar \omega_{\mathrm{n}} \, \mathcal{K}_{\mathrm{n}}^{\dagger} \mathcal{K}_{\mathrm{n}}. \tag{5.66}$$

5.3 Application: Phonon Polariton at a Planar Interface

As an illustration of the theory derived above we will apply it to the system discussed in Chapter 2 consisting of a planar interface between vacuum and a polar dielectric. Usually the approach followed is a macroscopic one as the explicit properties of the matter degrees of freedom are not of interest. The quantisation of the electromagnetic field in for a metallic halfspace was first reported by Elson and Ritchie in the lossless case describing the metal by a Drude model [168]. More recently Archambault *et al.* quantised the surface mode through its electromagnetic energy in the absence of loss, this is entirely equivalent to the normalisation condition we calculate from the polariton self-commutator in Eq. 5.41 [149]. An equivalent normalisation may also be calculated through the Poynting flux [169]. It is entirely feasible to extend such approaches to include dissipation by the general theory of Gruner [170]. The first microscopic description of plasma waves of the free electron gas was provided by Bohm and Pines who bosonise collective excitations mediated by the long range Coulomb

interaction for a homogeneous system [171]. More recently, analogous quantisation procedures have been applied to the metallic halfspace to quantise the surface plasmon [150]. The procedure however is *ad hoc* and the Hopfield transformation is in the end non-invertible. Our approach allows for an invertible diagonalisation of the interface problem. Our polar dielectric described by the Lorentz dielectric function Eq. 5.39 supports surface phonon polariton excitations [172].

If the surface is taken to lie in the x−y plane the system is described as

$$\begin{aligned}\epsilon\left(\omega, \mathrm{z}>0\right)&=1,\\ \epsilon\left(\omega, \mathrm{z}<0\right)&=\epsilon_{\mathrm{L}}\left(\omega\right)=\frac{\omega_{\mathrm{L}}^2-\omega^2}{\omega_{\mathrm{T}}^2-\omega^2},\end{aligned} \tag{5.67}$$

where ω_{L} and ω_{T} are the longitudinal and transverse optical phonon frequencies, linked between them by the Lyddane-Sachs-Teller relation [46].

As in the classical interface problem we solve the wave equation 5.38 with dielectric function Eq. 5.67, this yields propagative and evanescent solutions. We label the propagative ones which impinge on the interface from the vacuum or dielectric by their transverse magnetic (TM) or transverse electric (TE) polarisation and their wavevector in the medium of origin $\mathbf{k}=(\mathbf{k}_{\parallel}, \mathrm{k_z})$. Waves incident from the dielectric are also indexed by their bulk polariton branch ±. Surface modes exist for $|\mathbf{k}_{\parallel}|\geq\omega_{\mathrm{T}}/\mathrm{c}$ and are indexed by their in-plane wavevector $\mathbf{k}_{\parallel}$. We can express the general polaritonic operators as

$$\begin{aligned}\mathcal{K}_{\mathbf{k}^\sigma}^{\sigma}=\int \mathrm{d}\mathbf{r}\Bigg[&\boldsymbol{\alpha}_{\mathbf{k}^\sigma}^{\sigma}\cdot\mathbf{D}+\frac{i}{\omega_{\mathbf{k}^\sigma}}\nabla\times\boldsymbol{\alpha}_{\mathbf{k}^\sigma}^{\sigma}\cdot\mathbf{H}\\ &+i\frac{\kappa\omega_{\mathbf{k}^\sigma}}{\rho\left(\omega_{\mathrm{T}}^2-\omega_{\mathbf{k}^\sigma}^2\right)}\boldsymbol{\alpha}_{\mathbf{k}^\sigma}^{\sigma}\cdot\mathbf{P}+\frac{\kappa\omega_{\mathbf{k}^\sigma}^2}{\left(\omega_{\mathrm{T}}^2-\omega_{\mathbf{k}^\sigma}^2\right)}\boldsymbol{\alpha}_{\mathbf{k}^\sigma}^{\sigma}\cdot\mathbf{X}\Bigg],\end{aligned} \tag{5.68}$$

where σ=[TMv, TM±, TEv, TE±, S] indexes the solutions class, and $\mathbf{k}^\sigma$ is the relative two- or three-dimensional wavevector.

TE Modes Incident from Vacuum

We can write the eigenmodes for TE modes propagating from vacuum as

$$\begin{aligned}\boldsymbol{\theta}_{\mathbf{k}}^{\mathrm{TEv}}(\mathbf{r}_{\parallel}, \mathrm{z}>0)&=\mathrm{N}_{\mathbf{k}}^{\mathrm{TEv}}\mathrm{e}^{-\mathrm{i}\mathbf{k}_{\parallel}\cdot\mathbf{r}_{\parallel}}\left(\mathrm{e}^{\mathrm{i}\mathrm{k_z}\mathrm{z}}+\mathrm{r}_{\mathbf{k}}^{\mathrm{TEv}}\mathrm{e}^{-\mathrm{i}\mathrm{k_z}\mathrm{z}}\right)\hat{\mathbf{e}}_{\perp},\\ \boldsymbol{\theta}_{\mathbf{k}}^{\mathrm{TEv}}(\mathbf{r}_{\parallel}, \mathrm{z}<0)&=\mathrm{N}_{\mathbf{k}}^{\mathrm{TEv}}\mathrm{t}_{\mathbf{k}}^{\mathrm{TEv}}\mathrm{e}^{-\mathrm{i}\mathbf{k}\cdot\mathbf{r}}\hat{\mathbf{e}}_{\perp},\end{aligned} \tag{5.69}$$

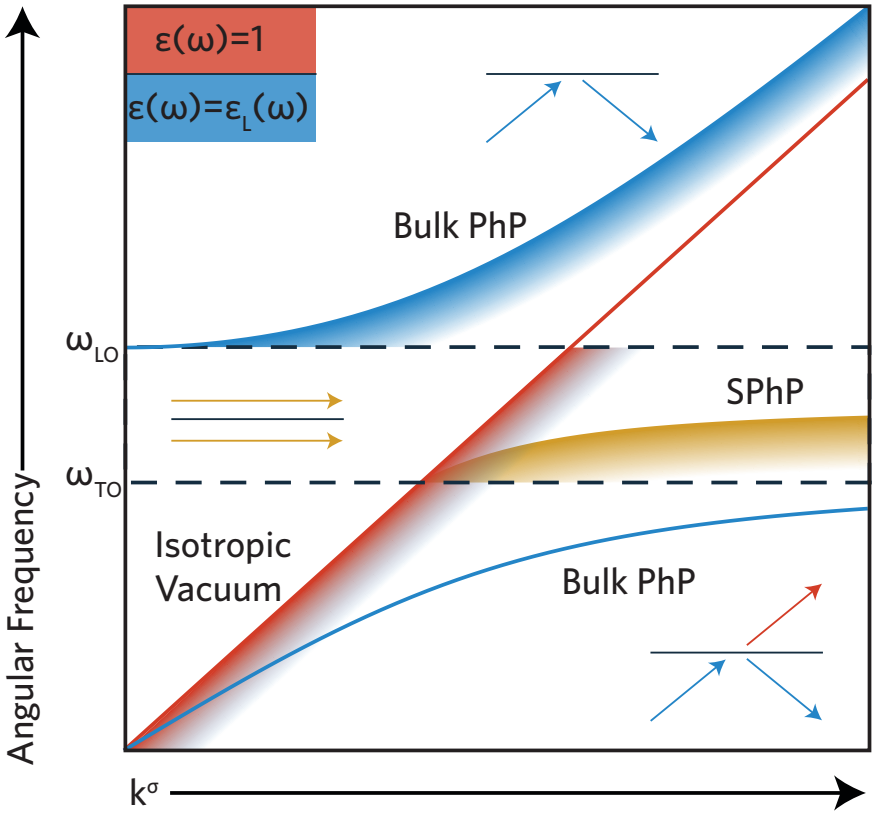


Figure 5.1: The inset illustrates the dielectric structure under study consisting of a halfspace characterised by dispersive dielectric function $\epsilon_{\mathrm{L}}(\omega)$ for $z<0$ and vacuum characterised by a unit dielectric function for $z>0$. The main figure illustrates the dispersion relations single photonic mode of an isotropic vacuum (red) and the two bulk phonon polariton modes of an isotropic polar dielectric (blue) as a function of wavevector magnitude. The modes of the coupled halfspace are formed by scattering from (to) the phonon polaritons to (from) the vacuum photon. Regions where scattering is forbidden are indicated by shading, here total internal reflection of the shaded mode occurs. In addition the dispersion of the surface phonon polariton is indicated in gold.

where the Fresnel coefficients read

$$\mathrm{r}_{\mathbf{k}}^{\mathrm{TEv}}=\frac{\mathrm{k_z}-\sqrt{\epsilon_{\mathrm{L}}\left(\omega_{\mathbf{k}}\right)\mathrm{k}^2-\mathrm{k}_{\parallel}^2}}{\mathrm{k_z}+\sqrt{\epsilon_{\mathrm{L}}\left(\omega_{\mathbf{k}}\right)\mathrm{k}^2-\mathrm{k}_{\parallel}^2}}, \tag{5.70}$$
$$\mathrm{t}_{\mathbf{k}}^{\mathrm{TEv}}=\frac{2\mathrm{k_z}}{\mathrm{k_z}+\sqrt{\epsilon_{\mathrm{L}}\left(\omega_{\mathbf{k}}\right)\mathrm{k}^2-\mathrm{k}_{\parallel}^2}},$$

and modes are normalised in the usual way through Eq. 5.41. Splitting the integral over the upper and lower halfspaces $\mathbf{r}^{>},\mathbf{r}^{<}$ we find

$$\delta_{\mathrm{m,n}}=\epsilon_0|\mathrm{N}_{\mathbf{k}}^{\mathrm{TEv}}|^2\Bigg[\left(\omega_{\mathrm{n}}+\omega_{\mathrm{m}}\right)\int \mathrm{d}\mathbf{r}^{>}\mathrm{e}^{-\mathrm{i}\left(\mathbf{k}_{\parallel,\mathrm{m}}-\mathbf{k}_{\parallel,\mathrm{n}}\right)\cdot\mathbf{r}_{\parallel}}\left(\mathrm{e}^{\mathrm{ik_{z,m}z}}+\mathrm{r}_{\mathbf{k}_{\mathrm{m}}}^{\mathrm{TEv}}\mathrm{e}^{-\mathrm{ik_{z,m}z}}\right)\left(\mathrm{e}^{-\mathrm{ik_{z,n}z}}+\mathrm{r}_{\mathbf{k}_{\mathrm{n}}}^{\mathrm{TEv}}\mathrm{e}^{\mathrm{ik_{z,n}z}}\right) \tag{5.71}$$
$$+\frac{\epsilon(\omega_{\mathrm{m}})\omega_{\mathrm{m}}^2-\epsilon(\omega_{\mathrm{n}})\omega_{\mathrm{n}}^2}{\omega_{\mathrm{m}}-\omega_{\mathrm{n}}}\mathrm{t}_{\mathbf{k}_{\mathrm{m}}}^{\mathrm{TEv}}\mathrm{t}_{\mathbf{k}_{\mathrm{n}}}^{\mathrm{TEv}}\int \mathrm{d}\mathbf{r}^{<}\mathrm{e}^{-\mathrm{i}(\mathbf{k}_{\mathrm{m}}-\mathbf{k}_{\mathrm{n}})\cdot\mathbf{r}}\Bigg], \tag{5.72}$$

and immediately we carry out the in-plane integral to get

$$\delta_{\mathrm{m,n}}=\epsilon_0\mathrm{L}^2|\mathrm{N}_{\mathbf{k}}^{\mathrm{TEv}}|^2\Bigg[\left(\omega_{\mathrm{n}}+\omega_{\mathrm{m}}\right)\int \mathrm{dz}^{>}\left(\mathrm{e}^{\mathrm{ik_{z,m}z}}+\mathrm{r}_{\mathbf{k}_{\mathrm{m}}}^{\mathrm{TEv}}\mathrm{e}^{-\mathrm{ik_{z,m}z}}\right)\left(\mathrm{e}^{-\mathrm{ik_{z,n}z}}+\mathrm{r}_{\mathbf{k}_{\mathrm{n}}}^{\mathrm{TEv},*}\mathrm{e}^{\mathrm{ik_{z,n}z}}\right) \tag{5.73}$$
$$+\frac{\epsilon(\omega_{\mathrm{m}})\omega_{\mathrm{m}}^2-\epsilon(\omega_{\mathrm{n}})\omega_{\mathrm{n}}^2}{\omega_{\mathrm{m}}-\omega_{\mathrm{n}}}\mathrm{t}_{\mathbf{k}_{\mathrm{m}}}^{\mathrm{TEv}}\mathrm{t}_{\mathbf{k}_{\mathrm{n}}}^{\mathrm{TEv},*}\int \mathrm{dz}^{<}\mathrm{e}^{\mathrm{i}(\mathrm{k_{z,m}}-\mathrm{k_{z,n}})\mathrm{z}}\Bigg]\delta^2\left(\mathbf{k}_{\parallel,\mathrm{n}}-\mathbf{k}_{\parallel,\mathrm{m}}\right), \tag{5.74}$$

where the quantisation length is given by $\mathcal{L}$ To calculate the out-of-plane integral the integration rules

$$\lim_{\nu\to 0^+}\int_{-\infty}^{0}\mathrm{dx}e^{i(\mathrm{k}-\mathrm{i}\nu)\mathrm{x}}=\mathcal{P}\left[-\frac{\mathrm{i}}{\mathrm{k}}\right]+\pi\delta\left(\mathrm{k}\right), \tag{5.75}$$

$$\lim_{\nu\to 0^+}\int_{0}^{\infty}\mathrm{dx}e^{i(\mathrm{k}+\mathrm{i}\nu)\mathrm{x}}=\mathcal{P}\left[\frac{\mathrm{i}}{\mathrm{k}}\right]+\pi\delta\left(\mathrm{k}\right), \tag{5.76}$$

are employed [173]. Here $\mathcal{P}$ refers to the principal part of the function. In the upper halfspace we calculate

$$\int \mathrm{dz}^{>}\left(\mathrm{e}^{\mathrm{ik_{z,m}z}}+\mathrm{r}_{\mathbf{k}_\mathrm{m}}^{\mathrm{TEv}}\mathrm{e}^{-\mathrm{ik_{z,m}z}}\right)\left(\mathrm{e}^{-\mathrm{ik_{z,n}z}}+\mathrm{r}_{\mathbf{k}_\mathrm{n}}^{\mathrm{TEv}}\mathrm{e}^{\mathrm{ik_{z,n}z}}\right), \tag{5.77}$$

$$=\int \mathrm{dz}^{>}\left[\mathrm{e}^{\mathrm{i(k_{z,m}-k_{z,n})z}}+\mathrm{r}_{\mathbf{k}_\mathrm{m}}^{\mathrm{TEv}}\mathrm{e}^{-\mathrm{i(k_{z,m}+k_{z,n})z}}+\mathrm{r}_{\mathbf{k}_\mathrm{n}}^{\mathrm{TEv},*}\mathrm{e}^{\mathrm{i(k_{z,m}+k_{z,n})z}}+\mathrm{r}_{\mathbf{k}_\mathrm{m}}^{\mathrm{TEv}}\mathrm{r}_{\mathbf{k}_\mathrm{n}}^{\mathrm{TEv},^*}\mathrm{e}^{-\mathrm{i(k_{z,m}-k_{z,n})z}}\right], \tag{5.78}$$

$$=\mathcal{P}\left[\frac{\mathrm{i}}{\mathrm{k_{z1,m}-k_{z1,n}}}\right]+\frac{\mathrm{L}}{2}\delta\left(\mathrm{k_{z1,m}-k_{z1,n}}\right)+\mathrm{r}_{\mathbf{k}_\mathrm{m}}^{\mathrm{TEv}}\mathcal{P}\left[-\frac{\mathrm{i}}{\mathrm{k_{z1,m}+k_{z1,n}}}\right]+\mathrm{r}_{\mathbf{k}_\mathrm{n}}^{\mathrm{TEv},*}\mathcal{P}\left[\frac{\mathrm{i}}{\mathrm{k_{z1,m}+k_{z1,n}}}\right] \tag{5.79}$$

$$+\mathrm{r}_{\mathbf{k}_\mathrm{m}}^{\mathrm{TEv}}\mathrm{r}_{\mathbf{k}_\mathrm{n}}^{\mathrm{TEv},*}\mathcal{P}\left[-\frac{\mathrm{i}}{\mathrm{k_{z1,m}-k_{z1,n}}}\right]+\frac{\mathrm{L}}{2}\mathrm{r}_{\mathbf{k}_\mathrm{m}}^{\mathrm{TEv}}\mathrm{r}_{\mathbf{k}_\mathrm{n}}^{\mathrm{TEv},*}\delta\left(\mathrm{k_{z1,m}-k_{z1,n}}\right), \tag{5.80}$$

where the delta terms for terms linear in the reflection coefficient are zero as all $k_{z1}>0$ by definition for modes incident from the vacuum halfspace. The lower halfspace term gives

$$\int \mathrm{dz}^{<}\mathrm{e}^{\mathrm{i(k_{z,m}-k_{z,n})z}}=\left(\mathcal{P}\left[\frac{-\mathrm{i}}{\mathrm{k_{z2,m}-k_{z2,n}}}\right]+\frac{\mathrm{L}}{2}\delta\left(\mathrm{k_{z2,m}-k_{z2,n}}\right)\right). \tag{5.81}$$

For the modes to be orthonormal with respect to the inner product Eq. 5.41 we need to prove that evaluation of the principal part gives zero. Collecting terms yields

$$0=(\omega_\mathrm{m}+\omega_\mathrm{n})\left[\mathcal{P}\left[\frac{\mathrm{i}}{\mathrm{k_{z1,m}-k_{z1,n}}}\right]+\mathrm{r}_{\mathbf{k}_\mathrm{m}}^{\mathrm{TEv}}\mathcal{P}\left[-\frac{\mathrm{i}}{\mathrm{k_{z1,m}+k_{z1,n}}}\right]+\mathrm{r}_{\mathbf{k}_\mathrm{n}}^{\mathrm{TEv},*}\mathcal{P}\left[\frac{\mathrm{i}}{\mathrm{k_{z1,m}+k_{z1,n}}}\right]\right. \tag{5.82}$$

$$\left.+\mathrm{r}_{\mathbf{k}_\mathrm{m}}^{\mathrm{TEv}}\mathrm{r}_{\mathbf{k}_\mathrm{n}}^{\mathrm{TEv},*}\mathcal{P}\left[-\frac{\mathrm{i}}{\mathrm{k_{z1,m}-k_{z1,n}}}\right]\right]+\frac{\epsilon(\omega_\mathrm{m})\omega_\mathrm{m}^2-\epsilon(\omega_\mathrm{n})\omega_\mathrm{n}^2}{\omega_\mathrm{m}-\omega_\mathrm{n}}\mathrm{t}_{\mathbf{k}_\mathrm{m}}^{\mathrm{TEv}}\mathrm{t}_{\mathbf{k}_\mathrm{n}}^{\mathrm{TEv},*}\mathcal{P}\left[\frac{-\mathrm{i}}{\mathrm{k_{z2,m}-k_{z2,n}}}\right], \tag{5.83}$$

and utilising

$$\frac{\epsilon(\omega_\mathrm{m})\omega_\mathrm{m}^2-\epsilon(\omega_\mathrm{n})\omega_\mathrm{n}^2}{\omega_\mathrm{m}-\omega_\mathrm{n}}=\frac{\mathrm{k_{z2,m}^2-k_{z2,n}^2}}{\mathrm{k_{z1,m}^2-k_{z1,n}^2}}\left(\omega_\mathrm{m}+\omega_\mathrm{n}\right), \tag{5.84}$$

along with the definition of the Fresnel coefficients Eq. 5.70 we can write

$$0=\frac{1}{\mathrm{k_{z1,m}-k_{z1,n}}}-\frac{\mathrm{k_{z1,m}-k_{z2,m}}}{\mathrm{k_{z1,m}+k_{z2,m}}}\frac{1}{\mathrm{k_{z1,m}+k_{z1,n}}}+\frac{\mathrm{k_{z1,n}-k_{z2,n}^*}}{\mathrm{k_{z1,n}+k_{z2,n}^*}}\frac{1}{\mathrm{k_{z1,m}+k_{z1,n}}} \tag{5.85}$$

$$-\frac{\mathrm{k_{z1,m}-k_{z2,m}}}{\mathrm{k_{z1,m}+k_{z2,m}}}\frac{\mathrm{k_{z1,n}-k_{z2,n}^*}}{\mathrm{k_{z1,n}+k_{z2,n}^*}}\frac{1}{\mathrm{k_{z1,m}-k_{z1,n}}}-\frac{\mathrm{k_{z2,m}^2-k_{z2,n}^2}}{\mathrm{k_{z1,m}^2-k_{z1,n}^2}}\frac{2\mathrm{k_{z1,m}}}{\mathrm{k_{z1,m}+k_{z2,m}}}\frac{2\mathrm{k_{z1,n}}}{\mathrm{k_{z1,n}+k_{z2,n}^*}}\frac{1}{\mathrm{k_{z2,m}-k_{z2,n}}}, \tag{5.86}$$

where we have removed the common factor $\omega_{\mathrm{m}}+\omega_{\mathrm{n}}$ and suppressed the principal part notation as it is common to all terms. Now multiplying the whole equation by $\left(\mathrm{k}_{\mathrm{z1,m}}^2-\mathrm{k}_{\mathrm{z1,n}}^2\right)\left(\mathrm{k}_{\mathrm{z1,m}}+\mathrm{k}_{\mathrm{z2,m}}\right)\left(\mathrm{k}_{\mathrm{z1,n}}+\mathrm{k}_{\mathrm{z2,n}}^*\right)$ and removing as a common factor we calculate

$$0=\left(k_{z1,\mathrm{m}}+k_{z1,\mathrm{n}}\right)\left(k_{z1,\mathrm{m}}+k_{z2,\mathrm{m}}\right)\left(k_{z1,\mathrm{n}}+k_{z2,\mathrm{n}}^*\right)-\left(k_{z1,\mathrm{m}}-k_{z2,\mathrm{m}}\right)\left(k_{z1,\mathrm{m}}-k_{z1,\mathrm{n}}\right)\left(k_{z1,\mathrm{n}}+k_{z2,\mathrm{n}}^*\right) \tag{5.87}$$

$$+\left(k_{z1,\mathrm{n}}-k_{z2,\mathrm{n}}^*\right)\left(k_{z1,\mathrm{m}}-k_{z1,\mathrm{n}}\right)\left(k_{z1,\mathrm{m}}+k_{z2,\mathrm{m}}\right)-\left(k_{z1,\mathrm{m}}-k_{z2,\mathrm{m}}\right)\left(k_{z1,\mathrm{n}}-k_{z2,\mathrm{n}}^*\right)\left(k_{z1,\mathrm{m}}+k_{z1,\mathrm{n}}\right) \tag{5.88}$$

$$-4k_{z1,\mathrm{m}}k_{z1,\mathrm{n}}\left(k_{z2,\mathrm{m}}+k_{z2,\mathrm{n}}\right), \tag{5.89}$$

which is the case. The remaining terms in Eq. 5.74 may be expressed as

$$\frac{2\delta_{\mathrm{m,n}}}{\epsilon_0\mathrm{L}^3|\mathrm{N}_{\mathbf{k}}^{\mathrm{TEv}}|^2\delta\left(\mathbf{k}_{\parallel,\mathrm{m}}-\mathbf{k}_{\parallel,\mathrm{n}}\right)}=\left(\omega_{\mathrm{m}}+\omega_{\mathrm{n}}\right)\left(1+\mathrm{r}_{\mathbf{k}_{\mathrm{m}}}^{\mathrm{TEv}}\mathrm{r}_{\mathbf{k}_{\mathrm{n}}}^{\mathrm{TEv},*}\right)\delta\left(\mathrm{k}_{\mathrm{z1,m}}-\mathrm{k}_{\mathrm{z1,n}}\right) \tag{5.90}$$

$$+\frac{\epsilon(\omega_{\mathrm{m}})\omega_{\mathrm{m}}^2-\epsilon(\omega_{\mathrm{n}})\omega_{\mathrm{n}}^2}{\omega_{\mathrm{m}}-\omega_{\mathrm{n}}}\mathrm{t}_{\mathbf{k}_{\mathrm{m}}}^{\mathrm{TEv}}\mathrm{t}_{\mathbf{k}_{\mathrm{n}}}^{\mathrm{TEv},*}\delta\left(\mathrm{k}_{\mathrm{z2,m}}-\mathrm{k}_{\mathrm{z2,n}}\right), \tag{5.91}$$

and utilising the equations

$$\delta\left(\mathrm{k}_{2\mathrm{z}}-\mathrm{k}_{2\mathrm{z}}'\right)=\delta\left(\mathrm{k}_{1\mathrm{z}}-\mathrm{k}_{1\mathrm{z}}'\right)\frac{\mathrm{k}_{2\mathrm{z}}}{\mathrm{k}_{1\mathrm{z}}}\frac{1}{\epsilon\left(\omega\right)+\frac{\omega}{2}\frac{\partial\epsilon(\omega)}{\partial\omega}}, \tag{5.92}$$

$$\lim_{\omega_{\mathrm{n}},\omega_{\mathrm{m}}\to\omega}\frac{\epsilon(\omega_{\mathrm{m}})\omega_{\mathrm{m}}^2-\epsilon(\omega_{\mathrm{n}})\omega_{\mathrm{n}}^2}{\omega_{\mathrm{m}}-\omega_{\mathrm{n}}}=2\omega\left(\epsilon\left(\omega\right)+\frac{\omega}{2}\frac{\partial\epsilon\left(\omega\right)}{\partial\omega}\right), \tag{5.93}$$

we can express Eq. 5.91 as

$$\frac{2\delta_{\mathrm{m,n}}}{2\mathrm{L}^3|\mathrm{N}_{\mathbf{k}}^{\mathrm{TE}}|^2\delta\left(\mathbf{k}_{\parallel,m}-\mathbf{k}_{\parallel,n}\right)\omega}=\left(1+|r_{\mathbf{k}}^{\mathrm{TE}}|^2+\frac{k_{2z}}{k_{1z}}|t_{\mathbf{k}}^{\mathrm{TE}}|^2\right)\delta\left(k_{z1,\mathrm{m}}-k_{z1,\mathrm{n}}\right), \tag{5.94}$$

and finally we apply the definition of the Fresnel coefficients Eq. 5.70 to find

$$1+|\mathrm{r}_{\mathbf{k}}^{\mathrm{TE}}|^2+\frac{\mathrm{k}_{2\mathrm{z}}}{\mathrm{k}_{1\mathrm{z}}}|\mathrm{t}_{\mathbf{k}}^{\mathrm{TE}}|^2=1+|\frac{\mathrm{k}_{\mathrm{z1}}-\mathrm{k}_{\mathrm{z2}}}{\mathrm{k}_{\mathrm{z1}}+\mathrm{k}_{\mathrm{z2}}}|^2+\frac{\mathrm{k}_{2\mathrm{z}}}{\mathrm{k}_{1\mathrm{z}}}|\frac{2\mathrm{k}_{\mathrm{z1}}}{\mathrm{k}_{\mathrm{z1}}+\mathrm{k}_{\mathrm{z2}}}|^2=2, \tag{5.95}$$

so we can write

$$\delta_{\mathrm{m,n}}=2\omega\mathrm{V}|\mathrm{N}_{\mathbf{k}}^{\mathrm{TEv}}|^2\delta^3\left(\mathbf{k}_{\mathrm{m}}-\mathbf{k}_{\mathrm{n}}\right), \tag{5.96}$$

so we find that

$$\mathrm{N}_{\mathbf{k}}^{\mathrm{TEv}}=\sqrt{\frac{1}{2\epsilon_0\omega\mathrm{V}}}, \tag{5.97}$$

where V is the quantisation volume.

TM Modes Incident from Vacuum

For TM polarisation we express the modes in terms of the magnetic Hopfield coefficient $\boldsymbol{\beta}$ as

$$\begin{aligned}\boldsymbol{\beta}_{\mathbf{k}}^{\mathrm{TMv}}(\mathbf{r}_{\parallel},\mathrm{z}{>}0)&=\mathrm{N}_{\mathbf{k}}^{\mathrm{TMv}}\mathrm{e}^{-\mathrm{i}\mathbf{k}_{\parallel}\cdot\mathbf{r}_{\parallel}}\left(\mathrm{e}^{\mathrm{i}\mathrm{k}_{\mathrm{z}}\mathrm{z}}+\mathrm{r}_{\mathbf{k}}^{\mathrm{TMv}}\mathrm{e}^{-\mathrm{i}\mathrm{k}_{\mathrm{z}}\mathrm{z}}\right)\hat{\mathbf{e}}_{\perp},\\ \boldsymbol{\beta}_{\mathbf{k}}^{\mathrm{TMv}}(\mathbf{r}_{\parallel},\mathrm{z}{<}0)&=\mathrm{N}_{\mathbf{k}}^{\mathrm{TMv}}\mathrm{t}_{\mathbf{k}}^{\mathrm{TMv}}\mathrm{e}^{-\mathrm{i}\mathbf{k}\cdot\mathbf{r}_{\parallel}}\hat{\mathbf{e}}_{\perp},\end{aligned}\tag{5.98}$$

where the $r_{\mathbf{k}}^{\mathrm{TMv}}, t_{\mathbf{k}}^{\mathrm{TMv}}$ are the usual Fresnel coefficients for TM polarised light. The corresponding $\boldsymbol{\theta}$ is simply calculated through

$$\boldsymbol{\theta}=-\frac{i\mathrm{c}^2}{\omega\epsilon\left(\omega\right)}\nabla\times\boldsymbol{\beta},\tag{5.99}$$

and by use of Eq. 5.41 we can follow the prescription of Sec. 5.3 to find

$$\mathrm{N}_{\mathbf{k}}^{\mathrm{TMv}}=\sqrt{\frac{\mu_0}{2\omega\mathrm{V}}}.\tag{5.100}$$

TE Modes Incident from the Dielectric

The TE polarised modes propagating from the polar dielectric consist of two polariton branches labelled ± The modes are given by

$$\begin{aligned}\boldsymbol{\theta}_{\mathbf{k}}^{\mathrm{TE}\pm}(\mathbf{r}_{\parallel},\mathrm{z}{>}0)&=\mathrm{N}_{\mathbf{k}}^{\mathrm{TE}\pm}\mathrm{t}_{\mathbf{k}}^{\mathrm{TE}\pm}\mathrm{e}^{-\mathrm{i}\mathbf{k}\cdot\mathbf{r}}\hat{\mathbf{e}}_{\perp},\\ \boldsymbol{\theta}_{\mathbf{k}}^{\mathrm{TE}\pm}(\mathbf{r}_{\parallel},\mathrm{z}{<}0)&=\mathrm{N}_{\mathbf{k}}^{\mathrm{TE}\pm}\mathrm{e}^{-\mathrm{i}\mathbf{k}_{\parallel}\cdot\mathbf{r}_{\parallel}}\left(\mathrm{e}^{-\mathrm{i}\mathrm{k}_{\mathrm{z}}\mathrm{z}}+\mathrm{r}_{\mathbf{k}}^{\mathrm{TE}\pm}\mathrm{e}^{\mathrm{i}\mathrm{k}_{\mathrm{z}}\mathrm{z}}\right)\hat{\mathbf{e}}_{\perp},\end{aligned}\tag{5.101}$$

where the $r_{\mathbf{k}}^{\mathrm{TE}\pm}, t_{\mathbf{k}}^{\mathrm{TE}\pm}$ are the usual Fresnel coefficients for TE polarised light. On following the procedure of Sec. 5.3 the normalisation constant is calculated as

$$\mathrm{N}_{\mathbf{k}}^{\mathrm{TE}\pm}=\sqrt{\frac{1}{2\omega\nu\left(\omega_{\mathbf{k},\pm}\right)\mathrm{V}}},\tag{5.102}$$

where the function $\nu\left(\omega\right)$ is defined in Eq. 5.44.

TM Modes Incident from the Dielectric

The TM polarised modes propagating from the polar dielectric also consist of two polariton branches labelled $\pm$. The modes are given by

$$\begin{aligned}\boldsymbol{\beta}_{\mathbf{k}}^{\mathrm{TM}\pm}(\mathbf{r}_{\parallel},\mathrm{z}{>}0)&=\mathrm{N}_{\mathbf{k}}^{\mathrm{TM}\pm}\mathrm{t}_{\mathbf{k}}^{\mathrm{TM}\pm}\mathrm{e}^{-\mathrm{i}\mathbf{k}\cdot\mathbf{r}}\hat{\mathbf{e}}_{\perp},\\ \boldsymbol{\beta}_{\mathbf{k}}^{\mathrm{TM}\pm}(\mathbf{r}_{\parallel},\mathrm{z}{<}0)&=\mathrm{N}_{\mathbf{k}}^{\mathrm{TM}\pm}\mathrm{e}^{-\mathrm{i}\mathbf{k}_{\parallel}\cdot\mathbf{r}_{\parallel}}\left(\mathrm{e}^{-\mathrm{i}\mathrm{k}_{\mathrm{z}}\mathrm{z}}+\mathrm{r}_{\mathbf{k}}^{\mathrm{TM}\pm}\mathrm{e}^{\mathrm{i}\mathrm{k}_{\mathrm{z}}\mathrm{z}}\right)\hat{\mathbf{e}}_{\perp},\end{aligned}\tag{5.103}$$

where the $r_{\mathbf{k}}^{\mathrm{TM}\pm}, t_{\mathbf{k}}^{\mathrm{TM}\pm}$ are the usual Fresnel coefficients for TM polarised light. The normalisation constant is found to be

$$\mathrm{N}_{\mathbf{k}}^{\mathrm{TM}\pm}=\sqrt{\frac{\mu_0}{2\omega\nu\left(\omega_{\mathbf{k},\pm}\right)\mathrm{V}}}.\tag{5.104}$$

Evanescent Modes

Surface modes are naturally characterised in terms of the magnetic field coefficient as

$$\begin{aligned}\boldsymbol{\beta}_{\mathbf{k}_{\parallel}}^{\mathrm{S}}(\mathbf{r}_{\parallel},z{>}0)&=\mathrm{N}_{\mathbf{k}_{\parallel}}^{\mathrm{S}}\mathrm{e}^{-\mathrm{i}\mathbf{k}_{\parallel}\cdot\mathbf{r}_{\parallel}}\mathrm{e}^{-|\mathrm{k}_{\parallel}|\sqrt{\frac{-1}{\epsilon(\omega)}}\mathrm{z}}\hat{\mathbf{e}}_{\perp},\\ \boldsymbol{\beta}_{\mathbf{k}_{\parallel}}^{\mathrm{S}}(\mathbf{r}_{\parallel},z{>}0)&=\mathrm{N}_{\mathbf{k}_{\parallel}}^{\mathrm{S}}\mathrm{e}^{-\mathrm{i}\mathbf{k}_{\parallel}\cdot\mathbf{r}_{\parallel}}\mathrm{e}^{|\mathrm{k}_{\parallel}|\sqrt{-\epsilon(\omega)}\mathrm{z}}\hat{\mathbf{e}}_{\perp},\end{aligned}\tag{5.105}$$

where the out-of-plane wavevector component has been explicitly calculated. This corresponds to electric field coefficient

$$\boldsymbol{\theta}_{\mathbf{k}_{\parallel}}^{\mathrm{S}}(\mathbf{r}_{\parallel},\mathrm{z}{>}0)=-\frac{\mathrm{c}^2\mathrm{N}_{\mathbf{k}_{\parallel}}^{\mathrm{S}}}{\omega}\left[\mathrm{i}\mathrm{k}_{\parallel}\sqrt{\frac{-1}{\epsilon\left(\omega\right)}}\hat{\mathbf{e}}_{\parallel}+\mathrm{k}_{\parallel}\hat{\mathbf{e}}_{\mathrm{z}}\right]\mathrm{e}^{-\mathrm{i}\mathbf{k}_{\parallel}\cdot\mathbf{r}_{\parallel}}\mathrm{e}^{-|\mathrm{k}_{\parallel}|\sqrt{\frac{-1}{\epsilon(\omega)}}\mathrm{z}},\tag{5.106}$$

$$\boldsymbol{\theta}_{\mathbf{k}_{\parallel}}^{\mathrm{S}}(\mathbf{r}_{\parallel},\mathrm{z}{<}0)=\frac{\mathrm{c}^2\mathrm{N}_{\mathbf{k}_{\parallel}}^{\mathrm{S}}}{\omega\epsilon\left(\omega\right)}\left[\mathrm{i}\mathrm{k}_{\parallel}\sqrt{-\epsilon\left(\omega\right)}\hat{\mathbf{e}}_{\parallel}-\mathrm{k}_{\parallel}\hat{\mathbf{e}}_{\mathrm{z}}\right]\mathrm{e}^{-\mathrm{i}\mathbf{k}_{\parallel}\cdot\mathbf{r}_{\parallel}}\mathrm{e}^{|\mathrm{k}_{\parallel}|\sqrt{-\epsilon(\omega)}\mathrm{z}}.\tag{5.107}$$

$$\tag{5.108}$$

Now we normalise utilising Eq. 5.41. The in-plane integral is carried out as in Sec. 5.3 and the integral over z is split giving

$$\delta_{\mathrm{m,n}}=\frac{\epsilon_0\mathrm{c}^4\mathrm{k}_{\parallel}^2|\mathrm{N}_{\mathbf{k}_{\parallel}}^{\mathrm{S}}|^2}{\omega^2}\mathrm{L}^2\delta\left(\mathbf{k}_{\parallel,\mathrm{m}}-\mathbf{k}_{\parallel,\mathrm{n}}\right)\left[2\omega\int\mathrm{d}\mathrm{z}^{>}\left(1-\frac{1}{\epsilon\left(\omega\right)}\right)\mathrm{e}^{-2|\mathrm{k}_{\parallel}|\sqrt{\frac{-1}{\epsilon(\omega)}}\mathrm{z}}\right.\tag{5.109}$$

$$\left.+\frac{2\omega\nu\left(\omega\right)}{\epsilon\left(\omega\right)}\int\mathrm{d}\mathrm{z}^{>}\left(1-\epsilon\left(\omega\right)\right)\mathrm{e}^{2|\mathrm{k}_{\parallel}|\sqrt{-\epsilon(\omega)}\mathrm{z}}\right].\tag{5.110}$$

Now we apply the evanescent mode dispersion relation

$$\mathrm{k}_{\parallel}=\frac{\omega}{\mathrm{c}}\sqrt{\frac{\epsilon\left(\omega\right)}{1+\epsilon\left(\omega\right)}}, \tag{5.111}$$

and carry out the out-of-plane integral to find

$$\delta_{\mathrm{m,n}}=2\omega\epsilon_0\mathrm{c}^2|\mathrm{N}^{\mathrm{S}}_{\mathbf{k}_{\parallel}}|^2\mathrm{L}^2\frac{\epsilon\left(\omega\right)}{1+\epsilon\left(\omega\right)}\delta\left(\mathbf{k}_{\parallel,\mathrm{m}}-\mathbf{k}_{\parallel,\mathrm{n}}\right)\left(\sqrt{-\epsilon\left(\omega\right)}+\frac{1}{\sqrt{-\epsilon\left(\omega\right)}}\right)\frac{1}{2|\mathrm{k}_{\parallel}|}\left[1-\frac{\nu\left(\omega\right)}{\epsilon\left(\omega\right)}\right], \tag{5.112}$$

finally yielding the normalisation coefficient

$$\mathrm{N}^{\mathrm{S}}_{\mathbf{k}_{\parallel}}=\sqrt{\frac{\mu_0}{\omega\mathrm{L}^2}}\sqrt{\frac{|\mathrm{k}_{\parallel}|}{\left(\sqrt{-\epsilon\left(\omega\right)}+\frac{1}{\sqrt{-\epsilon(\omega)}}\right)\left(1-\frac{\nu(\omega)}{\epsilon(\omega)}\right)}}\sqrt{\frac{1+\epsilon\left(\omega\right)}{\epsilon\left(\omega\right)}}. \tag{5.113}$$

Completeness

The form of the completeness in terms of the Hopfield coefficients is given by

$$\begin{aligned}\sum_{\mathbf{k}^{\sigma}}\sum_{\sigma}&\left[\boldsymbol{\alpha}^{\sigma}_{\mathbf{k}^{\sigma}}\left(\mathbf{r}'\right)\cdot\nabla\times\bar{\boldsymbol{\beta}}^{\sigma}_{\mathbf{k}^{\sigma}}\left(\mathbf{r}\right)-\bar{\boldsymbol{\alpha}}^{\sigma}_{\mathbf{k}^{\sigma}}\left(\mathbf{r}'\right)\cdot\nabla\times\boldsymbol{\beta}^{\sigma}_{\mathbf{k}^{\sigma}}\left(\mathbf{r}\right)\right]\\&=\frac{i}{\mathrm{c}^2}\sum_{\mathbf{k}_{\sigma}}\sum_{\sigma}\omega^{\sigma}_{\mathbf{k}^{\sigma}}[\epsilon\left(\omega^{\sigma}_{\mathbf{k}^{\sigma}},\mathbf{r}'\right)\boldsymbol{\alpha}^{\sigma}_{\mathbf{k}^{\sigma}}\left(\mathbf{r}'\right)\cdot\bar{\boldsymbol{\alpha}}^{\sigma}_{\mathbf{k}^{\sigma}}\left(\mathbf{r}\right)+\epsilon\left(\omega^{\sigma}_{\mathbf{k}^{\sigma}},\mathbf{r}\right)\bar{\boldsymbol{\alpha}}^{\sigma}_{\mathbf{k}^{\sigma}}\left(\mathbf{r}'\right)\cdot\boldsymbol{\alpha}^{\sigma}_{\mathbf{k}^{\sigma}}\left(\mathbf{r}\right)],\end{aligned}$$

and we evaluate this in the upper halfspace $\mathrm{z},\mathrm{z}'>0$ for brevity. The result for the lower halfspace may be calculated by application of the same methods and utilisation of the velocity sum rule calculated by Huttner and Barnett [160]

$$\sum_{\pm}\frac{\mathrm{v}^{\mathrm{G}}\left(\omega_{\mathbf{k},\pm}\right)}{\mathrm{v}^{\mathrm{P}}\left(\omega_{\mathbf{k},\pm}\right)}=1, \tag{5.114}$$

which links the velocities of the upper and lower polariton branches.
The contribution from TE polarised propagating modes in the upper halfspace is given

by

$$\frac{i}{\mathrm{c}^2}\sum_{\mathbf{k}_\sigma}\sum_{\sigma=\mathrm{TEv,TE}\pm}\omega^\sigma_{\mathbf{k}^\sigma}\left[\epsilon\left(\omega^\sigma_{\mathbf{k}^\sigma},\mathbf{r}'\right)\boldsymbol{\alpha}^\sigma_{\mathbf{k}^\sigma}\left(\mathbf{r}'\right)\cdot\bar{\boldsymbol{\alpha}}^\sigma_{\mathbf{k}^\sigma}\left(\mathbf{r}\right)+\epsilon\left(\omega^\sigma_{\mathbf{k}^\sigma},\mathbf{r}\right)\bar{\boldsymbol{\alpha}}^\sigma_{\mathbf{k}^\sigma}\left(\mathbf{r}'\right)\cdot\boldsymbol{\alpha}^\sigma_{\mathbf{k}^\sigma}\left(\mathbf{r}\right)\right], \tag{5.115}$$

$$=\frac{i\mu_0}{2}\int\mathrm{dk_z}\int\mathrm{d}\mathbf{k}_\parallel\left[\mathrm{e}^{\mathrm{i}\mathbf{k}_\parallel\cdot\left(\mathbf{r}-\mathbf{r}'\right)}\mathrm{e}^{\mathrm{ik_z(z-z')}}\left(1+|\mathrm{r}^{\mathrm{TEv}}_{\mathbf{k}}|^2+\frac{\mathrm{k_z}}{\mathrm{k_{zd}}}|\mathrm{t}^{\mathrm{TE}\pm}_{\mathbf{k}}|^2\right)+\mathrm{C.C}\right], \tag{5.116}$$

$$=i\mu_0\boldsymbol{\delta}^{\mathrm{T}}\left(\mathbf{r}-\mathbf{r}'\right), \tag{5.117}$$

For the TM modes in the upper halfspace we find

$$\frac{i}{\mathrm{c}^2}\sum_{\mathbf{k}_\sigma}\sum_{\sigma=\mathrm{TMv,TM}\pm}\omega^\sigma_{\mathbf{k}^\sigma}\left[\epsilon\left(\omega^\sigma_{\mathbf{k}^\sigma},\mathbf{r}'\right)\boldsymbol{\alpha}^\sigma_{\mathbf{k}^\sigma}\left(\mathbf{r}'\right)\cdot\bar{\boldsymbol{\alpha}}^\sigma_{\mathbf{k}^\sigma}\left(\mathbf{r}\right)+\epsilon\left(\omega^\sigma_{\mathbf{k}^\sigma},\mathbf{r}\right)\bar{\boldsymbol{\alpha}}^\sigma_{\mathbf{k}^\sigma}\left(\mathbf{r}'\right)\cdot\boldsymbol{\alpha}^\sigma_{\mathbf{k}^\sigma}\left(\mathbf{r}\right)\right], \tag{5.118}$$

$$=\frac{i\mu_0}{2}\sum_{\pm}\Bigg(\int\mathrm{dk_z}\int\mathrm{d}\mathbf{k}_\parallel\left[\mathrm{e}^{\mathrm{i}\mathbf{k}_\parallel\cdot\left(\mathbf{r}-\mathbf{r}'\right)}\mathrm{e}^{\mathrm{ik_z(z-z')}}\left(1+|\mathrm{r}^{\mathrm{TMv}}_{\mathbf{k}}|^2+\frac{\mathrm{k_z}\epsilon\left(\omega_{\mathbf{k}}\right)}{\mathrm{k_{zd}}}|\mathrm{t}^{\mathrm{TM}\pm}_{\mathbf{k}}|^2\right)+\mathrm{C.C}\right] \tag{5.119}$$

$$+2\int\mathrm{dk_z}\int\mathrm{d}\mathbf{k}_\parallel\mathrm{e}^{\mathrm{i}\mathbf{k}_\parallel\cdot\left(\mathbf{r}-\mathbf{r}'\right)}\frac{\mathrm{c}^2\left(|\mathrm{k}_\parallel|^2-|\mathrm{k_z}|^2\right)}{\omega^2}\left[\mathrm{r}^{\mathrm{TMv}}_{\mathbf{k}}\mathrm{e}^{-\mathrm{ik_z(z+z')}}+\mathrm{r}^{\mathrm{TMv*}}_{\mathbf{k}}\mathrm{e}^{\mathrm{ik_z(z+z')}}\right]\Bigg), \tag{5.120}$$

$$=i\mu_0\boldsymbol{\delta}^{\mathrm{T}}\left(\mathbf{r}-\mathbf{r}'\right)+i\mu_0\int\mathrm{dk_z}\int\mathrm{d}\mathbf{k}_\parallel\mathrm{e}^{\mathrm{i}\mathbf{k}_\parallel\cdot\left(\mathbf{r}-\mathbf{r}'\right)}\frac{\mathrm{c}^2\left(|\mathrm{k}_\parallel|^2-|\mathrm{k_z}|^2\right)}{\omega^2}\left[\mathrm{r}^{\mathrm{TMv}}_{\mathbf{k}}\mathrm{e}^{-\mathrm{ik_z(z+z')}}+\mathrm{r}^{\mathrm{TMv*}}_{\mathbf{k}}\mathrm{e}^{\mathrm{ik_z(z+z')}}\right], \tag{5.121}$$

$$=i\mu_0\boldsymbol{\delta}^{\mathrm{T}}\left(\mathbf{r}-\mathbf{r}'\right)+\mathcal{F}\left(\mathbf{r},\mathbf{r}',\omega\right), \tag{5.122}$$

where the remaining integral $\mathcal{F}\left(\mathbf{r},\mathbf{r}',\omega\right)$ will give the contribution of the pole of the Fresnel coefficients located at $\mathrm{k_z}=-\mathrm{k_{zd}}/\epsilon\left(\omega_{\mathbf{k}}\right)$. This is the evanescent mode so we can immediately write the pole position in frequency space as

$$\omega^2_{\mathrm{pole}}=\frac{2\mathrm{c}^2\mathrm{k}^2_\parallel+\omega^2_{\mathrm{L}}-\sqrt{4\mathrm{c}^4\mathrm{k}^4_\parallel+\omega^4_{\mathrm{L}}-4\mathrm{c}^2\mathrm{k}^2_\parallel\omega^2_{\mathrm{T}}}}{2}, \tag{5.123}$$

$$\mathrm{c}^2\mathrm{k}^2_{\mathrm{z,pole}}=\frac{\omega^2_{\mathrm{L}}-\sqrt{4\mathrm{c}^4\mathrm{k}^4_\parallel+\omega^2_{\mathrm{L}}-4\mathrm{c}^2\mathrm{k}^2_\parallel\omega^2_{\mathrm{T}}}}{2}, \tag{5.124}$$

and by making a first order Taylor expansion of the denominator of the reflection coefficient around the pole we can write the residue at the pole as

$$\lim_{\mathrm{k_z}\to\mathrm{k_{z,pole}}}\left(\mathrm{k_z}-\mathrm{k_{z,pole}}\right)\mathrm{r}^{\mathrm{TMv}}_{\mathbf{k}}=\frac{1}{1-\epsilon\left(\omega\right)}\frac{\sqrt{-\epsilon\left(\omega\right)}\mathrm{k}_\parallel}{1+\frac{\omega}{2\epsilon(\omega)(1-\epsilon(\omega))}\frac{\partial\epsilon(\omega)}{\partial\omega}}, \tag{5.125}$$

and in addition we may recognise that with an imaginary $\mathrm{k_z}$ the prefactor at the pole is unity

$$\lim_{\mathrm{k_z}\to\mathrm{k_{z,pole}}}\frac{\mathrm{c}^2\left(|\mathrm{k}_\parallel|^2-|\mathrm{k_z}|^2\right)}{\omega^2}=1, \tag{5.126}$$

as the wavevector sum is just the Helmholtz dispersion for the evanescent wave in the upper halfspace. We can therefore write the integrand as

$$\mathcal{F}\left(\mathbf{r},\mathbf{r}',\omega\right)=-i\mu_0\int \mathrm{d}\mathbf{k}_\parallel e^{i\mathbf{k}_\parallel\cdot\left(\mathbf{r}-\mathbf{r}'\right)}\frac{\sqrt{-\epsilon\left(\omega\right)}\mathrm{k}_\parallel}{1-\epsilon\left(\omega\right)+\frac{\omega}{2\epsilon(\omega)}\frac{\partial\epsilon(\omega)}{\partial\omega}}\mathrm{e}^{-\frac{|\mathrm{k}_\parallel|}{\sqrt{-\epsilon(\omega)}}\left(\mathrm{z}+\mathrm{z}'\right)}+\mathrm{C.C.}. \tag{5.127}$$

Now it is left to calculate the contribution from the surface mode. This is given by

$$\frac{i}{\mathrm{c}^2}\sum_{\mathbf{k}_\mathrm{S}}\omega^{\mathrm{S}}_{\mathbf{k}^{\mathrm{S}}}[\epsilon\left(\omega^{\mathrm{S}}_{\mathbf{k}^{\mathrm{S}}},\mathbf{r}'\right)\boldsymbol{\alpha}^{\mathrm{S}}_{\mathbf{k}^{\mathrm{S}}}\left(\mathbf{r}'\right)\cdot\bar{\boldsymbol{\alpha}}^{\mathrm{S}}_{\mathbf{k}^{\mathrm{S}}}\left(\mathbf{r}\right)+\epsilon\left(\omega^{\mathrm{S}}_{\mathbf{k}^{\mathrm{S}}},\mathbf{r}\right)\bar{\boldsymbol{\alpha}}^{\mathrm{S}}_{\mathbf{k}^{\mathrm{S}}}\left(\mathbf{r}'\right)\cdot\boldsymbol{\alpha}^{\mathrm{S}}_{\mathbf{k}^{\mathrm{S}}}\left(\mathbf{r}\right)], \tag{5.128}$$

$$=i\int \mathrm{d}\mathbf{k}_\parallel\omega|\mathrm{N}^{\mathrm{S}}_{\mathbf{k}_\parallel}|^2\mathrm{e}^{\mathrm{i}\mathbf{k}_\parallel\cdot\left(\mathbf{r}-\mathbf{r}'\right)}\frac{\epsilon\left(\omega\right)}{\epsilon\left(\omega\right)+1}\left(1-\frac{1}{\epsilon\left(\omega\right)}\right)\mathrm{e}^{-\frac{|\mathbf{k}_\parallel|}{\sqrt{-\epsilon(\omega)}}\left(\mathrm{z}+\mathrm{z}'\right)}+\mathrm{C.C.}, \tag{5.129}$$

$$=i\mu_0\int \mathrm{d}\mathbf{k}_\parallel\mathrm{e}^{\mathrm{i}\mathbf{k}_\parallel\cdot\left(\mathbf{r}-\mathbf{r}'\right)}\frac{|\mathrm{k}_\parallel|\sqrt{-\epsilon\left(\omega\right)}}{1-\epsilon\left(\omega\right)+\frac{\omega}{2\epsilon(\omega)}\frac{\partial\epsilon(\omega)}{\partial\omega}}\mathrm{e}^{-\frac{|\mathbf{k}_\parallel|}{\sqrt{-\epsilon(\omega)}}\left(\mathrm{z}+\mathrm{z}'\right)}+\mathrm{C.C.}, \tag{5.130}$$

so the system is orthonormal and complete.

5.4 Field Quantisation in Dispersive, Dissipative Media

So far we have considered the problem of electromagnetic field quantisation in dielectrics with an arbitrarily dispersive dielectric function in the absence of loss. This situation is non-physical, physical systems always involve dissipation, the real part of the electric susceptibility being related to the imaginary by the Kramers-Kronig relations

$$\chi_{\mathrm{R}}\left(\omega_0\right)=\frac{1}{\pi}\mathcal{P}\left[\int_{-\infty}^{\infty}\frac{\chi_{\mathrm{I}}\left(\omega\right)}{\omega-\omega_0}\mathrm{d}\omega\right], \tag{5.131}$$

$$\chi_{\mathrm{I}}\left(\omega_0\right)=-\frac{1}{\pi}\mathcal{P}\left[\int_{-\infty}^{\infty}\frac{\chi_{\mathrm{R}}\left(\omega\right)}{\omega-\omega_0}\mathrm{d}\omega\right], \tag{5.132}$$

which mean that resonant dispersion of the dielectric function at some real frequency will always result in loss at some other frequency. Attempts to quantise the electromagnetic field in these lossy systems fall into two main strands. The first set are microscopic

and proceed by writing the Hamiltonian for the light-matter coupled system as in Sec. 5.2 with dissipation described by coupling the matter fields to a non-resonant oscillator bath. Such a model may be solved by a Fano diagonalisation procedure [174]. Similar results are derivable in a fully microscopic framework that accounts for the lattice and dipole-dipole Coulomb interactions, in this case the Heisenberg equations for the operators were derived [175]. The Huttner-Barnett model can be easily extended to describe transient effects [176]. Extending the results of Huttner-Barnett to the inhomogeneous case is problematic as the modal expansions rely upon separation of longitudinal and transverse variables, this was later achieved by Suttorp who utilise a Fano diagonalisation procedure to derive equations of motion for the Hopfield coefficients, eventually expressing the fields in terms of the Green function of the classical scattering problem [177]. Equivalent results may also be derived utilising a Laplace transform technique [178]. Microscopic models may be extended to describe spatio-temporal dispersion of the dielectric function [179] and magnetodielectric materials [180]. The second set of procedures are macroscopic and build on the microscopic results of Huttner and Barnett for the isotropic dissipative dielectric system. Huttner and Barnett find that the medium can be solely described by its complex, dispersive dielectric function and can therefore be extended from the microscopic harmonic oscillator model of a dielectric to obtain a general procedure for field quantisation in dispersive and absorptive systems with phenomenologically given, Kramers-Kronig consistent, dielectric functions [181]. This approach may be extended by the introduction of phenomenological operatorial noise currents in the Maxwell equations as derived from the full Hopfield model by Knöll [182]. These act to preserve the equal time commutation relations between the fields. In this way it is possible to write the fields in terms of the Green's function of the classical scattering problem allowing for quantisation of the electromagnetic field in spatially inhomogeneous systems as postulated by both Gruner and Welsch [170] and Loudon *et al.* [183, 184]. This was later confirmed rigorously by the microscopic method of Suttorp [177]. Alternatively this approach may be developed from the causal relation between the electric and polarisation fields, in this case auxiliary fields are introduced to ensure unitary time evolution of the system [185, 186]. The Green function approach is easily extended to the three-dimensional case and its consistency proved for the homogeneous case [187], for a planar inhomogeneity [188] and for the case of general inhomogeneity [189]. These models can also describe spatial dispersion [190, 191] and magneto-dielectric materials [192]. We follow the approach of Huttner and Barnett's original extension to the dissipative case [174] and describe our lossy dielectric by

coupling the matter fields to a non-resonant oscillator bath. The Lagrangian for this system is given by $\mathcal{L}=\mathcal{L}_0'+\mathcal{L}_\mathrm{b}$ where $\mathcal{L}_0'$ is the Lagrangian derived in Eq. 5.17 for the non-dissipative case and

$$\mathcal{L}_\mathrm{B}=\int_0^\infty \mathrm{d}\zeta \left[\frac{\rho\dot{\mathrm{Y}}_\zeta^2}{2}-\frac{\rho\zeta^2\mathrm{Y}_\zeta^2}{2}-\upsilon_\zeta\mathbf{X}\cdot\dot{\mathbf{Y}}_\zeta\right], \tag{5.133}$$

describes a bath with displacement $\mathbf{Y}_\zeta$ and frequency ζ that couples to the matter modes with frequency υ_ζ. It is assumed that the integrals over the bath exist only when $\rho\neq 0$. The canonical momenta for the oscillator bath $\mathbf{Q}_\zeta$ is given by

$$\mathbf{Q}_\zeta=\frac{\delta\mathcal{L}_\mathrm{B}}{\delta\dot{\mathbf{Y}}_\zeta}=\rho\dot{\mathbf{Y}}_\zeta-\upsilon_\zeta\mathbf{X}, \tag{5.134}$$

and utilising this we can find the Hamiltonian density for the full system as $\mathcal{H}=\mathcal{H}_0+\mathcal{H}_\mathrm{B}$ where $\mathcal{H}_0$ is given in Eq. 5.19 and

$$\mathcal{H}_\mathrm{B}=\int_0^\infty \mathrm{d}\zeta \left[\frac{\rho\zeta^2\mathrm{Y}_\zeta^2}{2}+\frac{\mathrm{Q}_\zeta^2}{2\rho}+\frac{\upsilon_\zeta}{\rho}\mathbf{Q}_\zeta\cdot\mathbf{X}+\frac{\upsilon_\zeta^2\mathrm{X}^2}{2\rho}\right], \tag{5.135}$$

where the final term quadratic in the matter displacement X describes the renormalisation of the longitudinal frequency ω_L as a result of coupling to the bath

$$\tilde{\omega}_\mathrm{L}^2=\omega_\mathrm{T}^2+\frac{\kappa^2}{\epsilon_0\rho}+\int_0^\infty \mathrm{d}\zeta\,\frac{\upsilon_\zeta^2}{2\rho^2}. \tag{5.136}$$

We quantise the full Hamiltonian $\mathcal{H}$ by imposing the non-zero commutation relations Eq. 5.21-5.23 in addition to

$$\left[\mathbf{Y}_\zeta\left(\mathbf{r}\right),\mathbf{Q}_{\zeta'}\left(\mathbf{r}'\right)\right]=i\hbar\boldsymbol{\delta}\left(\mathbf{r}-\mathbf{r}'\right)\delta\left(\zeta-\zeta'\right), \tag{5.137}$$

which is the commutation relation of the bath variables. Now we introduce the polariton operator of the coupled system as

$$\mathcal{K}=\int \mathrm{d}\mathbf{r}\left[\boldsymbol{\alpha}\cdot\mathbf{D}+\boldsymbol{\beta}\cdot\mathbf{H}+\boldsymbol{\gamma}\cdot\mathbf{P}+\boldsymbol{\eta}\cdot\mathbf{X}+\int_0^\infty \mathrm{d}\zeta\left(\boldsymbol{\chi}_\zeta\cdot\mathbf{Q}_\zeta+\boldsymbol{\xi}_\zeta\cdot\mathbf{Y}_\zeta\right)\right], \tag{5.138}$$

and as before we solve the Heisenberg equation

$$\left[\mathcal{K},\mathcal{H}\right]=\omega\mathcal{K}, \tag{5.139}$$

utilising the commutation relations to find the coupled equations relating the light, matter and bath variables as

$$\omega\boldsymbol{\alpha}=-ic^2\nabla\times\boldsymbol{\beta}+i\frac{\left[\kappa\boldsymbol{\gamma}\right]^{\mathrm{T}}}{\epsilon_0}, \tag{5.140}$$

$$\omega\boldsymbol{\beta}=i\nabla\times\boldsymbol{\alpha}, \tag{5.141}$$

$$\omega\boldsymbol{\gamma}=i\frac{\boldsymbol{\eta}}{\rho}, \tag{5.142}$$

$$\omega\boldsymbol{\eta}=i\kappa\, c^2\nabla\times\boldsymbol{\beta}-i\rho\omega_{\mathrm{L}}^2\boldsymbol{\gamma}+i\frac{\upsilon_\zeta}{\rho}\boldsymbol{\xi}_\zeta, \tag{5.143}$$

$$\omega\boldsymbol{\chi}_\zeta=i\frac{\boldsymbol{\xi}_\zeta}{\rho}-i\frac{\upsilon_\zeta}{\rho}\boldsymbol{\gamma} \tag{5.144}$$

$$\omega\boldsymbol{\xi}_\zeta=-i\rho\zeta^2\boldsymbol{\chi}_\zeta. \tag{5.145}$$

We can solve this equation system by a Fano diagonalisation procedure [193]. which entails utilising Eq. 5.145 to eliminate the $\boldsymbol{\chi}_\zeta$ and thereby write the remaining bath coefficient $\boldsymbol{\xi}_\zeta$ as a function of the $\boldsymbol{\gamma}$

$$\boldsymbol{\xi}_\zeta=\mathcal{P}\frac{\upsilon_\zeta\zeta^2}{\zeta^2-\omega^2}\boldsymbol{\gamma}+\mathbf{y}\left(\omega\right)\delta\left(\zeta-\omega\right), \tag{5.146}$$

where the $\mathcal{P}$ refers to the principal part of the fraction and $\mathbf{y}\left(\omega\right)$ is a frequency- and space-dependent function to be determined. In this way we can reduce the equation system Eq. 5.140-5.145 to one over a single variable $\boldsymbol{\theta}=\boldsymbol{\alpha}+i\frac{\left[\kappa\boldsymbol{\gamma}\right]^{\mathrm{L}}}{\epsilon_0}$. This wave equation is given by

$$\nabla\times\nabla\times\boldsymbol{\theta}-\frac{\omega^2\tilde{\epsilon}\left(\omega\right)}{c^2}\boldsymbol{\theta}=\frac{\omega^2\upsilon_\omega}{\kappa\rho c^2}\left(\tilde{\epsilon}\left(\omega\right)-1\right)\mathbf{y}\left(\omega\right)=i\mu_0\omega\mathbf{j}\left(\omega\right), \tag{5.147}$$

where the now complex dielectric function is

$$\tilde{\epsilon}\left(\omega\right)=\frac{\tilde{\omega}_{\mathrm{L}}^2-\omega^2-\mathcal{G}\left(\omega\right)}{\omega_{\mathrm{T}}^2-\omega^2-\mathcal{G}\left(\omega\right)}, \tag{5.148}$$

and the function $\mathcal{G}\left(\omega\right)$

$$\mathcal{G}\left(\omega\right)=\mathcal{P}\left[\int_0^\infty \mathrm{d}\zeta\frac{\upsilon_\zeta^2\zeta^2}{\rho^2\left(\zeta^2-\omega^2\right)}\right], \tag{5.149}$$

is of the form derived by Wubs and Suttorp [177]. The source current $\mathbf{j}(\omega)$ relates to the function $\mathbf{y}(\omega)$ by

$$\mathbf{j}(\omega)=-\frac{i\omega\upsilon_\omega\epsilon_0}{\kappa\rho}\left[\tilde{\epsilon}(\omega)-1\right]\mathbf{y}(\omega). \tag{5.150}$$

Now we fix the normalisation of our system by imposing the usual bosonic commutation relation on the $\mathcal{K}$ in the continuous case

$$\left[\mathcal{K}_\omega,\mathcal{K}^\dagger_{\omega'}\right]=\delta(\omega-\omega')\mathrm{sgn}(\omega'), \tag{5.151}$$

and by introduction of the wavevectors

$$|\mathbf{\Psi}\rangle=\left(\boldsymbol{\alpha},\beta,\boldsymbol{\gamma},\boldsymbol{\eta},\boldsymbol{\chi}_\zeta,\boldsymbol{\xi}_\zeta\right), \tag{5.152}$$

it is again possible to define an inner product from the polariton commutation relations between polariton modes of positive energy

$$\langle\mathbf{\Psi}|\mathbf{\Psi}'\rangle=i\hbar\int\mathrm{d}\mathbf{r}\left[\frac{\boldsymbol{\alpha}\cdot\nabla\times\bar{\beta}'-\nabla\times\beta\cdot\bar{\boldsymbol{\alpha}}'}{\mu_0}+\boldsymbol{\eta}\cdot\bar{\boldsymbol{\gamma}}'-\boldsymbol{\gamma}\cdot\bar{\boldsymbol{\eta}}'+\int_0^\infty d\zeta\,\left(\boldsymbol{\xi}_\zeta\cdot\bar{\boldsymbol{\chi}}'_\zeta-\boldsymbol{\chi}_\zeta\cdot\bar{\boldsymbol{\eta}}'_\zeta\right)\right]. \tag{5.153}$$

By defining the operator $\mathcal{B}$ as the generalisation of the operator in Eq. 5.56, we may restate Eq. 5.140-5.145 in an operatorial form as

$$\mathcal{B}\,|\mathbf{\Psi}\rangle=\omega\,|\mathbf{\Psi}\rangle, \tag{5.154}$$

and thereby we may calculate the Lagrange identity for the operator $\mathcal{B}$ as

$$\langle\mathbf{\Psi}|\mathcal{B}\mathbf{\Psi}'\rangle-\langle\mathcal{B}\mathbf{\Psi}|\mathbf{\Psi}'\rangle=\int\mathrm{d}\mathbf{r}\left[\boldsymbol{\alpha}\cdot\nabla\times\nabla\times\bar{\boldsymbol{\alpha}}'-\bar{\boldsymbol{\alpha}}'\cdot\nabla\times\nabla\times\boldsymbol{\alpha}\right], \tag{5.155}$$

which gives a boundary condition for the system. This is of exactly the same form as the lossless case as a result of the purely algebraic relations linking the $\boldsymbol{\xi}_\zeta$ and $\boldsymbol{\chi}_\zeta$. The operator $\mathcal{B}$ is thus self-adjoint under the same boundary conditions as $\mathcal{B}_0$. On satisfaction of this boundary condition we are therefore able to find a complete set of bosonic polaritonic operators which are indexed by real frequencies ω [194] and can write the total Hamiltonian in a diagonal form as

$$\mathcal{H}=\hbar\int_{\omega>0}\mathrm{d}\omega\,\mathcal{K}^\dagger_\omega\mathcal{K}_\omega, \tag{5.156}$$

where the integral extends over the positive energy spectrum of Eq. 5.140-5.145.

5.5 Conclusions

In this chapter we introduced a real space Hopfield diagonalisation procedure for arbitrarily inhomogeneous non-magnetic dielectric environments. In Section 5.2 we present the theory in the absence of losses proving that the system eigenmodes can be expanded over an orthonormal and complete basis under application of an appropriate boundary condition. In Section 5.3 we apply this theory to the example of the planar interface between a polar dielectric and a vacuum which supports delocalised SPhP modes. In Section 5.4 we extend the model to encompass dissipative systems showing that in this case the characteristic equations for the Hopfield coefficients require a source term.

We have therefore presented an invertible Hopfield transformation procedure which allows us to express the fields as linear sums of the polariton modes. This allows us to calculate physical observables and more interestingly allows us to express nonlinear interactions in terms of those between polariton modes. For the example presented in Section 5.3 these nonlinear process correspond to anharmonic phonon scattering. We can express the Hamiltonian of the Nth order anharmonicity as

$$\mathcal{H}_{\mathrm{NL}}=\int \mathrm{d}\mathbf{r} \sum_{\mathrm{j}_1\cdots\mathrm{j}_\mathrm{N}=1}^{3} \mathbf{\Phi}^{\mathrm{j}_1\cdots\mathrm{j}_\mathrm{N}} \prod_{\mathrm{l}=1}^{\mathrm{N}} \mathbf{X}_{\mathrm{j}_\mathrm{l}}, \tag{5.157}$$

where spatial coordinates are indicated by the j_l. Our formalism allows us to express the field $\mathbf{X}$ as a sum of the polaritons given by

$$\mathbf{X}=\sum_{\sigma}\int \mathrm{d}\mathbf{k}^{\sigma} \frac{\hbar\kappa\omega_{\mathbf{k}^\sigma}}{\rho\left(\omega_{\mathrm{TO}}^2-\omega_{\mathbf{k}^\sigma}^2\right)} \bar{\boldsymbol{\theta}}_{\mathbf{k}^\sigma}^{\sigma} \mathcal{K}_{\mathbf{k}^\sigma}^{\sigma} \tag{5.158}$$

and therefore we can calculate the nonlinearity in the Hamiltonian by calculation of the appropriate spatial integrals as

$$\mathcal{H}_{\mathrm{NL}}=\sum_{\sigma_1\cdots\sigma_\mathrm{N}} \prod_{\mathrm{l}=1}^{\mathrm{N}} \left[\int \mathrm{d}\mathbf{k}^{\sigma_\mathrm{l}}\right] \Xi_{\mathbf{k}^{\sigma_1}\cdots\mathbf{k}^{\sigma_\mathrm{N}}}^{\sigma_1\cdots\sigma_\mathrm{N}} \prod_{\mathrm{l}=1}^{\mathrm{N}} \mathcal{K}_{\mathbf{k}^{\sigma_\mathrm{l}}}^{\sigma_\mathrm{l}}, \tag{5.159}$$

where the Ξ are found by integrating over the given spatial variable. In this way it would be possible to quantify the strength of the optical non-linearity in the surface

phonon polariton systems considered in Chapter 3. In this system the non-linearity between the coupled modes would arise from phonon-phonon interactions which will result in polariton-polariton interactions.

As discussed in Chapter 3 the deep sub-diffraction nature of phonon polariton modes can allow for a strong enhancement in non-linear polariton interactions compared to those in the planar microcavity systems discussed in Chapter 4 as the rate of an nth order non-linear scattering process is proportional to the nth power of the driving field. The formation of a polariton condensate could then be driven by the strong sub-diffraction confinement of a driving field which mediates strong non-linear phonon-phonon scattering. Vanderbilt *et al.* calculate cubic and quartic zone-centre anharmonic phonon scattering coefficients for the diamond polytypes of silicon, germanium and carbon showing a universality in the coefficients on rescaling by the bond lengths and phonon frequencies [195]. Interestingly the nonlinear interaction predicted from the results of Vanderbilt appears to be attractive. This is easily understood as a result of lattice softening due to an increase in the average atomic spacing in crystals when the phonon density is large and contrasts with the repulsive exciton-exciton nonlinearity in microcavity polariton systems. This could allow for observation of novel nonlinear effects in phonon-polariton condensate systems.

The results of Vanderbilt could be directly applicable to the zinc-blende structure of 3C-SiC and it would be a simple extension to the linear theory presented above to calculate non-linear scattering rates for processes such as second harmonic generation at a planar SiC interface [103]. A fit to experimental data would then allow for calculation of the SiC cubic anharmonic scattering coefficients. If SiC does follow the same pattern then four body scattering processes could be analysed directly by utilising Vanderbilt's results and their strength predicted. If these interactions are of comparable strength to those in exciton polariton systems [6] then phonon polaritons could present an exciting system to explore polariton Bose-Einstein condensation. These questions will be the subject of future publications.

Bibliography

1. Abbe, E. Beiträge zur Theorie des Mikroskops und der mikroskopischen Wahrnehmung. *Archiv für mikroskopische Anatomie* **9.** doi:10.1007/BF02956173 (1873).
2. Caldwell, J. D. *et al.* Low-Loss, Extreme Subdiffraction Photon Confinement via Silicon Carbide Localized Surface Phonon Polariton Resonators. *Nano Letters* **13.** doi:10.1021/nl401590g (2013).
3. Chen, Y. *et al.* Spectral Tuning of Localized Surface Phonon Polariton Resonators for Low-Loss Mid-IR Applications. *ACS Photonics* **1.** doi:10.1021/ph500143u (2014).
4. Weisbuch, C., Nishioka, M., Ishikawa, A. & Arakawa, Y. Observation of the coupled exciton-photon mode splitting in a semiconductor quantum microcavity. *Physical Review Letters* **69.** doi:10.1103/PhysRevLett.69.3314 (1992).
5. Daskalakis, K. S., Maier, S. A., Murray, R. & Kéna-Cohen, S. Nonlinear interactions in an organic polariton condensate. *Nature Materials* **13.** doi:10.1038/nmat3874 (2014).
6. Amo, A. *et al.* Superfluidity of polaritons in semiconductor microcavities. *Nature Physics* **5.** doi:10.1038/nphys1364 (2009).
7. Fan, X., Zheng, W. & Singh, D. J. Light scattering and surface plasmons on small spherical particles. *Light: Science & Applications* **3.** doi:10.1038/lsa.2014.60 (2014).
8. Gorodetsky, M. L., Savchenkov, A. A. & Ilchenko, V. S. Ultimate Q of optical microsphere resonators. *Optics Letters* **21.** doi:10.1364/OL.21.000453 (1996).
9. Lu, Y. F., Zhang, L., Song, W. D., Zheng, Y. W. & Luk'yanchuk, B. S. Laser writing of a subwavelength structure on silicon (100) surfaces with particle-enhanced optical irradiation. *Journal of Experimental and Theoretical Physics Letters* **72.** doi:10.1134/1.1339899 (2000).
10. Kasim, J. *et al.* Near-field Raman imaging using optically trapped dielectric microsphere. *Optics Express* **16.** doi:10.1364/OE.16.007976 (2008).
11. Schmidt, M. K. *et al.* Dielectric antennas - a suitable platform for controlling magnetic dipolar emission. *Optics Express* **20.** doi:10.1364/OE.20.013636 (2012).
12. Albella, P. *et al.* Low-Loss Electric and Magnetic Field-Enhanced Spectroscopy with Subwavelength Silicon Dimers. *The Journal of Physical Chemistry C* **117.** doi:10.1021/jp4027018 (2013).
13. Ritchie, R. H. Plasma Losses by Fast Electrons in Thin Films. *Physical Review* **106.** doi:10.1103/PhysRev.106.874 (1957).

14. Powell, C. J. & Swan, J. B. Origin of the Characteristic Electron Energy Losses in Aluminum. *Physical Review* **115.** doi:10.1103/PhysRev.115.869 (1959).

15. Powell, C. J. & Swan, J. B. Origin of the Characteristic Electron Energy Losses in Magnesium. *Physical Review* **116.** doi:10.1103/PhysRev.116.81 (1959).

16. Fröhlich, H. *Theory of Dielectrics: Dielectric Constant and Dielectric Loss* (Clarendon Press, 1949).

17. Gramotnev, D. K. & Bozhevolnyi, S. I. Plasmonics beyond the diffraction limit. *Nature Photonics* **4.** doi:10.1038/nphoton.2009.282 (2010).

18. Takahara, J., Yamagishi, S., Taki, H., Morimoto, A. & Kobayashi, T. Guiding of a one-dimensional optical beam with nanometer diameter. *Optics Letters* **22.** doi:10.1364/OL.22.000475 (1997).

19. Nerkararyan, K. Superfocusing of a surface polariton in a wedge-like structure. *Physics Letters A* **237.** doi:10.1016/S0375-9601(97)00722-6 (1997).

20. Ebbesen, T. W., Lezec, H. J., Ghaemi, H. F., Thio, T. & Wolff, P. A. Extraordinary optical transmission through sub-wavelength hole arrays. *Nature* **391,** 667–669 (1998).

21. Ciracı, C. *et al.* Probing the Ultimate Limits of Plasmonic Enhancement. *Science* **337.** doi:10.1126/science.1224823 (2012).

22. Khurgin, J. B. How to deal with the loss in plasmonics and metamaterials. *Nature Nanotechnology* **10.** doi:10.1038/nnano.2014.310 (2015).

23. Nordlander, P., Oubre, C., Prodan, E., Li, K. & Stockman, M. I. Plasmon Hybridization in Nanoparticle Dimers. *Nano Letters* **4.** doi:10.1021/nl049681c (2004).

24. Oulton, R. F., Sorger, V. J., Genov, D. A., Pile, D. F. P. & Zhang, X. A hybrid plasmonic waveguide for subwavelength confinement and long-range propagation. *Nature Photonics* **2.** doi:10.1038/nphoton.2008.131 (2008).

25. Khurgin, J. B. & Sun, G. Comparative analysis of spasers, vertical-cavity surface-emitting lasers and surface-plasmon-emitting diodes. *Nature Photonics* **8.** doi:10.1038/nphoton.2014.94 (2014).

26. Stanley, R. Plasmonics in the mid-infrared. *Nature Photonics* **6.** doi:10.1038/nphoton.2012.161 (2012).

27. Oulton, R. F. Plasmonics: Loss and gain. *Nature Photonics* **6.** doi:10.1038/nphoton.2012.72 (2012).

28. Grigorenko, A. N., Polini, M. & Novoselov, K. S. Graphene plasmonics. *Nature Photonics* **6.** doi:10.1038/nphoton.2012.262 (2012).

29. Blaber, M. G., Arnold, M. D. & Ford, M. J. A review of the optical properties of alloys and intermetallics for plasmonics. *Journal of Physics: Condensed Matter* **22.** doi:10.1088/0953-8984/22/14/143201 (2010).

30. Kim, H., Osofsky, M., Prokes, S. M., Glembocki, O. J. & Piqué, A. Optimization of Al-doped ZnO films for low loss plasmonic materials at telecommunication wavelengths. *Applied Physics Letters* **102.** doi:10.1063/1.4802901 (2013).

31. Khurgin, J. B. & Sun, G. In search of the elusive lossless metal. *Applied Physics Letters* **96.** doi:10.1063/1.3425890 (2010).

32. Ndukaife, J. C., Shalaev, V. M. & Boltasseva, A. Plasmonics - turning loss into gain. *Science* **351.** doi:10.1126/science.aad9864 (2016).

33. Adachi, S. *Optical Properties of Crystalline and Amorphous Semiconductors: Materials and Fundamental Principles* 33–61 (Springer US, 1999).

34. Tiwald, T. E. *et al.* Carrier concentration and lattice absorption in bulk and epitaxial silicon carbide determined using infrared ellipsometry. *Physical Review B* **60.** doi:10.1103/PhysRevB.60.11464 (1999).

35. Mutschke, H., Andersen, A. C., Clément, D., Henning, T. & Peiter, G. Infrared properties of SiC particles. *Astronomy and Astrophysics* **345.** doi:arXiv:astro-ph/9903031 (1999).

36. Hillenbrand, R., Taubner, T. & Keilmann, F. Phonon-enhanced light-matter interaction at the nanometre scale. *Nature* **418.** doi:10.1038/nature00899 (2002).

37. Pitman, K. M., Hofmeister, A. M., Corman, A. B. & Speck, A. K. Optical properties of silicon carbide for astrophysical applications. *Astronomy and Astrophysics* **483.** doi:10.1051/0004-6361:20078468 (2008).

38. Geick, R., Perry, C. H. & Rupprecht, G. Normal Modes in Hexagonal Boron Nitride. *Physical Review* **146.** doi:10.1103/PhysRev.146.543 (1966).

39. Cai, Y., Zhang, L., Zeng, Q., Cheng, L. & Xu, Y. Infrared reflectance spectrum of BN calculated from first principles. *Solid State Communications* **141.** doi:10.1016/j.ssc.2006.10.040 (2007).

40. Dai, S. *et al.* Tunable Phonon Polaritons in Atomically Thin van der Waals Crystals of Boron Nitride. *Science* **343.** doi:10.1126/science.1246833 (2014).

41. Caldwell, J. D. *et al.* Sub-diffractional volume-confined polaritons in the natural hyperbolic material hexagonal boron nitride. *Nature Communications* **5.** doi:10.1038/ncomms6221 (2014).

42. Moore, W. J. & Holm, R. T. Infrared dielectric constant of gallium arsenide. *Journal of Applied Physics* **80.** doi:10.1063/1.363818 (1996).

43. Haraguchi, M., Fukui, M. & Muto, S. Experimental observation of attenuated-total-reflection spectra of GaAs/AlAs superlattice. *Physical Review B* **41.** doi:10.1103/PhysRevB.41.1254 (1990).

44. Jamshidi, H. & Parker, T. J. The far infrared optical properties of InP at 6 and 300 K. *International Journal of Infrared and Millimeter Waves* **4.** doi:10.1007/BF01009327 (1983).

45. Hofmann, M., Zywietz, A., Karch, K. & Bechstedt, F. Lattice dynamics of SiC polytypes within the bond-charge model. *Physical Review B* **50.** doi:10.1103/PhysRevB.50.13401 (1994).

46. Lyddane, R. H., Sachs, R. G. & Teller, E. On the Polar Vibrations of Alkali Halides. *Physical Review* **59.** doi:10.1103/PhysRev.59.673 (1941).

47. Dolling, G. *Lattice vibrations in crystals with the diamond structure* in *Inelastic Scattering of Neutrons in Solids and Liquids* **2** (IAEA, 1963), 37–48.

48. Fan, J. & Chu, P. K. *Silicon Carbide Nanostructures: Fabrication, Structure, and Properties* 7–114 (Springer International, 2014).

49. Deinzer, G., Schmitt, M., Mayer, A. P. & Strauch, D. Intrinsic lifetimes and anharmonic frequency shifts of long-wavelength optical phonons in polar crystals. *Physical Review B* **69.** doi:10.1103/PhysRevB.69.014304 (2004).

50. Lindsay, L. & Broido, D. A. Three-phonon phase space and lattice thermal conductivity in semiconductors. *Journal of Physics: Condensed Matter* **20.** doi:10.1088/0953-8984/20/16/165209 (2008).

51. Lindsay, L., Broido, D. A. & Reinecke, T. L. *Ab initio* thermal transport in compound semiconductors. *Physical Review B* **87.** doi:10.1103/PhysRevB.87.165201 (2013).

52. Caldwell, J. D. *et al.* Low-loss, infrared and terahertz nanophotonics using surface phonon polaritons. *Nanophotonics* **4.** doi:10.1515/nanoph-2014-0003 (2015).

53. Bosman, M. *et al.* Surface Plasmon Damping Quantified with an Electron Nanoprobe. *Scientific Reports* **3.** doi:10.1038/srep01312 (2013).

54. Wimbauer, T., Meyer, B. K., Hofstaetter, A., Scharmann, A. & Overhof, H. Negatively charged Si vacancy in 4H SiC: A comparison between theory and experiment. *Physical Review B* **56.** doi:10.1103/PhysRevB.56.7384 (1997).

55. Torpo, L., Pöykkö, S. & Nieminen, R. M. Antisites in silicon carbide. *Physical Review B* **57.** doi:10.1103/PhysRevB.57.6243 (1998).

56. Lindsay, L., Broido, D. A. & Reinecke, T. L. Phonon-isotope scattering and thermal conductivity in materials with a large isotope effect: A first-principles study. *Physical Review B* **88.** doi:10.1103/PhysRevB.88.144306 (2013).

57. Caldwell, J. D., Stahlbush, R. E. & Mahadik, N. A. Mitigating defects within Silicon Carbide Epitaxy. *Journal of the Electrochemical Society* **159.** doi:10.1149/2.069203jes (2012).

58. Bohren, C. F. & Huffman, D. R. *Absorption and Scattering of Light by Small Particles* 57–129 (Wiley, 1998).

59. Wang, F. & Shen, Y. R. General Properties of Local Plasmons in Metal Nanostructures. *Physical Review Letters* **97.** doi:10.1103/PhysRevLett.97.206806 (2006).

60. Ocelic, N. & Hillenbrand, R. Subwavelength-scale tailoring of surface phonon polaritons by focussed ion-beam implantation. *Nature Materials* **3.** doi:10.1038/nmat1194 (2004).

61. Taubner, T., Keilmann, F. & Hillenbrand, R. Nanomechanical Resonance Tuning and Phase Effects in Optical Near-Field Interaction. *Nano Letters* **4.** doi:10.1021/nl0491677 (2004).

62. Huber, A., Ocelic, N., Taubner, T. & Hillenbrand, R. Nanoscale Resolved Infrared Probing of Crystal Structure and of Plasmon-Phonon Coupling. *Nano Letters* **6.** doi:10.1021/nl060092b (2006).

63. Korobkin, D., Urzhumov, Y. & Shvets, G. Enhanced near-field resolution in midinfrared using metamaterials. *Journal of the Optical Society of America B* **23.** doi:10.1364/JOSAB.23.000468 (2006).

64. Taubner, T., Korobkin, D., Urzhumov, Y., Shvets, G. & Hillenbrand, R. Near-Field Microscopy Through a SiC Superlens. *Science* **313.** doi:10.1126/science.1131025 (2006).

65. Greffet, J.-J. *et al.* Coherent Emission of Light by Thermal Sources. *Nature* **416.** doi:10.1038/416061a (2002).

66. Streyer, W. *et al.* Engineering absorption and blackbody radiation in the far-infrared with surface phonon polaritons on gallium phosphide. *Applied Physics Letters* **104.** doi:10.1063/1.4870255 (2014).

67. Schuller, J. A., Taubner, T. & Brongersma, M. L. Optical antenna thermal emitters. *Nature Photonics* **3.** doi:10.1038/nphoton.2009.188 (2009).

68. Neuner III, B. *et al.* Efficient infrared thermal emitters based on low-albedo polaritonic meta-surfaces. *Applied Physics Letters* **102.** doi:10.1063/1.4808086 (2013).

69. Anderson, M. S. Enhanced Infrared Absorption with Dielectric Nanoparticles. *Applied Physics Letters* **83.** doi:10.1063/1.1615317 (2003).

70. Shen, S., Narayanaswamy, A. & Chen, G. Surface Phonon Polaritons Mediated Energy Transfer between Nanoscale Gaps. *Nano Letters* **9.** doi:10.1021/nl901208v (2009).

71. Li, D., Lawandy, N. M. & Zia, R. Surface phonon-polariton enhanced optical forces in silicon carbide nanostructures. *Optics Express* **21.** doi:10.1364/OE.21.020900 (2013).

72. Feng, K. *et al.* Localized surface phonon polariton resonances in polar gallium nitride. *Applied Physics Letters* **107.** doi:10.1063/1.4929502 (2015).

73. Wang, T., Li, P., Hauer, B., Chigrin, D. N. & Taubner, T. Optical Properties of Single Infrared Resonant Circular Microcavities for Surface Phonon Polaritons. *Nano Letters* **13.** doi:10.1021/nl4020342 (2013).

74. Berini, P. Figures of merit for surface plasmon waveguides. *Optics Express* **14.** doi:10.1364/OE.14.013030 (2006).

75. Neuner III, B. *et al.* Critically coupled surface phonon-polariton excitation in silicon carbide. *Optics Letters* **34.** doi:10.1364/OL.34.002667 (2009).

76. Huber, A., Ocelic, N., Kazantsev, D. & Hillenbrand, R. Near-field imaging of mid-infrared surface phonon polariton propagation. *Applied Physics Letters* **87.** doi:10.1063/1.2032595 (2005).

77. Huber, A., Deutsch, B., Novotny, L. & Hillenbrand, R. Focusing of Surface Phonon Polaritons. *Applied Physics Letters* **92.** doi:10.1063/1.2930681 (2008).

78. Holmstrom, S. A. *et al.* Guided-mode phonon-polaritons in suspended waveguides. *Physical Review B* **86.** doi:10.1103/PhysRevB.86.165120 (2012).

79. Ditlbacher, H. *et al.* Silver Nanowires as Surface Plasmon Resonators. *Physical Review Letters* **95.** doi:10.1103/PhysRevLett.95.257403 (2005).

80. Martin, P. A. *Multiple Scattering: Interaction of Time-Harmonic Waves with N Obstacles* 17–18 (Cambridge University Press, 2006).

81. Ching, S. C., Lai, H. M. & K., Y. Dielectric microspheres as optical cavities: thermal spectrum and density of states. *Journal of the Optical Society of America B* **4.** doi:10.1364/JOSAB.4.001995 (1987).

82. Ching, E. S. C. *et al.* Quasinormal-mode expansion for waves in open systems. *Reviews of Modern Physics* **70.** doi:10.1103/RevModPhys.70.1545 (1998).

83. Kristensen, P. T., Van Vlack, C. & Hughes, S. Generalized Effective Mode Volume for Leaky Optical Cavities. *Optics Letters* **37.** doi:10.1364/OL.37.001649 (2012).

84. Sauvan, C., Hugonin, J. P., Maksymov, I. S. & Lalanne, P. Theory of the Spontaneous Optical Emission of Nanosize Photonic and Plasmon Resonators. *Physical Review Letters* **110.** doi:10.1103/PhysRevLett.110.237401 (2013).

85. Lai, H. M., Leung, P. T., Young, K., Barber, P. W. & Hill, S. C. Time-independent perturbation for leaking electromagnetic modes in open systems with application to resonances in microdroplets. *Physical Review A* **41.** doi:10.1103/PhysRevA.41.5187 (1990).

86. Kristensen, P. T., Ge, R.-C. & Hughes, S. Normalization of quasinormal modes in leaky optical cavities and plasmonic resonators. *Physical Review A* **92.** doi:10.1103/PhysRevA.92.053810 (2015).

87. Muljarov, E. A. & Langbein, W. Exact mode volume and Purcell factor of open optical systems. *arXiv:1409.6877* **cond-mat.mes-hall** (2014).

88. Chew, W. C. & Weedon, W. H. A 3D perfectly matched medium from modified Maxwell's equations with stretched coordinates. *Microwave and Optical Technology Letters* **7.** doi:10.1002/mop.4650071304 (1994).

89. Leung, P. T., Liu, S. Y. & Young, K. Completeness and time-independent perturbation of the quasinormal modes of an absorptive and leaky cavity. *Physical Review A* **49.** doi:10.1103/PhysRevA.49.3982 (1994).

90. Lee, K. M., Leung, P. T. & Pang, K. M. Dyadic formulation of morphology-dependent resonances. I. Completeness relation. *Journal of the Optical Society of America B* **16.** doi:10.1364/JOSAB.16.001409 (1999).

91. Bai, Q., Perrin, M., Sauvan, C., Hugonin, J. P. & Lalanne, P. Efficient and intuitive method for the analysis of light scattering by a resonant nanostructure. *Optics Express* **21.** doi:10.1364/OE.21.027371 (2013).

92. Koenderink, A. F. On the use of Purcell factors for plasmon antennas. *Optics Letters* **24.** doi:10.1364/OL.35.004208 (35).

93. Ge, R.-C., Kristensen, P. T., Young, J. F. & Hughes, S. Quasinormal mode approach to modelling light emission and propagation in nanoplasmonics. *New Journal of Physics* **16.** doi:10.1088/1367-2630/16/11/113048 (2014).

94. Liu, M., Lee, T.-W., Gray, S. K., Guyot-Sionnest, P. & Pelton, M. Excitation of Dark Plasmons in Metal Nanoparticles by a Localized Emitter. *Phys. Rev. Lett.* **102.** doi:10.1103/PhysRevLett.102.107401 (2009).

95. Nordlander, P. & Prodan, E. Plasmon Hybridization in Nanoparticles near Metallic Surfaces. *Nano Letters* **4.** doi:10.1021/nl0486160 (2004).

96. Yariv, A., Xu, Y., Lee, R. K. & Scherer, A. Coupled-Resonator Optical Waveguide: A Proposal and Analysis. *Optics Letters* **24.** doi:10.1364/OL.24.000711 (1999).

97. Hopfield, J. J. Theory of the Contribution of Excitons to the Complex Dielectric Constant of Crystals. *Physical Review* **112.** doi:10.1103/PhysRev.112.1555 (1958).

98. Christ, A., Tikhodeev, S. G., Gippius, N. A., Kuhl, J. & Giessen, H. Waveguide-Plasmon Polaritons: Strong Coupling of Photonic and Electronic Resonances in a Metallic Photonic Crystal Slab. *Physical Review Letters* **91.** doi:10.1103/PhysRevLett.91.183901 (2003).

99. De Liberato, S. Light-matter decoupling in the deep strong coupling regime: The breakdown of the Purcell effect. *Physical Review Letters* **112.** doi:10.1103/PhysRevLett.112.016401 (2014).

100. Cade, N. I., Ritman-Meer, T. & Richards, D. Strong coupling of localized plasmons and molecular excitons in nanostructured silver films. *Physical Review B* **79.** doi:10.1103/PhysRevB.79.241404 (2009).

101. Ferro, G., Chassagne, T., Leycuras, A., Cauwet, F. & Monteil, Y. Strain tailoring in 3C-SiC heteroepitaxial layers grown on Si(100). *Chemical Vapour Deposition* **12.** doi:10.1002/cvde.200506461 (2006).

102. Anappara, A. A. *et al.* Signatures of the ultrastrong light-matter coupling regime. *Physical Review B* **79.** doi:10.1103/PhysRevB.79.201303 (2009).

103. Paarmann, A. *et al.* Second harmonic generation spectroscopy in the Reststrahl band of SiC using an infrared free-electron laser. *Applied Physics Letters* **107.** doi:10.1063/1.4929358 (2015).

104. Razdolski, I. *et al.* Resonant enhancement of second harmonic generation in the mid-infrared using localized surface phonon polaritons in sub-diffractional nanostructures. *arXiv:1607.05158* **physics.optics** (2016).

105. Baumberg, J. J. *et al.* Parametric oscillation in a vertical microcavity: A polariton condensate or micro-optical parametric oscillators. *Physical Review B* **62.** doi:10.1103/PhysRevB.62.R16247 (2000).

106. Jung, J. & S, T. Green's function surface integral equation method for theoretical analysis of scatterers close to a metal interface. *Physical Review B* **77.** doi:10.1103/PhysRevB.77.245310 (2008).

107. Gubbin, C. R., Maier, S. A. & Kena-Cohen, S. Low-voltage polariton electroluminescence from an ultrastrongly coupled organic light-emitting diode. *Applied Physics Letters* **104.** doi:10.1063/1.4871271 (2014).

108. Hobson, P. A. *et al.* Strong exciton-photon coupling in a low-Q all-metal mirror microcavity. *Applied Physics Letters* **81.** doi:10.1063/1.1517714 (2002).

109. Tischler, J. R., Bradley, M. S., Bulović, V., Song, J. H. & Nurmikko, A. Strong Coupling in a Microcavity LED. *Physical Review Letters* **95.** doi:10.1103/PhysRevLett.95.036401 (2005).

110. Lodden, G. H. & Holmes, R. J. Polarization splitting in polariton electroluminescence from an organic semiconductor microcavity with metallic reflectors. *Applied Physics Letters* **98.** doi:10.1063/1.3599058 (2011).

111. Hayashi, S., Ishigaki, Y. & Fujii, M. Plasmonic effects on strong exciton-photon coupling in metal-insulator-metal microcavities. *Physical Review B* **86.** doi:10.1103/PhysRevB.86.045408 (2012).

112. Kéna-Cohen, S., Maier, S. A. & Bradley, D. D. C. Ultrastrongly Coupled Exciton-Polaritons in Metal-Clad Organic Semiconductor Microcavities. *Advanced Optical Materials* **1.** doi:10.1002/adom.201300256 (2013).

113. Houdré, R. *et al.* Measurement of Cavity-Polariton Dispersion Curve from Angle-Resolved Photoluminescence Experiments. *Phys. Rev. Lett.* **73.** doi:10.1103/PhysRevLett.73.2043 (1994).

114. Savvidis, P. G. *et al.* Angle-Resonant Stimulated Polariton Amplifier. *Physical Review Letters* **84.** doi:10.1103/PhysRevLett.84.1547 (2000).

115. Deng, H., Weihs, G., Snoke, D., Bloch, J. & Yamamoto, Y. Polariton lasing vs. photon lasing in a semiconductor microcavity. *Proceedings of the National Academy of Sciences of the United States of America* **100.** doi:10.1073/pnas.2634328100 (2003).

116. Lagoudakis, K. G. *et al.* Quantized vortices in an exciton-polariton condensate. *Nature Physics* **4.** doi:10.1038/nphys1051 (2008).

117. Suzuki, T. & Shimano, R. Exciton Mott Transition in Si Revealed by Terahertz Spectroscopy. *Physical Review Letters* **109.** doi:10.1103/PhysRevLett.109.046402 (2012).

118. Colombelli, R. & Manceau, J.-M. Perspectives for Intersubband Polariton Lasers. *Physical Review X* **5.** doi:10.1103/PhysRevX.5.011031 (2015).

119. Dini, D., Köhler, R., Tredicucci, A., Biasiol, G. & Sorba, L. Microcavity Polariton Splitting of Intersubband Transitions. *Physical Review Letters* **90.** doi:10.1103/PhysRevLett.90.116401 (2003).

120. Colombelli, R., Ciuti, C., Chassagneux, Y. & Sirtori, C. Quantum cascade intersubband polariton light emitters. *Semiconductor Science and Technology* **20.** doi:10.1088/0268-1242/20/10/001 (2005).

121. Lidzey, D. G. *et al.* Strong exciton-photon coupling in an organic semiconductor microcavity. *Nature* **395.** doi:10.1038/25692 (1998).

122. Lidzey, D. G. *et al.* Room Temperature Polariton Emission from Strongly Coupled Organic Semiconductor Microcavities. *Physical Review Letters* **82.** doi:10.1103/PhysRevLett.82.3316 (1999).

123. Kena-Cohen, S. & Forrest, S. R. Room-temperature polariton lasing in an organic single-crystal microcavity. *Nature Photonics* **4.** doi:10.1038/nphoton.2010.86 (2010).

124. Plumhof, J. D., Stöferle, T., Mai, L., Scherf, U. & Mahrt, R. F. Room-temperature Bose-Einstein condensation of cavity exciton-polaritons in a polymer. *Nature Materials* **13.** doi:10.1038/nmat3825 (2014).

125. Ciuti, C., Bastard, G. & Carusotto, I. Quantum vacuum properties of the intersubband cavity polariton field. *Physical Review B* **72.** doi:10.1103/PhysRevB.72.115303 (2005).

126. Quattropani, A., Andreani, L. C. & Bassani, F. Quantum theory of polaritons with spatial dispersion: Exact solutions. *Il Nuovo Cimento D* **7.** doi:10.1007/BF02452395 (1986).

127. De Liberato, S., Ciuti, C. & Carusotto, I. Quantum Vacuum Radiation Spectra from a Semiconductor Microcavity with a Time-Modulated Vacuum Rabi Frequency. *Physical Review Letters* **98.** doi:10.1103/PhysRevLett.98.103602 (2007).

128. Gunter, G. *et al.* Sub-cycle switch-on of ultrastrong light-matter interaction. *Nature* **458.** doi:10.1038/nature07838 (2009).

129. Jouy, P. *et al.* Transition from strong to ultrastrong coupling regime in mid-infrared metal-dielectric-metal cavities. *Applied Physics Letters* **98.** doi:10.1063/1.3598432 (2011).

130. Todorov, Y. *et al.* Strong Light-Matter Coupling in Subwavelength Metal-Dielectric Microcavities at Terahertz Frequencies. *Physical Review Letters* **102.** doi:10.1103/PhysRevLett.102.186402 (2009).

131. Wong, K.-T. *et al.* Ter(9,9-diarylfluorene)s: Highly Efficient Blue Emitter with Promising Electrochemical and Thermal Stability. *Journal of the American Chemical Society* **124.** doi:10.1021/ja0269587 (2002).

132. Schwartz, T., Hutchison, J. A., Genet, C. & Ebbesen, T. W. Reversible Switching of Ultrastrong Light-Molecule Coupling. *Physical Review Letters* **106.** doi:10.1103/PhysRevLett.106.196405 (2011).

133. Agranovich, V. M., Litinskaia, M. & Lidzey, D. G. Cavity polaritons in microcavities containing disordered organic semiconductors. *Physical Review B* **67.** doi:10.1103/PhysRevB.67.085311 (2003).

134. Litinskaya, M., Reineker, P. & Agranovich, V. Fast polariton relaxation in strongly coupled organic microcavities. *Journal of Luminescence* **110.** doi:10.1016/j.jlumin.2004.08.033 (2004).

135. Coles, D. M. *et al.* Vibrationally Assisted Polariton-Relaxation Processes in Strongly Coupled Organic-Semiconductor Microcavities. *Advanced Functional Materials* **21.** doi:10.1002/adfm.201100756 (2011).

136. Lidzey, D. G. *et al.* Experimental study of light emission from strongly coupled organic semiconductor microcavities following nonresonant laser excitation. *Physical Review B* **65.** doi:10.1103/PhysRevB.65.195312 (2002).

137. Lodden, G. H. & Holmes, R. J. Electrical excitation of microcavity polaritons by radiative pumping from a weakly coupled organic semiconductor. *Physical Review B* **82.** doi:10.1103/PhysRevB.82.125317 (2010).

138. Schneider, C. *et al.* An electrically pumped polariton laser. *Nature* **497.** doi:10.1038/nature12036 (2013).

139. Christogiannis, N. *et al.* Characterizing the Electroluminescence Emission from a Strongly Coupled Organic Semiconductor Microcavity LED. *Advanced Optical Materials* **1.** doi:10.1002/adom.201300017 (2013).

140. Wu, C.-C., Lin, Y.-T., Wong, K.-T., Chen, R.-T. & Chien, Y.-Y. Efficient Organic Blue-Light-Emitting Devices with Double Confinement on Terfluorenes with Ambipolar Carrier Transport Properties. *Advanced Materials* **16.** doi:10.1002/adma.200305619 (2004).

141. Haitao, X. & Xiang, Z. Investigation of hole injection enhancement by MoO3 buffer layer in organic light emitting diodes. *Journal of Applied Physics* **114.** doi:10.1063/1.4852835 (2013).

142. Scalari, G. *et al.* Ultrastrong Coupling of the Cyclotron Transition of a 2D Electron Gas to a THz Metamaterial. *Science* **335.** doi:10.1126/science.1216022 (2012).

143. Hutchison, J. A. *et al.* Tuning the Work-Function Via Strong Coupling. *Advanced Materials* **25.** doi:10.1002/adma.201203682 (2013).

144. Mazza, L., Fontanesi, L. & La Rocca, G. C. Organic-based microcavities with vibronic progressions: Photoluminescence. *Physical Review B* **80.** doi:10.1103/PhysRevB.80.235314 (2009).

145. Michetti, P. & La Rocca, G. C. Simulation of J-aggregate microcavity photoluminescence. *Physical Review B* **77.** doi:10.1103/PhysRevB.77.195301 (2008).

146. Geiser, M., Scalari, G., Castellano, F., Beck, M. & Faist, J. Room temperature terahertz polariton emitter. *Applied Physics Letters* **101.** doi:10.1063/1.4757611 (2012).

147. Mazzeo, M. *et al.* Ultrastrong light-matter coupling in electrically doped microcavity organic light emitting diodes. *Applied Physics Letters* **104.** doi:10.1063/1.4882422 (2014).

148. Cirio, M., De Liberato, S., Lambert, N. & Nori, F. Ground State Electroluminescence. *Physical Review Letters* **116.** doi:10.1103/PhysRevLett.116.113601 (2016).

149. Archambault, A., Marquier, F., Greffet, J.-J. & Arnold, C. Quantum theory of spontaneous and stimulated emission of surface plasmons. *Physical Review B* **82.** doi:10.1103/PhysRevB.82.035411 (2010).

150. Todorov, Y. Dipolar Quantum Electrodynamics Theory of the Three-Dimensional Electron Gas. *Physical Review B* **89.** doi:10.1103/PhysRevB.89.075115 (2014).

151. Born, M. & Infeld, L. On the Quantization of the New Field Equations. I. *Proceedings of the Royal Society of London A: Mathematical, Physical and Engineering Sciences* **147.** doi:10.1098/rspa.1934.0234 (1934).

152. Jauch, J. M. & Watson, K. M. Phenomenological Quantum-Electrodynamics. *Physical Review* **74.** doi:10.1103/PhysRev.74.950 (1948).

153. Abram, I. Quantum theory of light propagation: Linear medium. *Physical Review A* **35.** doi:10.1103/PhysRevA.35.4661 (1987).

154. Knöll, L., Vogel, W. & Welsch, D.-G. Action of passive, lossless optical systems in quantum optics. *Physical Review A* **36.** doi:10.1103/PhysRevA.36.3803 (1987).

155. Glauber, R. J. & Lewenstein, M. Quantum optics of dielectric media. *Physical Review A* **43.** doi:10.1103/PhysRevA.43.467 (1991).

156. Bordag, M., Kirsten, K. & Vassilevich, D. V. Path-integral quantization of electrodynamics in dielectric media. *Journal of Physics A: Mathematical and General* **31.** doi:10.1088/0305-4470/31/10/013 (1998).

157. Dalton, B. J., Barnett, S. M. & Knight, P. L. Quasi mode theory of macroscopic canonical quantization in quantum optics and cavity quantum electrodynamics. *Journal of Modern Optics* **46.** doi:10.1080/09500349908231338 (1999).

158. Milonni, P. W. Field quantization and radiative processes in dispersive dielectric media. *Journal of Modern Optics* **42.** doi:10.1080/09500349514551741 (1995).

159. Santos, D. J. & Loudon, R. Electromagnetic-field quantization in inhomogeneous and dispersive one-dimensional systems. *Physical Review A* **52.** doi:10.1103/PhysRevA.52.1538 (1995).

160. Huttner, B., Baumberg, J. J. & Barnett, S. M. Canonical quantization of light in a linear dielectric. *Europhysics Letters* **16.** doi:10.1209/0295-5075/16/2/010 (1991).

161. Hradil, Z. Decomposition of the electromagnetic field in lossless inhomogeneous dispersive dielectrics. *Physical Review A* **53.** doi:10.1103/PhysRevA.53.3687 (1996).

162. Drummond, P. D. & Hillery, M. Quantum theory of dispersive electromagnetic modes. *Physical Review A* **59.** doi:10.1103/PhysRevA.59.691 (1999).

163. Tatian, B. Fitting refractive-index data with the Sellmeier dispersion formula. *Applied Optics* **23.** doi:10.1364/AO.23.004477 (1984).

164. Vogel, W. & Welsch, D.-G. *Quantum Optics* 38–39 (WILEY-VCH Verlag, 2006).

165. Bamba, M. & Ogawa, T. Stability of polarizable materials against superradiant phase transitions. *Physical Review A* **90.** doi:10.1103/PhysRevA.90.063825 (2014).

166. Ruppin, R. Electromagnetic energy density in a dispersive and absorptive material. *Physics Letters A* **299.** doi:10.1016/S0375-9601(01)00838-6 (2002).

167. Dritschel, M. A. & Rovnyak, J. *Lectures on Operator Theory and its Applications* (ed Lancaster, P.) 143–227 (Americal Mathematical Society, 1991).

168. Elson, J. M. & Ritchie, R. H. Photon interactions at a rough metal surface. *Physical Review B* **4.** doi:10.1103/PhysRevB.4.4129 (1971).

169. Ballester, D., Tame, M. S. & Kim, M. S. Quantum theory of surface plasmon scattering. *Physical Review A* **82.** doi:10.1103/PhysRevA.82.012325 (2010).

170. Gruner, T. & Welsch, D.-G. Green-function approach to the radiation-field quantization for homogeneous and inhomogeneous Kramers-Kronig dielectrics. *Physical Review A* **53.** doi:10.1103/PhysRevA.53.1818 (1996).

171. Bohm, D. & Pines, D. A Collective Description of Electron Interactions: III. Coulomb Interactions in a Degenerate Electron Gas. *Physical Review* **92.** doi:10.1103/PhysRev.92.609 (1953).

172. Xu, Z. & Zhu, K. Quantum Theory of Surface Polaritons in Semi-Infinite Dielectric Systems. *Communications in Theoretical Physics* **14.** doi:10.1088/0253-6102/14/2/139 (1990).

173. Hammer, H. Orthogonality relations for triple modes at dielectric boundary surfaces. *Journal of Modern Optics* **50.** doi:10.1080/09500340308235171 (2003).

174. Huttner, B. & Barnett, S. M. Quantization of the electromagnetic field in dielectrics. *Physical Review A* **46.** doi:10.1103/PhysRevA.46.4306 (1992).

175. Ho, S. T. & Kumar, P. Quantum optics in a dielectric: macroscopic electromagnetic-field and medium operators for a linear dispersive lossy medium—a microscopic derivation of the operators and their commutation relations. *Journal of the Optical Society of America B* **10.** doi:10.1364/JOSAB.10.001620 (1993).

176. Wubs, M. & Suttorp, L. G. Transient QED effects in absorbing dielectrics. *Physical Review A* **63.** doi:10.1103/PhysRevA.63.043809 (2001).

177. Suttorp, L. G. & Wubs, M. Field quantization in inhomogeneous absorptive dielectrics. *Physical Review A* **70.** doi:10.1103/PhysRevA.70.013816 (2004).

178. Suttorp, L. G. & van Wonderen, A. J. Fano diagonalization of a polariton model for an inhomogeneous absorptive dielectric. *Europhysics Letters* **67.** doi:10.1209/epl/i2004-10131-8 (2004).

179. Suttorp, L. G. Field quantization in inhomogeneous anisotropic dielectrics with spatio-temporal dispersion. *Journal of Physics A: Mathematical and Theoretical* **40.** doi:10.1088/1751-8113/40/13/025 (2007).

180. Kheirandish, F. & Soltani, M. Extension of the Huttner-Barnett model to a magnetodielectric medium. *Physical Review A* **78.** doi:10.1103/PhysRevA.78.012102 (2008).

181. Gruner, T. & Welsch, D.-G. Correlation of radiation-field ground-state fluctuations in a dispersive and lossy dielectric. *Physical Review A* **51.** doi:10.1103/PhysRevA.51.3246 (1995).

182. Knöll, L. & Leonhardt, U. Quantum Optics in Oscillator Media. *Journal of Modern Optics* **39.** doi:10.1080/713823539 (1992).

183. Matloob, R., Loudon, R., Barnett & Jeffers, J. Electromagnetic field quantization in absorbing dielectrics. *Physical Review A* **52.** doi:10.1103/PhysRevA.52.4823 (1995).

184. Matloob, R. & Loudon, R. Electromagnetic field quantization in absorbing dielectrics. II. *Physical Review A* **53.** doi:10.1103/PhysRevA.53.4567 (1996).

185. Tip, A. Canonical formalism and quantization for a class of classical fields with application to radiative atomic decay in dielectrics. *Physical Review A* **56.** doi:10.1103/PhysRevA.56.5022 (1997).

186. Tip, A. Linear absorptive dielectrics. *Physical Review A* **57.** doi:10.1103/PhysRevA.57.4818 (1998).

187. Matloob, R. Electromagnetic field quantization in an absorbing medium. *Physical Review A* **60.** doi:10.1103/PhysRevA.60.50 (1999).

188. Dung, H. T., Knöll, L. & Welsch, D.-G. Three-dimensional quantization of the electromagnetic field in dispersive and absorbing inhomogeneous dielectrics. *Physical Review A* **57.** doi:10.1103/PhysRevA.57.3931 (1998).

189. Scheel, S., Knöll, L. & Welsch, D.-G. QED commutation relations for inhomogeneous Kramers-Kronig dielectrics. *Physical Review A* **58.** doi:10.1103/PhysRevA.58.700 (1998).

190. Di Stefano, O., Savasta, S. & Girlanda, R. Electromagnetic-field quantization in absorbing confined systems. *Physical Review A* **60.** doi:10.1103/PhysRevA.60.1614 (1999).

191. Horsley, S. & Philbin, T. Canonical quantization of electromagnetism in spatially dispersive media. *New Journal of Physics* **16.** doi:10.1088/1367-2630/16/1/013030 (2014).

192. Judge, A. C., Steel, M. J., Sipe, J. E. & de Sterke, C. M. Canonical quantization of macroscopic electrodynamics in a linear inhomogeneous magnetoelectric medium. *Physical Review A* **87.** doi:10.1103/PhysRevA.87.033824 (2013).

193. Fano, U. Effects of Configuration Interaction on Intensities and Phase Shifts. *Physical Review* **124.** doi:10.1103/PhysRev.124.1866 (1961).

194. Archambault, A., Teperik, T., Marquier, F. & Greffet, J.-J. Surface Plasmon Fourier Optics. *Physical Review B* **79.** doi:10.1103/PhysRevB.79.195414 (2009).

195. Vanderbilt, D., Louie, S. G. & Cohen, M. L. Calculation of anharmonic phonon couplings in C, Si, and Ge. *Physical Review B* **33.** doi:10.1103/PhysRevB.33.8740 (1985).